2015

Experimental and Numerical Study of Endwall Film Cooling

Srikrishna Mahadevan
University of Central Florida

EXPERIMENTAL AND NUMERICAL STUDY OF ENDWALL FILM COOLING

by

SRIKRISHNA MAHADEVAN
B.E., SRM College of Engineering (Anna University), 2008
M.S., Southern Illinois University, 2009

A dissertation submitted in partial fulfillment of the requirements
for the degree of Doctor of Philosophy
in the Department of Mechanical and Aerospace Engineering
in the College of Engineering and Computer Science
at the University of Central Florida
Orlando, Florida

Fall Term
2015

Major Professor: Jayanta S. Kapat

ABSTRACT

This research work investigates the thermal performance of a film-cooled gas turbine endwall under two different mainstream flow conditions. In the first part of the research investigation, the effect of unsteady passing wakes on a film-cooled pitchwise-curved surface (representing an endwall without airfoils) was experimentally studied for heat transfer characteristics on a time-averaged basis. The temperature sensitive paint technique was used to obtain the local temperatures on the test surface. The required heat flux input was provided using foil heaters. Discrete film injection was implemented on the test surface using cylindrical holes with a streamwise inclination angle of 35˚ and no compound angle relative to the mean approach velocity vector. The passing wakes increased the heat transfer coefficients at both the wake passing frequencies that were experimented. Due to the increasing film cooling jet turbulence and strong jet-mainstream interaction at higher blowing ratios, the heat transfer coefficients were amplified. A combination of film injection and unsteady passing wakes resulted in a maximum pitch-averaged and centerline heat transfer augmentation of ≅ 28% and 31.7% relative to the no wake and no film injection case.

The second part of the research study involves an experimental and numerical analysis of secondary flow and coolant film interaction in a high subsonic annular cascade with a maximum isentropic throat Mach number of ≅ 0.68. Endwall (platform) thermal protection is provided using discrete cylindrical holes with a streamwise inclination angle of 30˚ and no compound angle relative to the mean approach velocity vector. The surface flow visualization on the inner endwall provided the location of the saddle point and the

three-dimensional separation lines. Computational predictions showed that the leading-edge horseshoe vortex was confined to approximately 1.5% of the airfoil span for the no film injection case and intensified with low momentum film injection. At the highest blowing ratio, the film cooling jet weakened the horseshoe vortex at the leading-edge plane. The passage vortex was intensified with coolant injection at all blowing ratios. It was seen that increasing average blowing ratio improved the film effectiveness on the endwall. The discharge coefficients calculated for each film cooling hole indicated significant non-uniformity in the coolant discharge at lower blowing ratios and the strong dependence of discharge coefficients on the mainstream static pressure and the location of three-dimensional separation lines. Near the airfoil suction side, a region of coalesced film cooling jets providing close to uniform film coverage was observed, indicative of the mainstream acceleration and the influence of three-dimensional separation lines.

"This Dissertation is dedicated to my Parents, Siblings and other Family members for their invaluable love, guidance and support"

ACKNOWLEDGMENTS

First and foremost, I owe my gratitude to my major advisor, Prof. Jayanta Kapat for his encouragement, support and guidance in various aspects of my research work. I also thank him for the financial support provided during my coursework.

I am heartily thankful to my co-advisor, Dr. Shashi Verma for his valuable guidance in experimental techniques and research publications.

I am grateful to my dissertation committee members, Prof. Bhimsen Shivamoggi, Prof. Kareem Ahmed, and Prof. Subith Vasu for their valuable suggestions and patience during the course of preparation of my dissertation. In addition, I sincerely thank Prof. Bhimsen Shivamoggi for his encouragement, support and guidance in multiple aspects of my research and coursework.

I am heartily thankful to Prof. Ranganathan Kumar for his invaluable advise during my research and coursework.

I am extremely grateful to Prof. Challapalli Suryanarayana and (late) Prof. Suhada Jayasuriya for providing me Graduate Teaching Assistantship for multiple semesters during my coursework.

I am grateful to Prof. Hansen Mansy for his mentoring during my appointment as a Graduate Teaching Assistant for multiple semesters during my coursework.

I am thankful to Dr. Getnet Agegnehu, Application Engineer at CD Adapco for his valuable input on the computational model. I am grateful to Mr. Stephen Palluconi, research engineer at Innovative Scientific Solutions Inc., for his technical support with luminescent paint measurements.

I sincerely thank Dr. Brian Goldiez and Mr. Amit Goel at the Institute of Simulation and Training for their help with performing computations on STOKES Advanced Research Computing Cluster.

I owe my gratitude to the Siemens Energy Center research group and all my other colleagues for their help during the span of my stay at University of Central Florida.

I sincerely thank Dr. Jose Rodriguez at Siemens Energy for his valuable guidance during my appointment as a Graduate Research Assistant at the Siemens Energy Center.

I gratefully acknowledge the financial support received from Siemens Energy, Florida Center for Advanced Aero-Propulsion and Florida High-Tech Corridor for conducting my research work.

TABLE OF CONTENTS

LIST OF FIGURES

LIST OF TABLES

LIST OF NOMENCLATURE

A	area (m^2)
C	airfoil chord (mm)
D	film cooling hole diameter (mm)
d	wake rod diameter (mm)
DR	density ratio
h	heat transfer coefficient (W/ m^2 K)
I	momentum flux ratio
k	thermal conductivity (W/mK)
k^*	normalized turbulent kinetic energy $\left(\frac{1}{2}\left({u'_{s,RMS}}^2 + {u'_{n,RMS}}^2\right)/0.5U_\infty^2\right)$
L	entry length; film cooling hole length (mm)
M	blowing ratio/mass flux ratio
Ma	Mach number
N	number of film cooling holes; rotational speed of wake generator (RPM)
n	number of wake generator rods
P	pressure (Pa)
p	pitch (mm)
q	heat input; lateral heat conduction (W)
R	resistance of foil heater (ohm); radius of endwall (m)
Re	Reynolds number
S	wake Strouhal number; airfoil span (mm)

s	coordinate along airfoil chord (m)
T	temperature (°C/K)
Tu	turbulence intensity
U	mean velocity (m/s)
u	local velocity (m/s)
V	voltage (V)
w	width of the heater strip (mm)
x	streamwise coordinate (m)
y	wall-normal coordinate (m)
y^+	wall Reynolds number $\left(\frac{y\sqrt{\frac{\tau_w}{\rho}}}{\nu}\right)$
z	pitchwise coordinate ($z \cong R\Delta\theta$) (m)

Greek Symbols

α	film cooling hole inclination angle; temperature coefficient of resistance (K^{-1}); pitch angle of velocity vector
β	film cooling hole compound angle; yaw angle of velocity vector
γ	ratio of specific heats (c_p/c_v)
δ	boundary layer thickness (mm)
ε	emissivity
η	film cooling effectiveness
θ	pitchwise angle, cone angle of velocity vector
ν	kinematic viscosity (m^2/s)

ρ	fluid density (kg/m^3); resistivity of heater material (ohm-m)
σ	Stefan-Boltzman constant (5.67×10^{-8} W/m^2K^4)
φ	yaw angle, projected streamwise angle of film cooling hole
ϕ	roll angle of velocity vector
τ	shear stress (N/m^2)

Superscripts

$''$	per unit area
–	pitchwise-averaged
$'$	time-dependent value; auxiliary coordinate

Subscripts

1	displacement thickness
2	momentum thickness
∞	mainstream; free-stream
act	actual
amb	ambient
avg	average
ax	axial
b	backside
c	coolant
cond	conduction
conv	convection
e	exit

el	electrical
gen	generated
h	film cooling hole
in	inlet
inj	film injection location
is	isentropic
n	normal
o	baseline; stagnation condition
r	recovery
rad	radiation
s	static; surface; coordinate along airfoil chord
w	wire sensor; wall
l	local

Abbreviations

S_n	singlet state (n = 0,1,2,3…)
T_n	triplet state (n = 1,2,3…)
AR	aspect ratio (S/C)
CFD	computational fluid dynamics
CUC	cooling uniformity coefficient
CV	corner vortex
DR	density ratio
FCH	film cooling hole

fps	frames per second
IED	inner endwall
IT, IS	intersystem transition
LE	leading-edge
LED	light emitting diode
LHV	leading-edge horseshoe vortex
OED	outer endwall
PS	pressure side
PSP	pressure sensitive paint
PV	passage vortex
RMS	root mean square
SHV	suction side horseshoe vortex
SP	saddle point
SS	suction side
TSP	temperature sensitive paint
VR	velocity ratio

CHAPTER 1: INTRODUCTION

This chapter provides a brief background on gas turbines, their thermodynamic cycle, and the cooling methodologies that are practiced in modern gas turbines. Following this, endwall or platform cooling will be discussed in detail.

Gas Turbines

Gas turbines are cyclic heat engines widely used in propulsion, land-based power generation, marine and military applications. They have high specific power and are significantly low in emissions when compared to the conventional reciprocating engines. Almost, every modern aircraft is powered by a gas turbine. In addition, turbines contribute ≅ 98% of the total electricity that goes to the United States power grid [1]. These include coal, natural gas, nuclear, and renewable power sources (hydro, wind, solar-thermal). It is also noted that micro-turbines (miniature gas turbines) with power producing capacity ranging from 10s to 100s of kilowatts are considered to provide promising technologies to the hybrid electric vehicles. Some micro-turbines are also used for laboratory experiments in universities.

A large industrial gas turbine typically produces 100 to 400 MW of power and has 35–40% thermal efficiency under stand-alone cycle and 55-60% under combined cycle operation. Typically, industrial gas turbines have higher thermal efficiency than propulsion gas turbines. This is because of the thrust requirement in the latter case that keeps the work output of the turbine merely sufficient to the power the fan (in case of turbofan engines), compressor and small auxiliary power units. In addition, the aerodynamic losses are higher

in propulsion gas turbines due to increased coolant flow rate. The propulsion gas turbines have limitations on size and weight to reduce the flight load. In the case of industrial gas turbines, the size restriction is not a primary concern which permits the operation of dual or combined cycle gas turbine units (gas and steam turbine, for example).

Evolution of Gas Turbines

The earliest known concept of propulsion dates back to about 150 BC, when the Greek Mathematician Hero demonstrated the concept of a rotating sphere due to the reaction forces produced by the steam jets [2]. The first patent for a gas turbine engine was obtained by John Barber from United Kingdom in 1791 [2]. It consisted of a chain-driven, reciprocating type of compressor, a combustion chamber, and a turbine. Charles Gordon Curtis received the first gas turbine patent in the United States in 1899 [2]. The theory of gas flow past airfoils was studied by Alan Arnold Griffith resulting in a publication named, "An Aerodynamic Theory of Turbine Design" in 1926 [2]. In 1930, Sir Frank Whittle from England patented a gas turbine design for jet propulsion [2]. The world's first gas turbine for power generation was commissioned at Brown Boveri Company in Switzerland in 1939 [2].

The world's first aircraft to be powered by a turbojet engine was Heinkel He 178, which used Hans von Ohain's patented engine [2]. In 1942, the Junkers Jumo-004-B became the first large scale aircraft gas turbine to use air-cooled turbine blades [3]. From 1945 onwards, aircraft gas turbine development efforts have increased the turbine inlet temperatures, pressure ratios, component thermal efficiencies and fan by-pass ratios [3]. This has induced a corresponding increase in the thrust-to-weight ratios, durability and

reliability, thus reducing the specific fuel consumption. Other essential components of the development include production and maintenance costs, engine shut down times, and NO_x emissions [3].

Theory of Operation and Thermal Efficiency

The thermodynamic cycle of a gas turbine is called the "Brayton cycle" named after George Brayton who proposed it in 1870. In an ideal Brayton cycle, the heat addition and rejection are constant pressure processes as opposed to constant volume that occurs in a reciprocating engine (Otto cycle, for example). The process of combustion is continuous in a gas turbine which increases power output per cycle. The actual Brayton cycle on the h-s diagram for an industrial gas turbine is shown in Figure 1 and the jet propulsion cycle is shown in Figure 2. In Figures 1 and 2, the ideal or the isentropic states are shown using the subscript '*i*'.

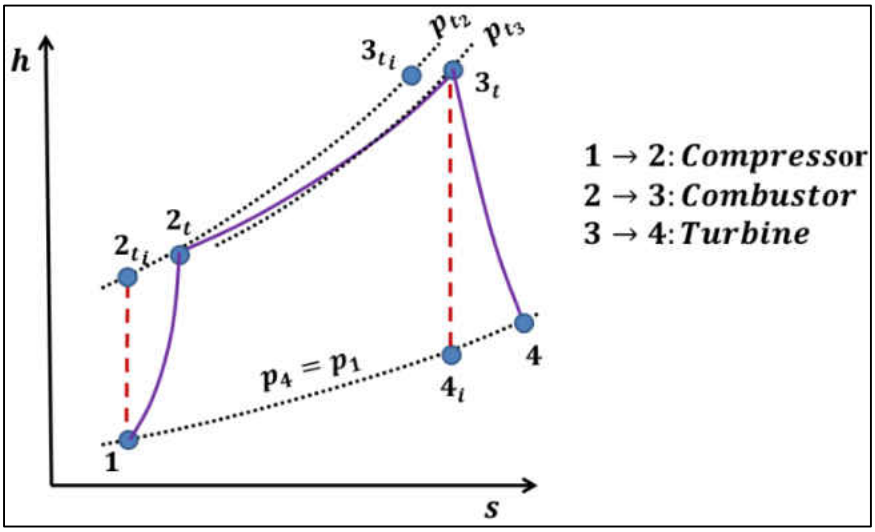

Figure 1: Actual Brayton cycle for an industrial gas turbine [4]

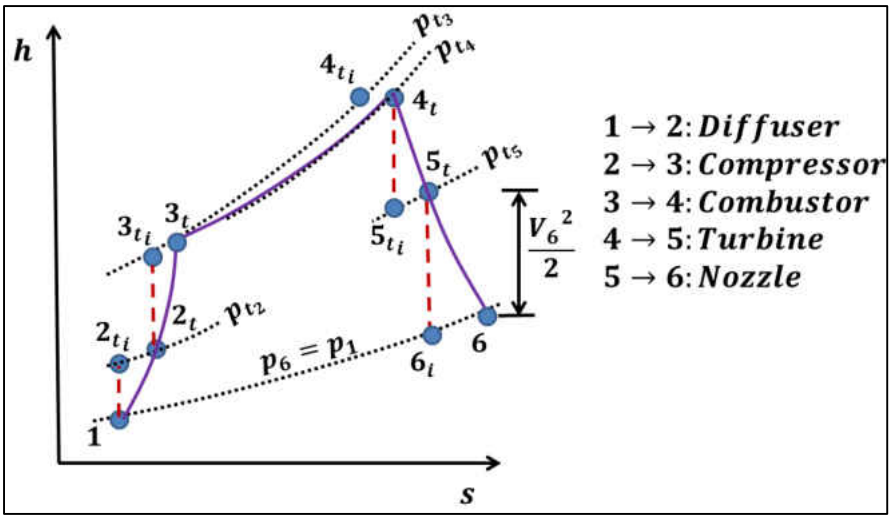

Figure 2: Actual Brayton cycle for a propulsion gas turbine [4]

In Figure 1, which describes a Brayton cycle for a power generation gas turbine, shows four processes. For the ideal case, the compression and expansion processes are reversible adiabatic (i.e. the entropy remains constant) and the pressure remains constant during heat addition. Typically the exhaust gas is vented to the atmosphere. Due to the entropy generation from non-isothermal heat transfer and other irreversibilities, the actual cycle deviates from the isentropic case, decreasing the thermal efficiency.

In a jet propulsion cycle (Figure 2), the compression and expansion processes are similar to the Brayton cycle. The useful work output of the turbine stage is negligible compared to an industrial gas turbine. This is because the primary goal in the case for a propulsion gas turbine is to increase the thrust. Due to this, the core thermal efficiency receives a lower priority. By accelerating the exhaust gases in a nozzle, the jet velocity is increased resulting in the required thrust. On the other hand, the thermal efficiency is a pertinent factor for power generation gas turbines. Since the temperature of turbine exhaust gases are high (~ 474°C in modern gas turbines) compared to the ambient temperature,

additional heat recovery is practiced mainly in large scale power generation gas turbines by passing the exhaust gases through a steam-generator to power a steam turbine. This type of dual thermodynamic cycle operation that involves a gas and steam turbine is called a "combined cycle" power plant whose efficiency can be > 60% in modern gas turbines [5].

Considering an ideal Brayton cycle for a power generation gas turbine, the thermal efficiency of the cycle is given in Equation 1.1 [6].

$$\eta_{th,Brayton_{ideal}} = \frac{w_{net}}{q_{in}} = 1 - \frac{q_{out}}{q_{in}} = 1 - \frac{T_4}{T_3}\left(\frac{1 - \frac{T_1}{T_4}}{1 - \frac{T_2}{T_3}}\right) \tag{1.1}$$

Since the processes $1 \rightarrow 2$ and $3 \rightarrow 4$ are isentropic, the isentropic relations can be used as shown in Equation 1.2.

$$\frac{T_2}{T_1} = \left(\frac{P_2}{P_1}\right)^{\frac{\gamma-1}{\gamma}} = \left(\frac{P_3}{P_4}\right)^{\frac{\gamma-1}{\gamma}} = \frac{T_3}{T_4} \tag{1.2}$$

Using Equation 1.2 in Equation 1.1 and using cold-air-standard assumptions, the thermal efficiency for an ideal Brayton cycle can be obtained as shown in Equation 1.3 [6].

$$\eta_{th,Brayton_{ideal}} = 1 - \frac{T_4}{T_3} = 1 - \frac{1}{\left(\frac{P_2}{P_1}\right)^{\frac{\gamma-1}{\gamma}}};\ \frac{P_2}{P_1} = r_p \tag{1.3}$$

From Equation 1.3, it is evident that the efficiency can be increased by increasing the pressure ratio (r_p). The performance of a Brayton cycle is usually evaluated using two factors namely, the thermal efficiency and the useful work output as pointed out by Wilson and Korakianitis [7]. The former increases with pressure ratio while the latter reaches a maximum at an optimum pressure ratio. It is essential to arrive at the optimum pressure ratio based on the gas turbine application. This optimum pressure ratio can be found for an ideal cycle by minimizing the derivative of the useful work with respect to the pressure

ratio. The pressure ratio for maximum useful work output is derived below based on [6]. The specific work (i.e. work per unit mass) is defined in Equation 1.4.

$$w_{net} = c_p[(T_3 - T_2) - (T_4 - T_1)] \tag{1.4}$$

Assuming constant properties for the gas and recognizing that the compressor inlet temperature is normally the ambient temperature and cannot be considered to be an important independent parameter in Equation 1.4, Equation 1.5 is obtained.

$$\frac{w_{net}}{c_p T_1} = \frac{T_3}{T_1}\left[1 - \frac{T_4}{T_3}\right] - \left[\frac{T_2}{T_1} - 1\right] \tag{1.5}$$

Using Equation 1.2 in Equation 1.5, Equation 1.6 is obtained.

$$\frac{w_{net}}{c_p T_1} = \frac{T_3}{T_1}\left[1 - \frac{1}{r_p^{\frac{\gamma-1}{\gamma}}}\right] - \left[r_p^{\frac{\gamma-1}{\gamma}} - 1\right] \tag{1.6}$$

In Equation 1.6 we can recognize $\frac{T_3}{T_1}$ as the temperature ratio parameter the upper bound being dictated by the highest turbine inlet temperature that the first turbine stage can withstand without failure. The graph for Equation 1.6 is shown in Figure 3. Component cooling has paved way for turbine inlet temperatures higher than the super-alloy melting temperature. Gas turbine cooling will be discussed in the next section of this dissertation.

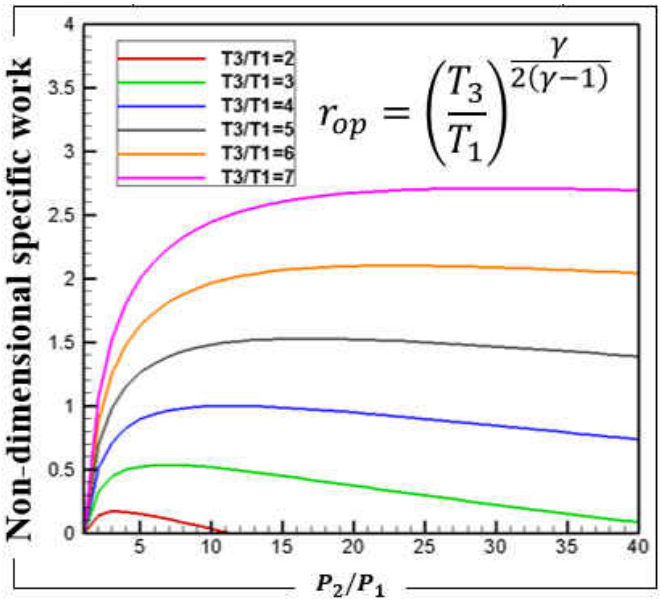

Figure 3: Non-dimensional work output dependence on pressure ratio [6]

It can be observed from Figure 3 that the maximum work output at higher turbine inlet temperatures shifts towards higher pressure ratios. This implies there must be an optimum pressure ratio for which the useful work output is the maximum. The optimum pressure ratio can be obtained by the maximization of the specific work output with respect to the pressure ratio for a fixed temperature ratio as shown in Equation 1.7.

$$\frac{d}{dr_p^{\frac{\gamma-1}{\gamma}}}\left(\frac{w_{net}}{c_p T_1}\right) = \frac{T_3}{T_1}\left(\frac{1}{r_p^{2\left(\frac{\gamma-1}{\gamma}\right)}} - 1\right) \tag{1.7}$$

For maximum useful work output, we need to have $\frac{d}{dr_p^{\frac{\gamma-1}{\gamma}}}\left(\frac{W_{net}}{c_p T_1}\right) = 0$ and $\frac{d^2}{d^2 r_p^{\frac{\gamma-1}{\gamma}}}\left(\frac{W_{net}}{c_p T_1}\right) < 0$. The first derivative of the non-dimensional specific work is given in Equation 1.8.

$$\frac{T_3}{T_1}\left(\frac{1}{{r_p}^{2\left(\frac{\gamma-1}{\gamma}\right)}}-1\right)=0 \tag{1.8}$$

The optimum pressure ratio for a fixed $\frac{T_3}{T_1}$ is given in Equation 1.9.

$$r_{op}=\left(\frac{T_3}{T_1}\right)^{\frac{\gamma}{2(\gamma-1)}} \tag{1.9}$$

Note that from Equation 1.8, we can see that $\frac{d^2}{d^2{r_p}^{\frac{\gamma-1}{\gamma}}}\left(\frac{W_{net}}{c_pT_1}\right)<0$.

From Equation 1.9, for a given temperature ratio and the type of gas (predominantly air), the optimum pressure ratio for the maximum specific work can be ascertained. Equation 1.9 can be rewritten to move the specific heat ratio exponent to the side of optimum pressure ratio as shown in Equation 1.10.

$${r_{op}}^{\frac{\gamma-1}{\gamma}}=\left(\frac{T_3}{T_1}\right)^{1/2} \tag{1.10}$$

Using Equation 1.2 in Equation 1.10, Equation 1.11 is obtained.

$$\left(\frac{T_2}{T_1}\right)^2=\frac{T_3}{T_1};\ \left(\frac{T_2}{T_1}\right)\left(\frac{T_3}{T_4}\right)=\frac{T_3}{T_1};\ T_2=T_4 \tag{1.11}$$

From Equation 1.11, it can be inferred that in order to progress towards the optimum pressure ratio, the compressor discharge and turbine exhaust temperatures must be as close as possible. For values of r_p between 1 and $\left(\frac{T_3}{T_1}\right)^{\frac{\gamma}{2(\gamma-1)}}$, the compressor discharge temperature will be less than the turbine exhaust temperature. In power plants with regeneration, the heat from the turbine exhaust is effectively utilized to increase the temperature of the compressor discharge air prior to combustion. Typical pressure ratios

used in land-based gas turbines are in the range of 15 to 25. The pressure ratios are higher than 40 in aircraft and military applications.

In summary, the need to increase the thermal efficiency and the specific work output of a gas turbine involves optimizing the pressure ratio for a fixed temperature ratio. The turbine inlet temperature is a key performance parameter and a minor increase in this value requires significant amount of engineering design and analysis to sustain component durability.

Gas Turbine Cooling

With increasing demands in turbine efficiency and net power output, the turbine inlet temperatures of the modern industrial gas turbines have reached approximately 1600˚C [5]. Cooling is widely practiced in gas turbines to increase component life. According to Han et al. [8], the life of a gas turbine blade can be approximately doubled if the mean blade wall temperature can be reduced by 28˚C. It is therefore extremely critical that turbine components are cooled continuously to sustain part durability. The gas turbine blades are manufactured by investment casting of super-alloys [9]. The typical thermal conductivity of a Nickel-based super-alloy (IN713LC) is approximately 10.3 W/mK at room temperature [9]. There have been significant improvements made in the field of turbine cooling over the last few decades. The underlying goal is to lower the maximum metal temperature. Figure 4 shows the advancement of cooling systems in gas turbine blades over the last five decades with increasing turbine inlet temperature.

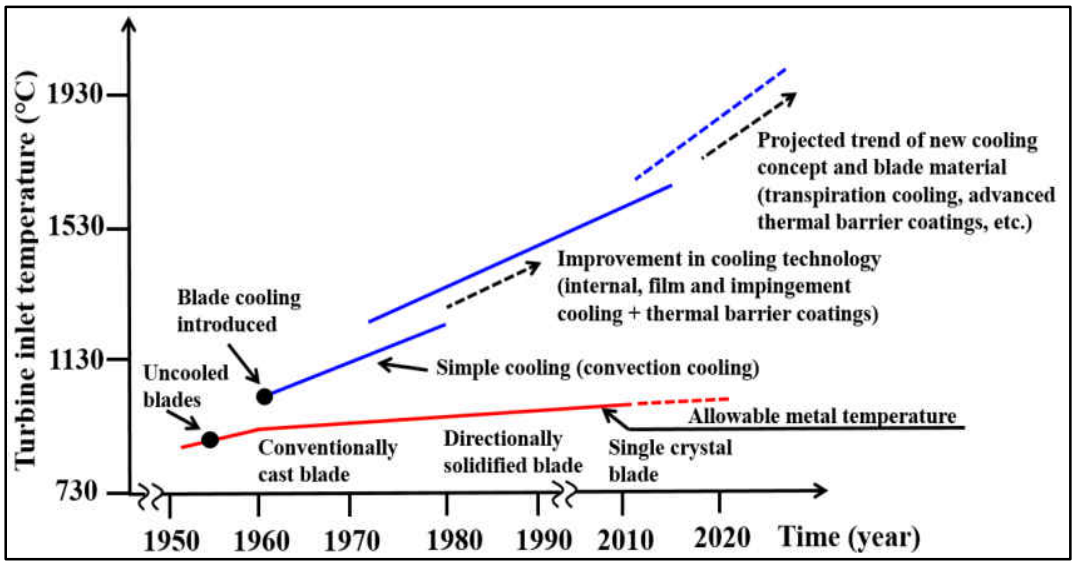

Figure 4: Advancement of gas turbine blade cooling systems [8]

Both internal and external cooling techniques are practiced in gas turbine components. The primary hot-gas-path components include the first stage nozzle guide vanes, rotors, and the associated endwalls (platforms). High pressure air, typically from the last few compressor stages is made to by-pass the combustor and is fed into internal cooling channels inside the hot-gas-path components. The compressor-bled airflow is cold relative to the mainstream flow, with the temperature difference being 337˚C approximately for the GE-E^3 engine for the first stage nozzle guide vanes [10]. It is noted here that the coolant temperature can differ based on the overall pressure ratio and operating conditions of the gas turbine.

Since the coolant bled from the compressor stage does not contribute towards useful turbine work, it is extremely essential to minimize the amount of cooling air in any gas turbine cooling scheme. Moreover, excess coolant increases the mixing losses in the engine which is detrimental to the thermal efficiency. A fundamental understanding of the coolant

behavior in a gas turbine is extremely essential for the design of efficient cooling schemes. The pertinent contributions to the thermal efficiency reduction from the theoretical limit and the importance of efficient cooling schemes and reduced losses is outlined in a simplified block diagram in Figure 5. A typical classification of gas turbine component cooling is shown in Figure 6.

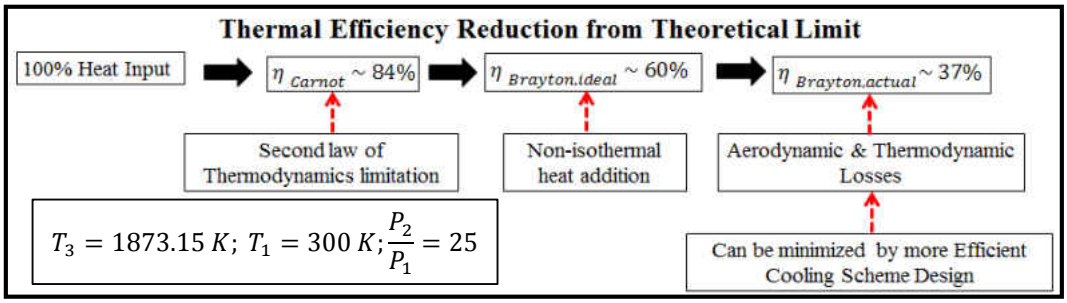

Figure 5: Simplified block diagram of gas turbine thermal efficiency reduction

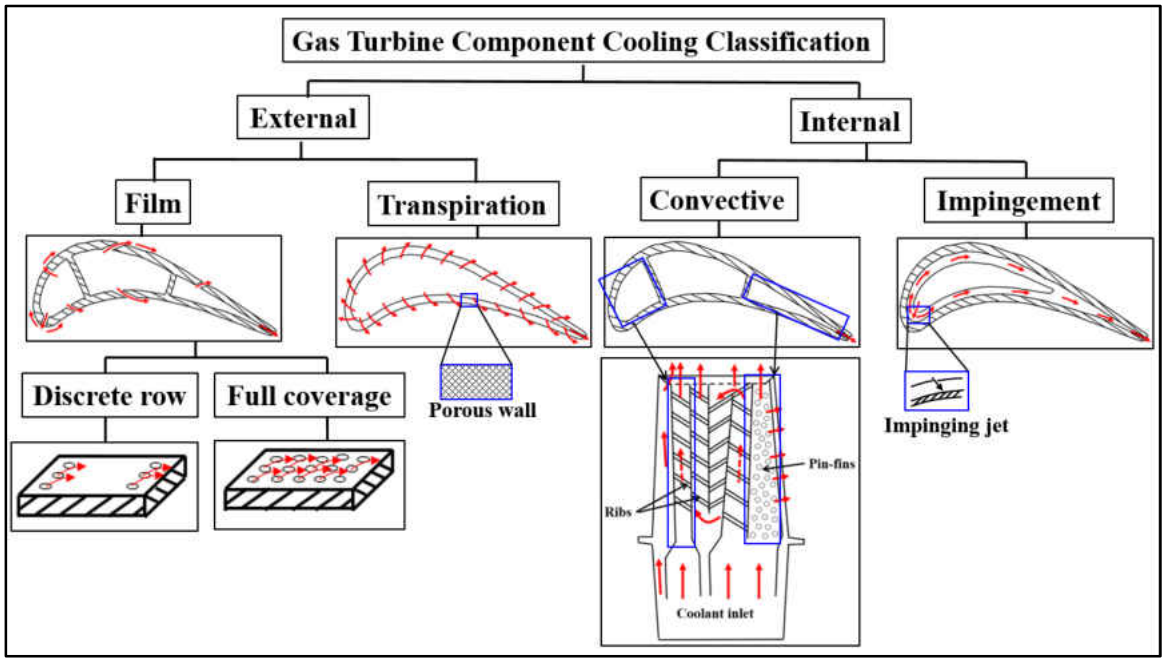

Figure 6: A typical classification of component cooling in gas turbines [11]

Any cooling technique must have a balance between its efficiency and the losses incurred to the turbomachine. In that respect, the elevated turbine inlet temperatures that can be achieved using a particular cooling technique become essential during the evaluation of its performance. Based on the type of gas turbine application, weight restrictions may also determine the feasibility of a cooling technique.

Internal Cooling

In internal (or convective) cooling, the passages inside the blade are usually roughened with turbulators. Typical turbulators include ribs and pin-fins. The turbulators increase the coolant residing time in the internal cooling passage by promoting flow mixing between the coolant the hot component wall thereby enhancing heat convection. Pin-fins are normally used near the trailing edge region of the airfoil in order to provide structural rigidity for the airfoil walls. Impingement cooling, which is a sub-category of internal cooling uses a surface with numerous holes through which high pressure air is ejected on to a hot (target) surface. The heat transfer coefficients on the target surface exhibit variation depending on the distance between the impingement holes and the target surface. Typically, impingement cooling is employed in areas which require high levels cooling (for example, the leading-edge of a first stage vane or blade). It is also noted here that the blade geometry itself imposes a constraint on the type of cooling that can be implemented.

External Cooling

After cooling the inside of the component, the coolant is ejected through discrete holes on the surface of the component that creates a relatively cold film over the target surface. This type of external cooling often called film cooling. The buffer layer (film) formed between the hot gas and the cooled surface reduces the temperature of the substrate (i.e. the maximum metal temperature). This type of cooling has permitted significant increase in turbine inlet temperatures over the past three decades. A typical stator-rotor and endwall cooling system in an aircraft gas turbine can be found in [11]. Transpiration cooling or continuous film cooling is a type of porous media cooling which has the potential to provide increased uniformity in the film coverage compared to discrete film injection in which hot spots can appear between the film cooling holes. Due to the challenges in the manufacturing of transpired components walls, the transpiration cooling technique is still under research and development.

In addition to the active cooling schemes, low thermal conductivity coatings called thermal barrier coatings (TBC) are applied to the components that need a large amount of cooling. An example of a thermal barrier coating used with Nickel-based superalloy is Yttria-stabilized Zirconia Polycrystal which has a thermal conductivity of ≅ 2 W/mK at room temperature [12]. Usually, the first stage nozzle guide vanes, blades and endwalls are coated with TBC since they experience the highest thermal and aerodynamic load in the engine. Thus higher turbine inlet temperatures are possible with TBC coatings while limiting the thermal exposure of the components. In combination with active film cooling, TBC's permit working fluid temperatures higher than the melting point of the super-alloy.

Endwall Film Cooling

The primary hot-gas path components as mentioned earlier include the first stage nozzle guide vanes, blades, and the associated endwalls. Film cooling practiced on the hot-gas path components have received significant attention in the past few decades. This is because of the strong secondary flow that dominates the endwall flow field thereby affecting the coolant trajectory and coverage. The ejected coolant interacts with the endwall secondary flow resulting in higher aerodynamic and thermodynamic losses. Increased losses are a penalty to the turbine stage efficiency and the extraction of cooling air from the compressor results in the reduction of the overall thermal efficiency. A typical gas turbine endwall film cooling configuration can be found in [3].

Due to the presence of alternating stator-rotor arrangement in a gas turbine, the mainstream flow is strongly influenced from the wakes (i.e. velocity deficits) shed by the vanes and blades. The endwall located downstream of a vane or blade is subjected to the wakes that are inherently unsteady. As the wakes convect downstream, they interact with the injected coolant. It essential to understand this interaction to quantify the influence of unsteady passing wakes on the coolant distribution on the endwall.

A substantial amount of research has been performed in the field of endwall film cooling. The next chapter will provide a comprehensive review of the published literature on film cooling studies relevant to the present investigation.

References

[1] “Annual Energy Outlook”, 2015, *U.S. Energy Information Administration*.

[2] Meher-Homji, C. B., 2000, “The historical evolution of turbomachinery”, *Proceedings of the 29th Turbomachinery Symposium,* Texas A & M University, Texas, USA.

[3] Friedrichs, S., 1997, “Endwall film-cooling in axial flow turbines”, *Ph.D. Dissertation*, Cambridge University, Cambridge, United Kingdom.

[4] Baskharone, E. A., 2006, "Principles of Turbomachinery in Air-Breathing Engines" Cambridge University Press, New York, USA.

[5] Mitsubishi Heavy Industries Ltd., 2011, “J Series Gas Turbine”, Technical Documentation, Yokohama, Japan.

[6] Saravanamuttoo, H. I. H., Rogers, G. F. C., Cohen, H., 2001, “Gas turbine theory”, 5th edition, Prentice Hall, New Jersey, USA.

[7] Wilson, D. G., and Korakianitis, T.P., 1998, "The Design of High-Efficiency Turbomachinery and Gas Turbines" Prentice Hall, New Jersey, USA

[8] Han., J. C., Dutta., S., and Ekkad., S. V., 2000, "Gas Turbine Heat Transfer and Cooling Technology" Taylor & Francis, Inc., New York.

[9] Zielinska, M., Yavorska, M., Poreba, M., and Sieniawski, J., 2010, “Thermal properties of cast nickel based superalloys”, *International Scientific Journal – World Academy of Materials and Manufacturing Engineering*, Vol. 44, pp. 35-38.

[10] Halila, E.E., Lenahan, D.T., and Thomas, T.T., 198 2. “Energy Efficient Engine.” General Electric Company (prepared for NASA CR-167955).

[11] “The Jet Engine”, 1996, *Rolls Royce PLC*, Derby, United Kingdom.

[12] “YTZP Tetragonal zirzonia polycrystal material properties”, 2013, Accuratus Ceramic Corporation, New Jersey, USA

CHAPTER 2: REVIEW OF LITERATURE

A comprehensive review of the film cooling technology has been provided by Goldstein [1] and Bogard and Thole [2]. Some of the topics discussed in these investigations include film cooling hole shape, coolant injection location, momentum flux ratio, mainstream turbulence, mainstream pressure gradient, and surface roughness. A more specific review on shaped hole film cooling was contributed by Bunker [3]. This chapter is split into several sections each providing a detailed review of the published literature related to film cooling on a flat plate, film cooling in the presence of unsteady passing wakes and film cooling on a gas turbine endwall.

Film Cooling on a Flat Plate

Some fundamental studies on film cooling were performed on a flat plate with zero pressure gradient. Eriksen and Goldstein [4] pointed out that the film cooling effectiveness at the centerline of the film hole increased with decreasing displacement thickness to film hole diameter ratio near the injection location. This was because of the greater momentum (due to the thin boundary layer) experienced by the film jet as it enters the mainstream. The effect of film hole geometry and density ratio on film cooling performance was studied by Goldstein et al. [5]. It was found that widening of the coolant channel near the exit of the film hole reduced the momentum of the exiting jet thereby keeping the jet well adhered to the surface and increasing the lateral spreading of the film jet. The orientation of a film cooling hole is shown in Figure 7.

Goldstein and Yoshida [6] observed that the inlet boundary layer was perturbed by the film holes and that the type of inlet boundary layer has meager influence on film cooling and heat transfer. In the work by Sinha et al. [7], the momentum flux ratio was found to be a better scaling parameter for film effectiveness in the jet lift-off regime, which was observed to occur at a momentum flux ratio greater than 0.3. The attached jet and partially detached jet (lift-off) scenario is shown in Figure 8 based on [7]. The effect of varying film-hole geometries including compounded holes and diffusing exits for a wide range of momentum, mass flux, and density ratios were studied by Bell et al. [8]. It was seen that the film holes with a combination of lateral diffusion and compound angle performed the best among the tested configurations. Hay et al. [9] observed that the lateral variation in the heat transfer augmentation was small past the streamwise location where the adjacent film jets started interacting with each other.

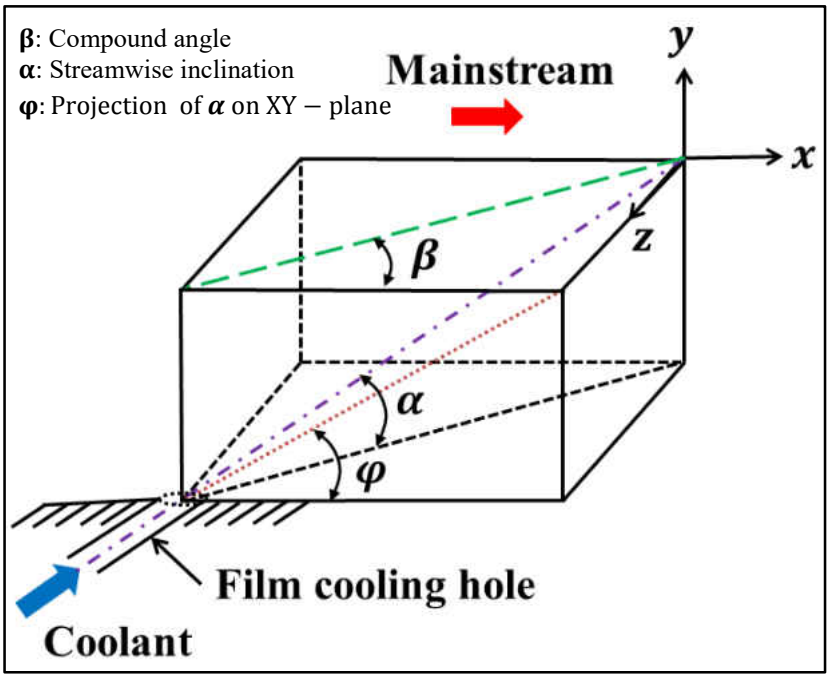

Figure 7: Film cooling hole nomenclature

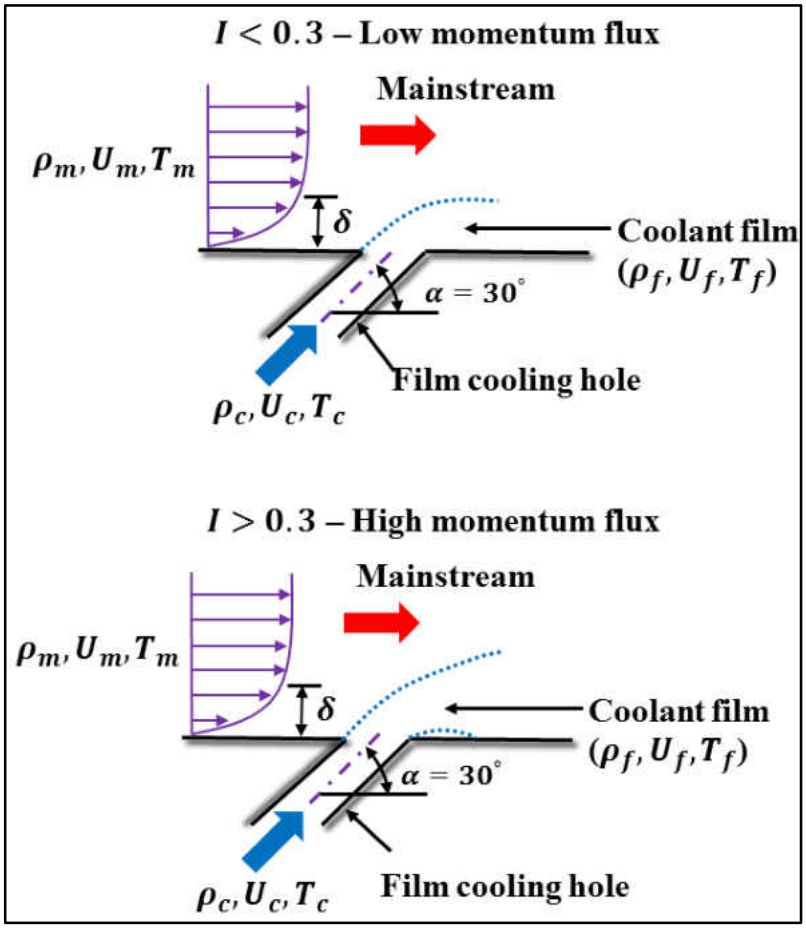

Figure 8: Coolant jet behavior at low and high momentum flux ratio [7]

In the study performed by Liess [10], it was observed that the mainstream Mach number had no measurable effect on the film cooling parameters up to a local Mach number of 0.9. Increasing displacement thickness to film hole diameter ratio was found to deteriorate the film cooling effectiveness. Pedersen et al. [11] showed that the effect of density ratio had a significant impact on the film cooling performance for holes with an injection angle of 35°. Lutum and Johnson [12] reported that film holes with length to diameter ratio less than 5 exhibited undeveloped flow character and a greater effective injection angle. This deteriorated the film cooling effectiveness.

An experimental study by Gritsch et al. [13] included the effect of cross flow Mach number in the coolant reservoir on film cooling performance. Their results showed that higher cross flow Mach numbers increased the turbulence intensity inside the ejected jet thus augmenting the laterally-averaged heat transfer coefficient about 10% for cylindrical holes and up to 30% for shaped holes. Goldstein and Taylor [14] used the heat-mass transfer analogy to measure heat transfer with film cooling. Their investigations indicated that high heat transfer coefficients occur between adjacent film holes mainly due to the jet-to-jet interaction. The behavior of the film jet at higher mass flux ratios were compared to a solid rod placed in a cross flow at the same film hole injection angle.

In a study by Ammari et al. [15], the heat transfer coefficients for film injection through normal holes (90° injection angle) exhibited no change when the density ratio was varied by keeping the mass flux ratio constant. When the film hole injection angle was reduced to 35°, a strong dependence on density ratio was exhibited by the heat transfer coefficient. The hydrodynamics of a row of film holes with an injection angle of 35° was studied by Pietrzyk et al. [16] on a flat plate for a density ratio of 2 and compared the results with two cases with density ratio of 1. They found that in the near hole region, the high density jets have lower velocities near the wall when compared to the jets with lower density. This reduces the relative momentum of the film jet with respect to the mainstream flow keeping it closer to the cooled surface.

Nasir et al. [17] observed that the film cooling effectiveness was lower for holes with higher injection angle. They also noticed that the compound angle film cooling holes produced lateral interactions of the film jet with the mainstream thereby resulting in high

heat transfer coefficients. The film cooling effectiveness in the far downstream increased for a compounded hole due to high lateral momentum of the film jet.

Experimental investigations on a flat plate performed by Yuen & Botas [18,19] indicated that the coolant film behavior can change dramatically when the fluid mechanics of the coolant film and the associated boundary layer are altered. The flow characteristics inside a film hole were studied by Walters and Leylek [20] who found the existence of a region of accelerating flow near the exit of the coolant hole and recirculating flow (wake region) under the film hole at higher coolant-to-mainstream mass flux ratios. They also showed the production of vorticity inside the boundary layer of the film hole that gives rise to the counter-rotating vortex pair. They also found that increasing distance between the streamwise vorticity pockets reduces the lift and strength of the vortical structures. There are two major parts of a vortex structure namely the up-wash and down-wash side, which was observed in the flat plate film cooling experiments performed by Ligrani and Williams [21] and Ligrani et al. [22]. The former decreases film cooling while the converse is true in the latter case.

The effect of both unsteady wakes and pulsed jets on film cooling were studied by Womack et al. [23] on a flat plate with a wall-tangential wake rod orientation. They noticed a reduction in film effectiveness when both pulsed jets and wakes were introduced. It was observed that at lower wake passing frequencies, the timing of the wake had a significant impact on the time-accurate film effectiveness measurements whereas at higher wake passing frequencies, the effect of wake timing was negligible. In another similar flat plate investigation with periodic wakes, Womack et al. [24] observed that the heat transfer coefficients increased with the wake passing frequency by the same order as with and

without film cooling. The test surface recovered completely from the passing wake disturbance at low Strouhal numbers but this recovery reduced with increasing wake passing frequency.

Influence of Unsteady Wakes on Film Cooling

Since a gas turbine turbine endwall is continuously exposed to wake shedding from upstream stators and rotors, it is necessary to understand the effects of unsteady passing wakes on film cooling and heat transfer. There is a need here to simplify the existing situation of the complex flow field by considering the passing wake influence on an endwall without airfoils. This enables to isolate the effects of secondary flows that are generated in a cascade and focus the attention on the unsteady passing wake effect only. This is the motivation behind the first part of this research work. This section provides a detailed discussion on the relevant passing wake studies that are part of the open literature.

Schobeiri et al. [25] conducted tests on a concave plate with an upstream wake generator and observed a wake-induced boundary layer transition and a quasi-steady primary boundary layer which was periodically disturbed by the wakes. Du et al. [26, 27] found that trailing edge ejection from a rotating wake rod compensated for the velocity deficit caused by the periodic wakes. The trailing edge coolant ejection was observed to have a stronger effect on film effectiveness than on airfoil heat transfer coefficients. Unsteady wakes were seen to increase the heat transfer coefficients slightly on a film cooled blade.

On the other hand, the film cooling effectiveness deteriorated with the introduction of unsteady wakes. Han et al. [28] found that the blade heat transfer coefficients increased

with the Strouhal number when the mainstream Reynolds number was held constant. The Reynolds number (length scale based on the airfoil chord) and Strouhal number (length scale based on the wake rod diameter) were both considered essential parameters in understanding the airfoil heat transfer [28].

In a numerical investigation of wake influenced shower-head film cooling by Adami et al. [29], it was found that the wake has a considerable impact on the coolant flow mixing and separation near the surface while the effect on the overall flow field was not significant. The velocity fluctuations due to the wake and mainstream turbulence were damped out more on the suction side than the pressure side due to the local positive curvature near the airfoil leading-edge. Dullenkopf et al. [30] found that the unsteady wakes have a significant influence on the boundary layer on the suction side of an airfoil. Apart from this, the unsteady wakes were observed to have a vital effect on the average heat transfer coefficient in the laminar-turbulent boundary layer transition regime.

Teng et al. [31] found that unsteady wakes play a predominant role in determining the boundary layer transition while a single row of film holes do not have a notable influence on the transition. The jet lift-off phenomenon was observed by Funazaki et al. [32] for an average mass flux ratio greater than 0.8 and a density ratio of 0.93 for film holes located near the stagnation region of a blunt body. This was because the local mass flux ratio at the film hole exit was much higher due to the decreased local mainstream velocity in the airfoil stagnation region. The influence of the passing wake was negligible at low mass flux ratios. Both turbulence intensity and the turbulence length scale of the mainstream were considered to be important factors in dictating the film cooling performance.

The effect of stationary wakes on endwall film cooling near the airfoil leading-edge junction was studied by Rodriguez et al. [33]. At lower streamwise distances downstream of film injection, the wakes were found to increase the film effectiveness. But due to strong mixing with the coolant, the decay rate of the film effectiveness increased in the presence of stationary wakes. An experimental and numerical study by Heidmann et al. [34] showed that not resolving the flow within the film holes can over predict the film effectiveness since the flow field inside the coolant hole had a substantial influence on the jet trajectory. It was also seen that the passing wakes influences the film jets by augmenting their lateral mixing.

Ou et al. [35] studied the effect of unsteady wakes on the blade heat transfer in a linear cascade at a density ratio of 1.5 and unity. The high density coolant increased the heat transfer coefficient in the transition region but did not have much influence on most part of the suction and pressure side of the airfoil. Film injection alone was seen to increase the heat transfer coefficient more than just the passing wake. Mehendale et al. [36] performed heat transfer and film cooling experiments in the same facility as Ou et al. [35]. On the pressure side of the airfoil, the high density coolant was noticed to perform much better than the low density coolant. The reason for this is due to the very low the mainstream velocity near the airfoil pressure side that increases the momentum flux ratio. With a higher density coolant, the velocity ratio reduces which in turn decreases the momentum flux ratio.

Wright et al. [37] used stationary rods and delta wings to mimic the combined effect of trailing edge wakes and upstream passage vortices in a linear cascade of airfoils. Among the 30° and 45° delta wings used to generate upstream passage vortices, the secondary

flows generated by the delta wings at 45° incidence angle were observed to cause greater detriment to the slot coolant.

From the discussed published literature, it is observed that most of the passing wake investigations conducted have been confined to flat plate or cascade studies. The first part of the present research investigation stands in-between flat plate and cascade flow studies providing information on film cooling effectiveness and heat transfer on a pitchwise-curved surface influenced by passing wakes. The wall-normal wake rod orientation in a sector-annular duct provides a realistic experimental setup in connection with a gas turbine endwall in the absence of airfoils. It should be noted that the velocity components (axial & tangential) of the passing wake are retained in its entirety when investigated in an annular channel as opposed to a rectangular channel. A schematic in Figure 9 shows the difference between a wall-normal and wall-tangential wake-rod orientation.

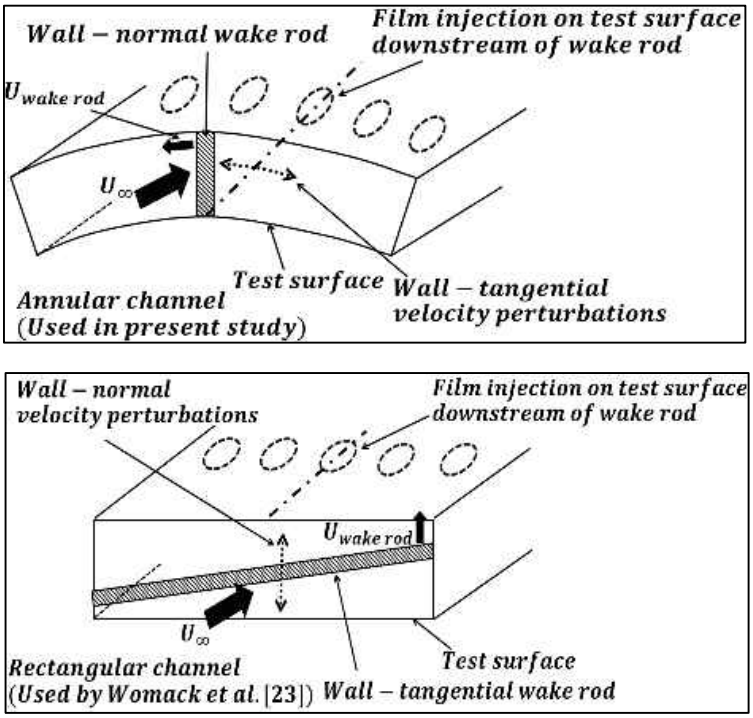

Figure 9: Difference between wall-normal and wall-tangential wake rod orientation

The results obtained from this investigation will provide information on the film effectiveness and heat transfer distribution on an endwall without airfoils with wall-normal wake rod orientation. The following section will focus on endwall secondary flows, endwall film cooling and heat transfer studies reported in the published literature.

Endwall Secondary Flow System

The endwall flow field is highly complicated and three-dimensional. Due to the non-uniform velocity distribution in the flow approaching the airfoils, there exists a spanwise stagnation pressure gradient with the lowest stagnation pressure occurring near the endwall. This results in a downward flow approaching the endwall that rolls up into a horseshoe vortex near the airfoil leading-edge. In addition, the flow turning due to the non-zero airfoil camber produces cross flow (i.e. flow from the pressure side to the suction side of the airfoil) inside the airfoil passage which leads to the migration of the horseshoe vortex to the suction side.

The cross flow fed pressure side horseshoe vortex is called the passage vortex. The suction leg of the horseshoe vortex stays close to the airfoil suction surface and has an opposite rotational motion compared to the pressure side branch. A typical endwall secondary flow system is shown in Figure 10. These secondary flows can have a significant influence on the film cooling effectiveness and heat transfer coefficient distribution on the endwall. Particularly, the airfoil leading-edge-endwall junction and the path of the passage vortex inside the airfoil passage experience high heat transfer coefficients and hence need adequate cooling to maintain part durability.

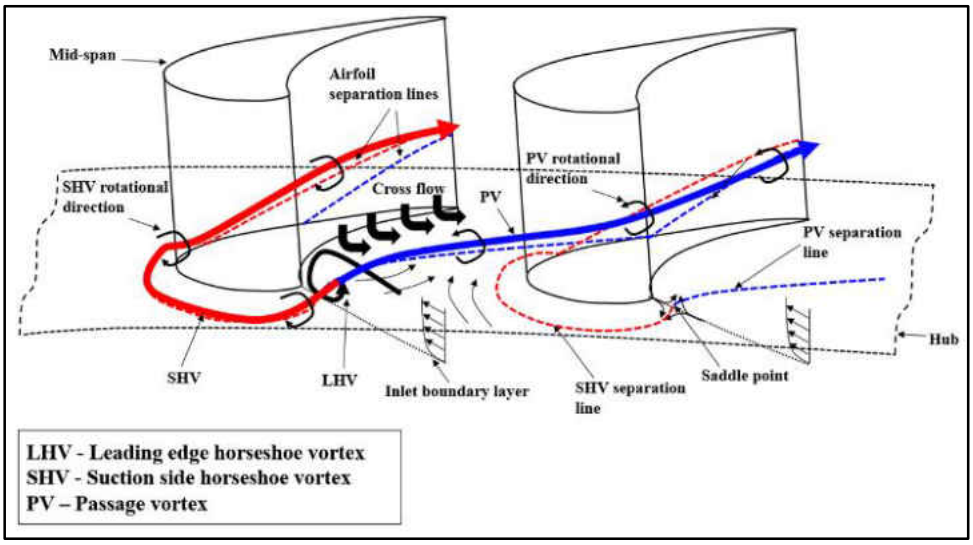

Figure 10: Simplified schematic of an endwall secondary flow system [47,55]

One of the earliest studies on the classical secondary flow theory was reported by Hawthorne [38]. This model presents the streamwise vorticity components arising due to the distortion of the vortex filaments in the inlet boundary layer leading to the generation of the passage vortex. The leading-edge or the stagnation point vortex was first identified by Klein as pointed out by Sieverding [39], who has summarized the research performed on the basic aspects of secondary flows in airfoil passages between 1975 and 1985. Several investigations have been made in the field of flow visualization and pressure loss measurements in cascade flows [40-47].

It was noted by Moore and Smith [40], Sieverding and Van den Bosch [41], and Langston et al. [42] that the injected fluid along the pressure side ended in the core of the passage vortex and the suction side fluid surrounded the passage vortex with an opposite rotational motion. Sjolander [43] measured the total pressure at various streamwise planes along the airfoil passage to calculate the losses incurred due to the vortical flows. The

losses were seen to be high near the suction side due to the pitchwise migration of the passage vortex.

Harrison [44] performed measurements of endwall shear stress and streamwise vorticity in a high turning linear cascade. They observed that the boundary layer on the endwall was affected both upstream and downstream of the separation lines. The loss core of the passage vortex was highest at the exit plane of the cascade. Gregory-Smith and Graves [45] reported that the secondary loss growth exhibited close to a steady behavior through the cascade. This finding was opposite to Langston et al. [42] and Marchal and Sieverding [46] who found the losses to remain the same up to the axial location of highest suction velocity and increased rapidly thereafter due to the interaction of the endwall cross flow and the airfoil suction surface boundary layer. A comprehensive discussion on the loss mechanisms in turbomachines was provided by Denton [47] where the author points out that the secondary flow losses contribute to almost one-third of the total losses in a turbomachine.

Secondary flow reduction is another important aspect of endwall film cooling. A passive method of reducing the endwall secondary flows is to use a fillet at the airfoil leading-edge-endwall junction. The fillet reduces the pitchwise pressure gradient by accelerating the flow near the airfoil pressure side thereby altering the size and location of the vortex structures. Many researchers have studied the usage of fillet and its impact on the cascade aerodynamics and heat transfer. Only few recent studies are mentioned here. Mahmood and Acharya [48] investigated the effect of a linear and a parabolic fillet on the cascade flow field and heat transfer. They found that the fillet weakened the passage vortex and reduced the endwall heat transfer compared to the no fillet case. Praisner et al. [49]

studied the application of non-axisymmetric contouring to the endwall of high lift low pressure turbine airfoils. It was observed that the secondary flow losses associated with the passage vortex were reduced with the introduction of a contoured endwall. Abraham et al. [50] conducted experiments in a transonic cascade with two contoured endwalls optimized for aerodynamics and heat transfer respectively. They found that the mixed out secondary flow losses, one airfoil chord downstream of the trailing edge reduced by 17% with the introduction of the endwall optimized for aerodynamics.

Endwall Film Cooling

Film cooling effectiveness is a non-dimensional temperature ratio which provides a measure of coolant concentration on the surface. Various research groups have performed effectiveness measurements using discrete film and slot injection on an endwall.

Initial research investigations in film cooling focused on studying the impact of the coolant injection on the secondary flows [51-53]. The effect of pitchwise blowing upstream of the airfoil leading-edge was investigated by Biesinger and Gregory-Smith [51], who observed that increased blowing re-energized the inlet boundary layer thereby promoting counter-streamwise vorticity which causes progressive weakening of the passage vortex. On the other hand, excess blowing was seen to be detrimental in terms of increasing the mixing losses in the passage. In high turning cascades, the effect of coolant injection altered the flow angles significantly based on the blowing ratio as reported by Sieverding and Wilputte [52] and Goldman and McLallin [53], who also showed that the depth of the loss core of the passage vortex was mitigated at higher coolant flow rates.

One of the earliest studies reported in film effectiveness measurements was by Blair [54] who performed measurements in an airfoil passage of a linear cascade. It was seen that the film effectiveness deteriorated near the pressure side due to the disturbance caused by the secondary flows. A similar finding was reported by Takeishi et al. [55]. Harasgama and Burton [56] performed endwall film cooling effectiveness measurements at engine conditions in an annular cascade. It was reported that positioning of the film cooling holes along the iso-Mach lines provided a uniform momentum flux ratio. In a companion paper, Harasgama and Burton [57] observed that when the axial pressure gradient correction was made to the endwall film effectiveness distribution, it came closer to the flat plate correlations with discrete film injection. It was also found that film injection alters the endwall streamlines significantly depending on the momentum flux ratio.

The effect of a non-uniform inlet velocity and temperature profile in a cascade was discussed by Lakshminarayana [58] who showed that the direction of rotation of the passage vortex was altered depending on the combination of inlet velocity and temperature profile. This resulted in the change of sign in the radial total pressure gradient. Friedrichs et al. [59-61] studied the aerodynamic aspects of film cooling and the coolant distribution in a low speed linear cascade. It was found that the continuously varying static pressure across an airfoil passage altered the local blowing ratio significantly. The coolant injection upstream of the lift-off lines was noticed to have a substantial influence on the secondary flow strength and its associated losses.

Barigozzi et al. [62] studied the effect of coolant flow rate on the aero-thermal performance in a higher pressure rotor airfoil cascade using discrete film holes employed near the airfoil pressure side. In terms of the aerodynamic losses, it was found that the

ejected coolant did not have any significant influence on the downstream flow field. It was found that varying the coolant mass flow rate did not affect the secondary flows significantly. This can be explained due to the location of the film holes in the passage as pointed out by Friedrichs et al. [60]. In the study by Liu et al. [63], the spatially averaged film cooling effectiveness was reported to be doubled in the case of double row film injection upstream of the airfoil leading-edge. A triangular shaped uncooled region between the airfoil pressure side and the vortex lift off line was seen to be diminishing as the coolant mass flux increased to approximately twice the mainstream mass flux.

Jabbari et al. [64] experimented discrete film injection inside an airfoil passage of a low speed planar cascade. It was observed that the film cooling hole spacing, local mainstream velocity direction, blowing ratio, and the density ratio significantly affected the film cooling jet behavior and thereby the coolant distribution. Goldstein and Chen [65] investigated the film cooling of a turbine blade due to the effect of endwall secondary flow. The sweeping of the coolant from the suction side due to the suction side horseshoe vortex results in an uncooled triangular region. On the other hand, the airfoil pressure side was observed to less influenced by the endwall secondary flow. It was found that the film cooling effectiveness was closely linked to the local mainstream flow behavior. A combination of the mainstream flow conditions and the airfoil geometry were considered responsible for the strength and location of the secondary flows.

Some of the computational investigations for endwall film cooling have been performed by Friedrichs [66], Hada and Thole [67], Hermanson and Thole [68], Lynch et al. [69], and Knost and Thole [70]. It was found that the predictions agreed reasonably well with the experimental results, especially from the coolant coverage perspective [67]. In the

study by Hermanson and Thole [68], computational predictions were performed to investigate the inlet velocity and temperature profile effects on secondary flows. The results reported were qualitatively similar to Lakshminarayana [58]. Lynch et al. [69] found that the total pressure loss and heat transfer distribution were over-predicted by the computational model whereas the film cooling effectiveness and secondary kinetic energy were found to be in good agreement with the experiments.

As discussed in the review of shaped holes [1], fan-shaped holes increase the lateral spreading of the coolant jets thereby enhancing the effectiveness. The study conducted by Colban et al. [71] involved comparing cylindrical and fan-shaped holes under low and high mainstream turbulence conditions. It was seen that the fan-shaped holes increased the area-averaged cooling effectiveness by 75% more than the cylindrical holes. This was attributed to the decrease in the local blowing ratios of the fan-shaped holes in comparison with the cylindrical holes. The effect of high mainstream turbulence on the cylindrical holes was to slightly increase the film effectiveness since the turbulent mixing of the jet helps to have higher lateral spreading. For the fan-shaped holes, the effect of higher mainstream turbulence slightly increased the film effectiveness but followed a similar trend as the low turbulence cases at higher coolant flow rates.

Barigozzi et al. [72] performed experiments using fan-shaped holes with different area-ratios. It was seen that lower area-ratio holes performed better in terms of secondary losses. This was attributed to the higher momentum of coolant jet that reduced the secondary flow strength. Various airfoil loading conditions were studied by Kunze et al. [73] to understand its impact on film effectiveness downstream of a single row of fan-shaped holes. At higher incidence angles, which typically represent engine off-design

conditions, the secondary loss region was found to grow in the radial and the pitchwise directions due to intensification of the secondary flow. A second loss peak appeared in the loss coefficient contour positioning itself close to the passage vortex. This was considered to be representing the trailing edge vortex.

Some investigations have been performed with trenched film cooling holes, film cooling slots (representing the combustor-turbine interface) or a combination of slot and discrete film cooling holes. A few of them are discussed here. Sundaram and Thole [74] performed endwall film cooling studies using trenched holes and observed that the coolant stayed attached to the surface until $M_{avg} = 2.5$ due to the low exit momentum flux compared to the discrete film holes. Since the edge of the trench acts like a wall, the coolant is forced to spread laterally thereby enhancing the effectiveness.

Zhang and Jaiswal [75] performed experiments with a double-staggered row of discrete film holes or slots located upstream of the airfoil leading-edge. A higher cooling uniformity was obtained with slot injection at increased blowing ratios. The dominating effect of the secondary flow was almost unchanged for both the slot and the discrete hole injection at the lower blowing ratios. At higher blowing ratios, the secondary flow was suppressed due to the increased coolant momentum.

Knost & Thole [76] studied film cooling effectiveness in the presence of leakage flow from the combustor-turbine interface along with two distinct discrete film cooling hole patterns. The first hole pattern used the iso-Mach lines to locate most of the film cooling holes while the second hole pattern followed the iso-Mach lines only for few downstream holes. It was noticed that for the discrete film injection cases, an uncooled region was present in the center of the passage for pattern 2. This uncooled region was not

present in the case of pattern 1 due to the uniformity in the blowing ratio of the holes located on the same iso-Mach line. Including slot injection in addition to the discrete film resulted in an overcooled region in the center portion of the passage inlet. The authors pointed out that caution must be used while determining the film cooling hole locations in a combined slot and discrete film injection scenario to avoid excessive use of coolant.

Wright et al. [77] performed an experimental investigation of a combined slot and discrete film cooling configuration in a linear cascade. The slot was located near the airfoil leading-edge and the discrete film cooling holes were employed downstream in the airfoil passage. The authors found that the slot injection weakened the passage vortex at blowing ratios greater than unity. In addition, increased mainstream turbulence was found to weaken the passage vortex thereby increasing the film cooling effectiveness.

Heat transfer and film cooling effectiveness measurements in a transonic linear cascade were conducted by Nicklas [78]. The coolant injection was provided using a slot or discrete film cooling holes. It was found that the slot injection intensified the leading-edge horseshoe vortex which resulted in high heat transfer coefficients near the leading-edge. The trailing edge wake region was noted to be extremely difficult to cool without introducing trailing edge cooling holes.

Milidonis and Geogiou [79] investigated a slot injection configuration at the leading-edge of a symmetric bluff body near the endwall junction. The coolant trajectory was seen to be assisted by the return leg of the leading-edge horseshoe vortex. It was observed that the coolant film extended for a radial distance of almost half the radius of the bluff body leading-edge and for a 30° circumferential distance from the bluff body leading-edge. Mensch and Thole [80] studied film and impingement cooling separately and a

combination of film and impingement cooling in adjacent airfoil passages of an endwall in a linear cascade. The film cooling holes were oriented along the local flow direction. The average discharge coefficient of the film cooling holes exhibited an increase with the blowing ratio. High film effectiveness was observed in the immediate downstream region of the film holes after which the endwall cross flow disturbed the uniformity in the film effectiveness distribution.

The effect of both coolant plenum and mainstream cross flow on film cooling hole discharge coefficient was investigated by Gritsch et al. [81] in a flat plate film cooling experiment. By varying both the inclination and compound angle of the film cooling hole, the impact on the hole discharge coefficient was studied. It was found that the discharge coefficient was profoundly affected by the coolant plenum and mainstream cross flow conditions in addition to the coolant to mainstream pressure ratio. Increasing the inclination or compound angle of the film cooling hole resulted in reduced discharge coefficients due to the higher losses at the inlet than the exit of the coolant hole.

Rowbury et al. [82] reported a scaling methodology of film cooling hole discharge coefficients from experiment to engine conditions. The experiments were conducted in a large scale annular cascade. It was shown that by means of dimensional analysis, the film cooling hole discharge coefficients depend on the coolant to mainstream pressure ratio and the coolant jet Reynolds number.

The published literature on endwall film cooling contains studies performed at both engine and non-engine conditions. Although the coolant jet behavior at a density ratio less than 1.2 cannot be directly applied to understand the flow physics at engine conditions where the density ratios are typically between 1.5 and 2, the scientific methodology used

in the present investigation for understanding the impact of coolant injection on secondary flow and vice versa can be adapted to analyze the flow physics in an engine scenario.

Endwall Heat Transfer

In addition to the substantial impact on film cooling effectiveness, the endwall secondary flows also contribute to high rates of heat transfer mainly because of the increased mixing between the near-wall fluid and the mainstream flow. Several experimental investigations have been carried out to measure heat transfer coefficients on airfoils and endwalls.

Blair et al. [54] conducted endwall heat transfer experiments in a large scale linear cascade. It was found that due to the presence of a corner vortex at the junction of the airfoil suction side and the endwall, the heat transfer distribution exhibited significant variations inside the airfoil passage in the trailing edge region. Introducing film injection or changing the location of inlet boundary layer transition did not have a noticeable impact on the corner vortex. Endwall and airfoil heat transfer measurements were performed by Takeishi et al. [55] in a low-speed annular cascade of nozzle guide vanes. It was found that the secondary flows upstream and inside the airfoil passage had a significant impact on the heat transfer distribution on the endwall and the airfoil suction surface. On the other hand, the secondary flows were found to have little influence on the heat transfer distribution on the airfoil pressure surface. The heat transfer in the airfoil leading region was increased by the horseshoe vortex.

Harasgama and Burton [56] conducted heat transfer measurements in an annular cascade at engine representative mainstream and coolant flow conditions. It was observed

that film injection decreased the heat transfer rate by 50-75% over most of the endwall area for the high blowing ratio cases. The airfoil pressure side corner was observed to experience high heat transfer rates even with film injection due to the passage vortex that removes the coolant from the endwall. A thin boundary layer is formed in this region which is highly skewed and contributes to increased heat transfer rates.

Liu et al. [63] conducted endwall heat transfer measurements in a large scale linear cascade. The heat transfer coefficients on the endwall increased remarkably in the presence of film cooling since the film jets promote turbulent mixing with the mainstream flow. In a study by Kang et al. [83], the sweeping of peak heat transfer across the blade passage from the airfoil pressure side to the suction side on the endwall due to the impact of the cross flow on the passage vortex was reported. The skewed boundary layer that is formed downstream of the separation lines leads to high heat transfer coefficients due to high shear stresses in this region.

Thole and Knost [84] compared the local heat transfer augmentation along three individual streamlines at the pressure, mid-pitch, and suction side of the passage. It was noted that there was little difference between the pressure and suction side locations at the inlet to the passage. Further downstream of the passage, the suction side heat transfer increased beyond the pressure side due to the passage vortex which migrates towards the suction side. The authors point out that the heat transfer augmentation could be severely under predicted if any two-dimensional boundary layer calculations were used.

Endwall heat transfer measurements at engine representative Reynolds and Mach numbers were performed by Spencer et al. [85] in an annular cascade of nozzle guide vanes. They found that the heat transfer coefficient increased along the passage due to the

acceleration of the mainstream flow. The horseshoe vortex was found to create a region of high heat transfer near the suction side due to its lift-off from the hub surface. The pitchwise and spanwise pressure gradients in the airfoil passage affect the pattern of the secondary flows and their position thereby influencing the heat transfer characteristics. Boyle and Russell [86] performed an experimental investigation of endwall heat transfer in a linear cascade for a wide range of Reynolds numbers. At low Reynolds numbers, the heat transfer pattern was found to be close to the inviscid streamlines at the airfoil midspan. On the other hand, the high Reynolds number cases exhibited significant differences from the inviscid streamlines. The heat transfer coefficients at high Reynolds numbers were found to correlate well with the local mainstream velocity. The magnitude of the heat transfer coefficients showed noticeable variation with changes in the thickness of the inlet boundary layer.

Graziani et al. [87] performed endwall and airfoil heat transfer experiments in a large scale turbine blade cascade for two inlet boundary layer thickness values. The results showed that the heat transfer distribution on the airfoil suction side and the endwall was strongly influenced by the passage secondary flows. The secondary flows were found to have negligible impact on the airfoil pressure side heat transfer distribution. Variation in the cascade inlet boundary layer thickness was seen to influence the airfoil suction side and endwall heat transfer distribution significantly. Due to the strong three-dimensionality in the cascade flow field, the applicability of conventional boundary layer calculations were considered questionable [87].

Goldstein and Spores [88] investigated the heat transfer distribution in a linear cascade using the mass transfer analogy. It was found that the presence of the leading-edge

horseshoe vortex increased the heat transfer coefficient significantly near the stagnation region of the airfoil. Apart from this, the heat transfer distribution varied greatly inside the airfoil passage due to the presence of branches of the leading-edge horseshoe vortex.

Harvey et al. [89] studied the endwall heat transfer in an annular cascade using thin film heat flux gauges at engine representative Mach and Reynolds numbers. They found that the sweeping of the inlet boundary layer upstream of the endwall separation lines resulted in the convergence of streamlines near the airfoil suction side, reducing the heat transfer in that region. The location of passage vortex formation near the leading-edge, the pressure side trailing edge region, the sweeping path of the new boundary layer from the airfoil pressure side to the suction side were observed to be high heat transfer zones. Downstream of the airfoil passage, it was seen that the growing boundary layer and flow diffusion reduced the heat transfer.

Measurements of heat transfer performed by Chana [90] in an annular cascade of nozzle guide vanes showed high heat transfer mainly near the airfoil trailing edge region. This finding was different from those reported by [85-88] who found high heat transfer values at many locations inside the airfoil passage. The heat transfer levels were augmented with the increase in the mainstream flow Reynolds number and were found to be in good agreement with the flat plate heat transfer analogy.

The effect of slot injection angle on the leading-edge horseshoe vortex and endwall heat transfer distribution was investigated by Thrift and Thole [91] in a large-scale low-speed cascade. At low blowing ratios, the turbulence levels were noted to be very similar to the no injection case. The low momentum coolant was observed to be dominated by the secondary flow at the airfoil-endwall junction resulting in the formation of a leading-edge

horseshoe vortex for all the slot injection cases. It was found that at high blowing ratios, the leading-edge horseshoe vortex disappeared for the 30° and 45° slot injection and increased turbulence levels were observed that resulted in the enhancement of endwall heat transfer compared to the no injection case. In the case of 65° and 90° slot injection, a significant downwash was observed near the airfoil leading-edge which resulted in the boundary layer impingement on the endwall thereby augmenting the heat transfer at high blowing ratios.

References

[1] Goldstein, R. J., 1971, "Film-cooling", *Adv. Heat Transfer*, Vol. 7, pp. 321-379.

[2] Bogard, D.G., and Thole, K.A., 2006, "Gas turbine film cooling", *Journal of Propulsion and Power*, Vol. 22, pp. 249–270.

[3] Bunker, R. S., 2005, "A review of shaped hole turbine film-cooling technology", *Journal of Heat Transfer*, Vol. 127, pp. 441-453.

[4] Eriksen, V.L., and Goldstein, R.J., 1974, "Heat transfer and Film cooling following injection through inclined circular tubes," *Journal of Heat Transfer*, Vol. 96, pp. 239-245.

[5] Goldstein, R.J., Eckert, E.R.G., and Burggraf, F., 1974, "Effects of hole geometry and density on three-dimensional Film cooling," *International Journal of Heat and Mass Transfer*, Vol. 17, pp. 595-607.

[6] R.J. Goldstein, and T. Yoshida, 1982, "The influence of a laminar boundary layer and laminar injection on film cooling performance", *Journal of Heat Transfer*, Vol. 104, pp. 355–362

[7] Sinha, A. K., Bogard, D. G., and Crawford, M. E., 1991, “Film-Cooling Effectiveness Downstream of a Single Row of Holes with Variable Density Ratio”, *Journal of Turbomachinery,* Vol. 113, pp. 442-449.

[8] Bell, C. M., Hamakawa, H., and Ligrani, P. M., 2000, “Film Cooling from Shaped Holes,” *Journal of Heat Transfer,* Vol. 122, pp. 224-232.

[9] Hay, N., Lampard, D., and Saluja, C.L., 1985, “Effects of cooling Films on the heat transfer coefficient on a flat plate with zero mainstream pressure gradient,” *Journal of Engineering for Gas Turbines and Power*, Vol. 107, pp. 104-110.

[10] Liess, C., 1975, “Experimental investigation of film cooling with ejection from a row of holes for the application to gas turbine blades”, *Journal of Engineering for Power*, Vol. 97, pp. 21-27.

[11] Pedersen, D., Eckert, E., and Goldstein, R., 1977, "Film Cooling with Large Density Differences between the Mainstream and the Secondary Fluid Measured by the Heat-Mass Transfer Analogy," *Journal of Heat Transfer*, Vol. 99, pp. 620-627.

[12] Lutum, E., and Johnson, B. V., 1998, “Influence of Hole Length-to-Diameter Ratio on Film Cooling with Cylindrical Holes”, *Journal of Turbomachinery*, Vol. 121, pp. 209-216.

[13] Gritsch, M., Schulz, A., and Wittig, S., 2000, “Film-Cooling Holes with Expanded Exits: near-hole heat transfer coefficients," *International Journal of Heat and Fluid Flow*, Vol. 21, pp. 146-155.

[14] Goldstein, R.J., and Taylor, J.R., 1982, “Mass transfer in the neighborhood of jets entering a crossflow,” *Journal of Heat Transfer*, Vol. 104, pp. 715-721.

[15] Ammari, H.D., Hay, N., and Lampard, D., 1990, “The effect of density ratio on the heat transfer coefficient from a film-cooled flat plate,” *Journal of Turbomachinery*, Vol. 112, pp. 444-450.

[16] Pietrzyk, J. R., Bogard, D. G., and Crawford, M. E., 1990, “Effects of Density Ratio on the Hydrodynamics of Film Cooling”, *Journal of Turbomachinery,* Vol. 112, pp. 437-443.

[17] Nasir, H., Ekkad, S. V., and Acharya, S., 2001, “Effect of Compound Angle Injection on Flat Surface Film Cooling with Large Streamwise Injection Angle,” *Journal of Experimental Thermal and Fluid Science*, Vol. 25, pp. 23-29.

[18] Yuen, C. H. N., and Martinez Botas, R. F., 2003, “Film cooling characteristics of a single round hole at various angles in a cross flow: Part I-effectiveness,” International Journal of Heat and Mass Transfer, Vol. 46, pp. 221-235.

[19] Yuen, C. H. N., and Martinez-Botas, R. F., 2003, “Film cooling characteristics of a single round hole at various angle in a cross flow: Part II-heat transfer coefficients,” *International Journal of Heat and Mass Transfer*, Vol. 46, pp. 237-249.

[20] Walters, D. K., and Leylek, J. H., 2000, “A detailed analysis of film cooling physics: Part I—streamwise injection with cylindrical holes,” Journal of Turbomachinery, Vol. 122, pp. 102–112.

[21] Ligrani, P.M. and Williams, W. 1988, "Effects of an Embedded Vortex on Injectant from a Single Film-Cooling Hole in a Turbulent Boundary Layer," Journal of Turbomachinery, Vol. 112, pp. 428-436.

[22] Ligrani, P.M., Ortiz, A., Joseph, S.L., and Evans, D.L., 1988, "Effects of Embedded Vortices on Film-Cooled Turbulent Boundary Layers," Journal of Turbomachinery, Vol. 111, pp. 71-77.

[23] Womack, K. M., Volino, R. J., and Schultz, M. P., 2008, "Combined Effects of Wakes and Jet Pulsing on Film Cooling", Journal of Turbomachinery, Vol. 130, pp. 041010- 1-12.

[24] Womack, K. M., Volino, R. J., and Schultz, M. P., 2008, "Measurements in Film Cooling Flows with Periodic Wakes", Journal of Turbomachinery, Vol. 130, pp. 041008- 1-13.

[25] Schobeiri, M., Read, K., and Lewalle, J., 2003, "Effect of Unsteady Wake Passing Frequency on Boundary Layer Transition, Experimental Investigation, and Wavelet Analysis," Journal of Fluids Engineering, Vol. 125, pp. 251-266

[26] Du, H., Han, J. C., and Ekkad, S. V., 1998, "Effect of Unsteady Wake on Detailed Heat Transfer Coefficient and Film Effectiveness Distributions for a Gas Turbine Blade," Journal of Turbomachinery, Vol. 120, pp. 808-817.

[27] Du, H., Ekkad, S. V., and Han, J. C., 1999, "Effect of Unsteady Wake With Trailing Edge Ejection on Film Cooling Performance for a Gas Turbine Blade," Journal of Turbomachinery, Vol. 121, pp. 448–455.

[28] Han, J. C., Zhang, L., and Ou, S., 1993, "Influence of Unsteady Wake on Heat Transfer Coefficient from a Gas Turbine Blade," Journal of Heat Transfer, Vol. 115, pp. 904–911.

[29] Adami, P., Montomoli, F., and Belardini, E., 2004, "Interaction Between Wake and Film Cooling Jets: Numerical Analysis," ASME Turbo Expo, Paper No. GT2004-53178, pp 1053-1063.

[30] Dullenkopf, K., Shulz, A., and Wittig, S., 1991, "The Effect of Incident Wake Conditions on the Mean Heat Transfer of an Airfoil", Journal of Turbomachinery, Vol. 113, pp. 412-418.

[31] Teng, S., Sohn, D. K., and Han, J. C., 2000, "Unsteady Wake Effect on Film Temperature and Effectiveness Distributions for a Gas Turbine Blade," Journal of Turbomachinery, Vol. 122, pp. 340-347.

[32] Funazaki, K., Yokota, M., Yamawaki, S., 1997, "Effect of Periodic Wake Passing on Film Effectiveness of Discrete Cooling Holes Around the Leading-edge of a Blunt Body", Journal of Turbomachinery, Vol. 119, pp. 292-301.

[33] Rodríguez, S., Kersten, S., Krishnan, V., and Kapat, J. S., 2008, "Effect of Wake on Endwall Film Cooling Effectiveness for a Row of Cylindrical Holes Near the Stagnation Region of an Airfoil", Proceedings of the ASME Turbo Expo, GT2008-51460.

[34] Heidmann, J. D., Lucci, B. L., and Reshotko, E., 2001, "An Experimental Study of the Effect of Wake Passing on Turbine Blade Film Cooling," Journal of Turbomachinery, Vol. 123, pp. 214-221.

[35] Ou, S., Han, J. C., Mehendale, A. B., and Lee, C. P., 1994, "Unsteady Wake over a Linear Turbine Blade Cascade with Air and CO_2 Film Injection: Part I-Effect on Heat Transfer Coefficients", Journal of Turbomachinery, Vol. 116, pp. 721-729.

[36] Mehendale, A. B., Han, J. C., Ou, S., and Lee, C. P., 1994, "Unsteady Wake over a Linear Turbine Blade Cascade with Air and CO_2 Film Injection: Part II-Effect on Film Effectiveness and Heat Transfer Distributions", Journal of Turbomachinery, Vol. 116, pp. 730-737.

[37] Wright, L., Blake, S., Rhee, D. H., and Han, J. C., 2009, "Effect of Upstream Vortex on Turbine Blade Platform Film Cooling With Simulated Stator-Rotor Purge Flow", Journal of Turbomachinery, Vol. 131, pp. 021017.1-021017.1

[38] W.R. Hawthorne, 1951, "Secondary circulation in fluid flow", *Proceedings A-Royal Society Publishing*, Vol. 206.

[39] Sieverding, C. H., 1985, "Recent progress in the understanding of basic aspects of secondary flows in turbine blade passages", *Journal of Engineering for Gas Turbines and Power*, Vol. 107, pp. 248-257.

[40] Moore, J., and Smith, B. L., 1984, "Flow in a turbine cascade: part 2 - measurement of flow trajectories by ethylene detection", *Journal of Engineering for Gas Turbines and Power*, Vol. 106, pp. 409-413.

[41] Sieverding, C. H., and Van den Bosch, P., 1983, "The use of colored smoke to visualize secondary flows in a turbine-blade cascade", *Journal of Fluid Mechanics*, Vol. 134, pp. 85-89.

[42] Langston, L., Nice, M., and Hooper, R., 1977, "Three-dimensional flow within a turbine cascade passage", *Journal of Engineering for Power*, pp. 21-28.

[43] Sjolander, S. A., 1975, "The endwall boundary layer in an annular cascade to turbine nozzle guide vanes", *Carleton University Press*, Ottawa, Canada.

[44] Harrison, S., 1989, "Secondary loss generation in a linear cascade of high-turning turbine blades", *Proceedings of the International Gas Turbine and Aeroengine Congress and Exposition*, 89-GT-47, pp. 1-7.

[45] Gregory-Smith, D. G., Graves, C., and Walsh, J., 1988, "Growth of secondary losses and vorticity in an axial turbine cascade", *Journal of Turbomachinery*, Vol. 110, pp. 1-8.

[46] Marchal, P., and Sieverding, C. H., 1977, "Secondary flows within turbomachinery bladings", *Proceedings of the Advisory Group for Aerospace Research and Development*, Vol. 214.

[47] Denton, J. D., 1993, "Loss mechanisms in turbomachines", *Journal of Turbomachinery*, Vol. 115, pp. 621-656.

[48] Mahmood, G., and Acharya, S., 2014, "Effects of blade leading-edge fillet on near wall pressure and heat transfer in a linear turbine cascade", *Proceedings of the International Mechanical Engineering Congress and Exposition*, IMECE2014-39768.

[49] Praisner, T. J., Bradley, A. R., Grover, E. A., Knezevici, D. C., Sjolander, S. A., 2013, "Application of non-axisymmetric endwall contouring to conventional and high-lift turbine airfoils", *Journal of Turbomachinery*, Vol. 135, pp. 1-8.

[50] Abraham, S., Panchal, K., Ekkad, S. V., Ng, W., Lohaus, A. S., and Malandra, A., 2012, "Measurement of aerodynamic losses for turbine airfoil cascades with varying pitch, operating under transonic conditions", *Proceedings of the ASME Turbo Expo*, GT2012-68424.

[51] Biesinger, T.E. and Gregory-Smith, D.G., 1993, "Reduction in secondary flows and losses in a turbine cascade by upstream boundary layer blowing", *Rolls Royce PLC-Report*, Vol. 91084, pp. 1-16.

[52] Sieverding, C. H., and Wilputte, P., 1981, "Influence of mach number and endwall cooling on secondary flows in a straight nozzle cascade", *Journal of Engineering for Power*, Vol. 103, pp. 257–263.

[53] Goldman, L. J. and McLallin, K. L., 1977, "Effect of end wall cooling on secondary flows in turbine stator vanes", *Proceedings of the Advisory Group for Aerospace Research and Development*, Vol. 214.

[54] Blair, M. F., 1974, "Experimental study of heat transfer and film cooling on large-scale turbine endwalls", *Journal of Heat Transfer*, Vol. 96, pp. 524-529.

[55] Takeishi, K., Matsuura, M., Aoki, S., 1990, "Experimental study of heat transfer and film cooling on low aspect ratio turbine nozzles", *Journal of Turbomachinery*, Vol. 112, pp. 488-496.

[56] Harasgama, S. P., and Burton, C. D., 1992, "Film cooling research on the endwall of a turbine nozzle guide vane in a short duration annular cascade: part I-experimental technique and results", *Journal of Turbomachinery*, Vol. 114, pp. 734-740.

[57] Harasgama, S. P., and Burton, C. D., 1992, "Film cooling research on the endwall of a turbine nozzle guide vane in a short duration annular cascade: part II-analysis and correlation of results", *Journal of Turbomachinery*, Vol. 114, pp. 741-746.

[58] Lakshminarayana, B., 1975, "Effects of inlet temperature gradients on turbomachinery performance", *Journal of Engineering for Power*, Vol. 97, pp. 64-74.

[59] Friedrichs, S., Hodson, H.P., and Dawes, W.N., 1996, "Distribution of film-cooling effectiveness on a turbine endwall measured using the ammonia and diazo technique", *Journal of Turbomachinery*, Vol. 118, pp. 613–621.

[60] Friedrichs, S., Hodson, H.P., and Dawes, W.N., 1997, "Aerodynamic aspects of endwall film-cooling", *Journal of Turbomachinery*, Vol. 119, pp. 786-793.

[61] Friedrichs, S., Hodson, H. P., and Dawes, W. N., 1999, "The design of an improved endwall film-cooling configuration", *Journal of Turbomachinery*, Vol. 121, pp. 772-780.

[62] Barigozzi, G., Fontaneto, F., and Franchini, G., 2012, "Influence of coolant flow rate on aero-thermal performance of a rotor blade cascade with endwall film cooling", *Journal of Turbomachinery*, Vol. 134, pp. 1-8.

[63] Liu, G., Liu, S., Zhu, H., Lapworth, B. L., and Forest, A, E., 2004, "Endwall heat transfer and film-cooling measurements in a turbine cascade with injection upstream of leading-edge", *Heat Transfer–Asian Research*, Vol. 33, pp. 141-154.

[64] Jabbari, M. Y., Marston, K. C., Eckert, E. R. G., and Goldstein, R. J., 1996, "Film cooling of the gas turbine endwall by discrete-hole injection", *Journal of Turbomachinery*, Vol. 118, pp. 278–284.

[65] Goldstein, R. J., and Chen, P. H., 1987, "Film cooling of a turbine blade with injection through two rows of holes in the near-endwall region", *Journal of Turbomachinery*, Vol. 109, pp. 588-593.

[66] Friedrichs, S., 1997, "Endwall film-cooling in axial flow turbines", *Ph.D. Dissertation*, Cambridge University, Cambridge, United Kingdom.

[67] Hada, S., and Thole, K. A., 2011, “Computational study of a midpassage gap and upstream slot on vane endwall film-cooling”, *Journal of Turbomachinery*, Vol. 133, pp. 011024-1 – 011024-9.

[68] Hermanson, K., and Thole, K.A., 2002, “Effect on non-uniform inlet conditions on endwall secondary flows”, *Journal of Turbomachinery*, Vol. 124, pp. 623-631.

[69] Lynch, S. P., Thole, K. A., Kohli, A., and Lehane, C., 2011, “Computational predictions of heat transfer and film-cooling for a turbine blade with non-axisymmetric endwall contouring”, *Journal of Turbomachinery*, Vol. 133, pp. 041003-1 – 041003-10.

[70] Knost, D. G., and Thole, K. A., 2003, “Computational predictions of endwall film-cooling for a first stage vane”, *Proceedings of the ASME Turbo Expo*, GT2003-38252.

[71] Colban, W., Thole, K. A., and Haendler, M., 2006, "A comparison of cylindrical and fan-shaped film-cooling holes on a vane endwall at low and high freestream turbulence levels," 2006 ASME 51st Turbo Expo, May 6, 2006 - May 11, American Society of Mechanical Engineers, Barcelona, Spain, 3 PART A, pp. 25-35.

[72] Barigozzi, G., Franchini, G., Perdichizzi, A., 2007, "End-Wall Film Cooling Through Fan-Shaped Holes With Different Area Ratios," Journal of Turbomachinery, **129**pp. 212.

[73] Kunze, M., Vogeler, K., Brown, G., Prakash, C., Landis, K., 2011, "Aerodynamic and Endwall Film Cooling Investigations of a Gas Turbine Nozzle Guide Vane Applying Temperature-Sensitive Paint," Journal of Turbomachinery, **133**pp. 031027.

[74] Thole, K. A., and Sundaram, N., 2009, "Film-Cooling Flowfields with Trenched Holes on an Endwall," Journal of Turbomachinery, 131(4) pp. 041007 (10 pp.).

[75] Zhang, L. J., and Jaiswal, R. S., 2001, "Turbine nozzle endwall film cooling study using pressure-sensitive paint", *Journal of Turbomachinery*, Vol. 123, pp. 730-738.

[76] Knost, D.G. and Thole, K.A., 2005, "Adiabatic effectiveness measurements of endwall film-cooling for a first stage vane", *Journal of Turbomachinery*, Vol. 127, pp. 297-305.

[77] Wright, L. M., Gao, Z., Yang, H., and Han, J. C., 2008, "Film cooling effectiveness distribution on a gas turbine blade platform with inclined slot leakage and discrete film hole flows", *Journal of Heat Transfer*, Vol. 130, pp. 071702-1 - 071702-11.

[78] Nicklas, M., 2001, "Film-cooled turbine endwall in a transonic flow field: part II–heat transfer and film-cooling effectiveness measurements", *Journal of Turbomachinery*, Vol. 123, pp. 720-729.

[79] Milidonis, K. F., and Georgiou, D. P., 2015, "Film cooling effectiveness in the region of the blade-endwall corner junction with the injection assisted by the recirculating vortex flow", *International Journal of Heat and Mass Transfer*, Vol. 83, pp. 294-306.

[80] Mensch, A., and Thole, K. A., 2014, "Overall effectiveness of a blade endwall with jet impingement and film cooling", *Journal of Engineering for Gas Turbines and Power*, Vol. 136, pp. 031901-1 – 031901-10.

[81] Gritsch, M., Schulz, A., and Wittig, S., 2001, "Effect of crossflows on the discharge coefficient of film cooling holes with varying angles of inclination and orientation", *Proceedings of the International Gas Turbine and Aeroengine Congress and Exposition*, 2001-GT-134, pp. 1-9.

[82] Rowbury, D. A., Oldfield, M. L. G., Lock, G. D., and Dancer, S. N., 1998, “Scaling of film cooling discharge coefficient measurements to engine conditions”, *Proceedings of the International Gas Turbine and Aeroengine Congress and Exposition*, 98-GT-79, pp. 1-8.

[83] Thole, K. A., and Knost, D. G., 2005, "Heat Transfer and Film-Cooling for the Endwall of a First Stage Turbine Vane," International Journal of Heat and Mass Transfer, 48(25-26) pp. 5255-69.

[84] M. Kang, A. Kohli, K.A. Thole, 1999, Heat transfer and flowfield measurements in the leading-edge region of stator vane endwall, J. Turbomachinery 121 (3) (1999) 558–568.

[85] Spencer, M. C., Jones, T. V., and Lock, G. D., 1996, “Endwall heat transfer measurements in an annular cascade of nozzle guide vanes at engine representative Reynolds and Mach numbers,” *International Journal of Heat and Fluid Flow*, Vol. 17, pp. 139-147.

[86] Boyle, R. J., and Russell, L.M., 1989, “Experimental Determination of Stator Endwall Heat Transfer”, NASA Technical Memorandum 101419.

[87] Graziani, R.A., Blair, M.F., Taylor, J.R. and Mayle, R.E., 1980, “An Experimental Study of Endwall and Airfoil Surface Heat Transfer in a Large Scale Turbine Blade Cascade”, ASME Journal of Engineering for Power, Vol. 102, pp. 257-267

[88] Goldstein, R. J., and Spores, R.A., 1988, “Turbulent transport on the endwall in the region between adjacent turbine blades”, *Journal of Heat Transfer*, Vol. 110, pp. 862-869.

[89] Harvey, N.W., Wang, Z., Ireland, P.T. and Jones, T.V., 1989, "Detailed Heat Transfer Measurements in Nozzle Guide Vane Passages in Linear and Annular Cascades in the Presence of Secondary Flows", AGARD CPP-468/469, pp. 24/1 - 24/12

[90] Chana, K.S., 1993, "Heat Transfer and Aerodynamics of a 3D Design Nozzle Guide Vane Tested in the Pyestock Isentropic Light Piston Facility", AGARD-CP-527, Heat Transfer and Cooling in Gas Turbines, pp. 1/1 - 1/11.

[91] Thrift, A. A. and Thole, K. A., 2012, "Influence of flow injection angle on a leading-edge horseshoe vortex", *International Journal of Heat and Mass Transfer*, Vol. 55, pp. 4651-4664.

CHAPTER 3: RESEARCH OBJECTIVES

Scientific Contributions

The main scientific contributions of the present dissertation work are as follows:

Unsteady Passing Wake Effect on a Pitchwise-curved Surface

(i) To quantify the impact of unsteady passing wakes on heat transfer on a film-cooled pitchwise-curved surface, replicating an endwall without airfoils.

(ii) To bridge the knowledge gap between flat plate film cooling and cascade film cooling studies in the regime of unsteady passing wake effect.

Endwall Film Cooling in a High Subsonic Annular Cascade

(i) To provide a fundamental insight into the interaction between the endwall secondary flow and the coolant jets from a surface flow perspective and extending this information to the predicted three-dimensional flow field.

(ii) To quantify the impact of endwall secondary flow on film cooling and vice versa.

(iii) The procedure reported in this investigation to understand the endwall secondary flow and film cooling jet interaction can be adapted towards improvement in an engine endwall film cooling hole configuration.

The pertinent scientific contributions from the present dissertation study are detailed in Table 1.

Table 1: Scientific contributions

Current Issue	**Contribution(s) of present study**	**Instrumentation/ Methodology**	**Key aspects of experimental setup**
Endwall film cooling affected by unsteady passing wakes shed by upstream components	❖ Quantification of the effect of passing wakes on heat transfer on a film-cooled pitchwise curved surface, replicating an endwall in the absence of airfoils	❖ Foil heater ❖ Temperature sensitive paint ❖ Hot wire ❖ Pitot-static tube ❖ Static pressure taps	❖ Sector-annular duct with wall-normal wake rod orientation ❖ Baseline test case – no film cooling ❖ Single row discrete film injection ❖ Cylindrical film cooling hole ❖ $\alpha = 35^{\circ}$, $\beta = 0^{\circ}$ p/d $\cong$ 3, Number of holes = 5 ❖ Wake rod to film cooling hole diameter ratio = 2.375 ❖ DR $\cong$ 1
Impact of secondary flow on endwall film cooling effectiveness	❖ Study of interaction between discrete film cooling jets and secondary flow ❖ Quantification of saddle point shift with film injection ❖ Quantification of local blowing ratio effect on film effectiveness ❖ Quantification of local discharge coefficient effect on film effectiveness	❖ Surface oil visualization ❖ Temperature sensitive paint ❖ Pressure sensitive paint ❖ Pitot-static tube ❖ Five-hole probe ❖ Hot wire ❖ Static pressure taps ❖ CFD	❖ High subsonic annular cascade with a maximum isentropic throat Mach number of $\cong$ 0.68 ❖ Baseline test case – no film cooling ❖ Single row discrete film injection upstream of airfoil leading-edge; ❖ Cylindrical film cooling hole ❖ $\alpha = 30^{\circ}$, $\beta = 0^{\circ}$ p/d $\cong$ 3.55 ❖ Airfoil leading-edge diameter to film cooling hole diameter ratio ($\cong$ 4.75) representative of an aircraft engine ❖ DR $\cong$ 0.89

CHAPTER 4: INSTRUMENTATION AND METHODOLOGY

This chapter contains a detailed description of the various types of measurements and instrumentation involved in this research study.

Temperature Sensitive Paint

In order to obtain local temperature measurements on the test surface, the Temperature Sensitive Paint (TSP) technique was used. This provides high resolution measurements of temperature on the test surface based on the maximum number of pixels available on the imaging device. The test surface (airfoil passage-3 inner endwall) was painted with TSP that comprises luminescent molecules (pigment) in an oxygen-impermeable polymer binder. A schematic of the TSP technique is shown in Figure 11. The photo-physical process of thermal quenching, which is the principle of the TSP technique is explained using the Jablonski quantum energy-level diagram as shown in Figure 12.

The luminescent molecule is initially at the ground state which is a singlet state. The recommended excitation range for TSP is between 380 and 520 nm. When the TSP is exposed to a peak excitation wavelength of 458.2 nm with a full width at half maximum of 30.7 nm, the ground state molecules absorb the incident photons and get transferred to an excited state. The molecule returns to its original energy state through emission of a longer wavelength (lower energy) light relative to the excitation wavelength. The probability that the molecule will emit luminescent light as opposed to the radiation-less transition to ground state through thermal quenching decreases at higher temperature. Thus the intensity

of TSP is inversely proportional to temperature of the luminophore. The intensity of the emitted radiation is detected by a scientific grade CCD (charge-coupled device) camera (14-bit PCO 1600 monochrome) using a long pass filter with a typical high pass cut-off wavelength of 550 nm. Due to the oxygen impermeability of the polymer binder, the TSP measurements are not influenced by oxygen partial pressure changes. Hence oxygen quenching does not affect the temperature measurements obtained from the TSP technique. The effect of the test surface curvature on the pixel shift in the image was found to be less than 1 pixel at the CCD camera position. This shift was therefore neglected during the processing of the TSP images. More details on the TSP technique can be found in Liu [1]. Using an in-house MATLAB code, the time-averaged temperatures are processed to calculate the adiabatic film cooling effectiveness (see chapter 6 for equation).

The spatial variations due to the illumination and the paint thickness are eliminated by taking the ratio of a reference (wind-off) and a test (wind-on) image. A spatial resolution of ≅ 7.3 pixels per 'mm' was obtained for the captured image size (1200 × 1600 pixels). The signal to noise ratio was calculated for each average blowing ratio. An average signal to noise ratio is reported here. The highest and lowest signal to noise ratio were calculated to be 100:1 and 54:1 respectively. The CCD camera noise obtained from the dark room image was subtracted from both the test image and the reference image during post processing.

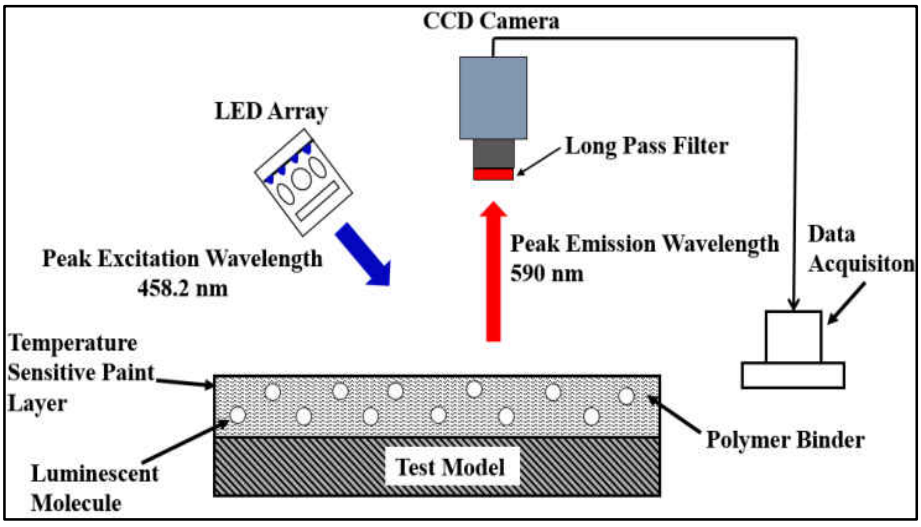

Figure 11: Temperature sensitive paint technique

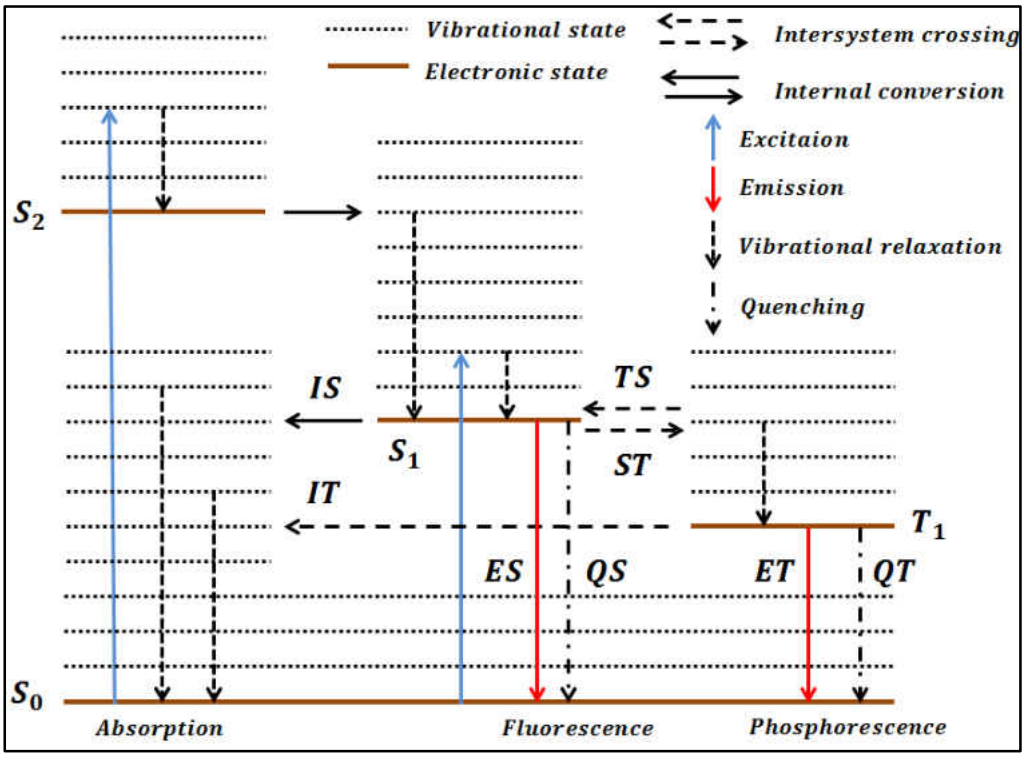

Figure 12: Jablonski quantum energy-level diagram [1]

Calibration

The calibration setup for the TSP is shown in Figure 13. During the calibration, a high thermal conductivity substrate (coupon) painted with TSP is placed on a Peltier thermo-electric module which in turn is placed on an aluminum heat sink. As part of the imaging procedure, the first image is taken at a known temperature, called the reference image (usually at room temperature). The second image called the hot image is taken at an elevated temperature (higher than reference temperature). This is repeated to span the entire calibration range at appropriate temperature increments (≅ 22 – 80°C).

By taking the ratio of TSP images at various temperatures to the reference image, a calibration curve with intensity ratio on the abscissa and temperature ratio on the ordinate is obtained. The definitions for the temperature and the intensity ratio are provided in Figure 14. It should be noted that T_{ref} and I_{ref} are the temperature and intensity of the calibration sample at zero heater voltage (i.e. approximately at room temperature). The values of T_{sample} and I_{sample} are taken at every calibration point. Therefore, at any known reference temperature and intensity ratio, the local surface temperature can be ascertained.

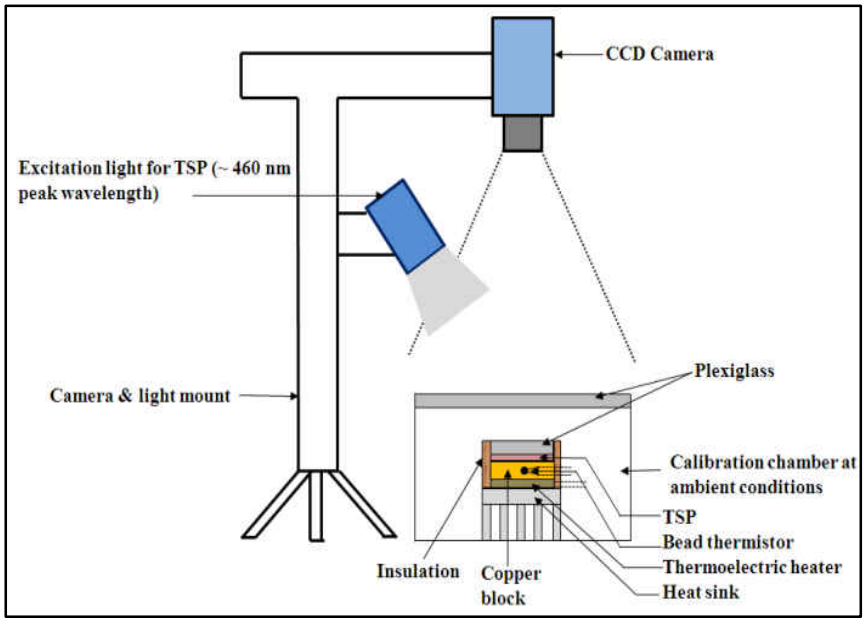

Figure 13: Temperature sensitive paint calibration setup

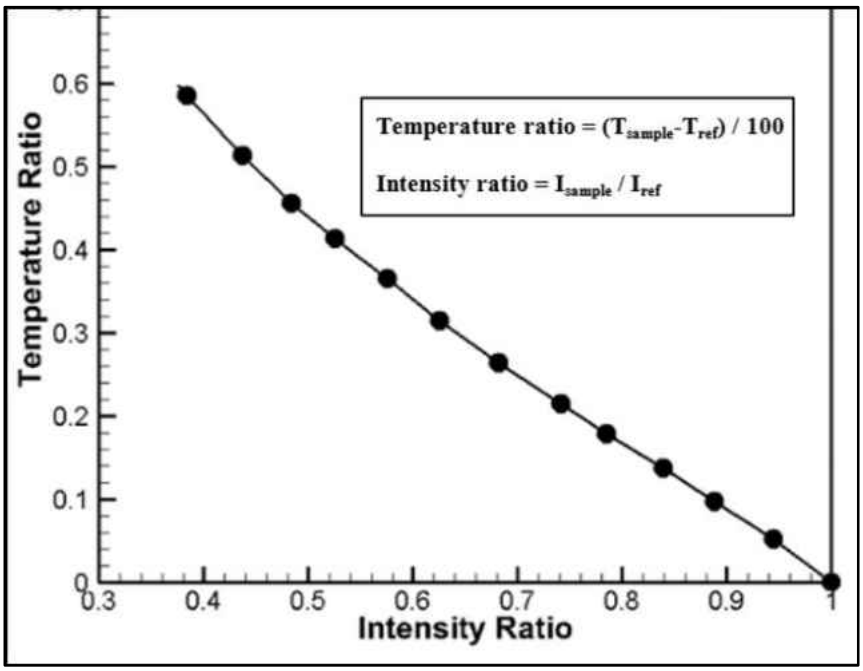

Figure 14: Temperature sensitive paint typical calibration curve

Pressure Sensitive Paint

The static pressure on the endwall is measured using the Pressure Sensitive Paint (PSP) technique. As part of the measurement process, the test surface (airfoil passage-3 inner endwall) is painted with PSP which comprises luminescent molecules (pigment) in an oxygen-permeable polymer binder which is sensitive to both pressure and temperature. The principle of the PSP method is the photo-physical process of oxygen quenching. The recommended excitation range for PSP is between 380 and 520 nm. A circular LED array with a peak excitation wavelength of 458.2 nm and a full width at half maximum of 30.7 nm is used to excite the luminescent molecules in the PSP. The excited luminophore returns to its original energy state by transferring the excited state energy to a vibrational mode of the local oxygen molecule through a process known as oxygen quenching. This is a radiation-less decay mechanism and the probability of this process increases at higher partial pressures of oxygen. The emission wavelength is higher relative to the excitation wavelength. Thus the intensity of PSP is inversely proportional to the oxygen partial pressure. Using a long pass filter with a typical high pass cut-off wavelength of 610 nm, the emitted radiation is captured by a scientific grade CCD camera (14-bit PCO 1600 monochrome) having a frame rate of 30 frames per second at its maximum resolution. The camera exposure time ranges between 300 ms and 600 ms. The spatial resolution of the measurements and elimination of PSP spatial variations were performed similar to TSP measurements (see Temperature Sensitive Paint). The highest and lowest signal to noise ratio were calculated to be 100:1 and 54:1 respectively. Figures 15,16,17 provide the

schematics of the PSP technique, calibration setup, and a typical calibration curve respectively. For a more detailed explanation of the PSP technique, refer Liu [1].

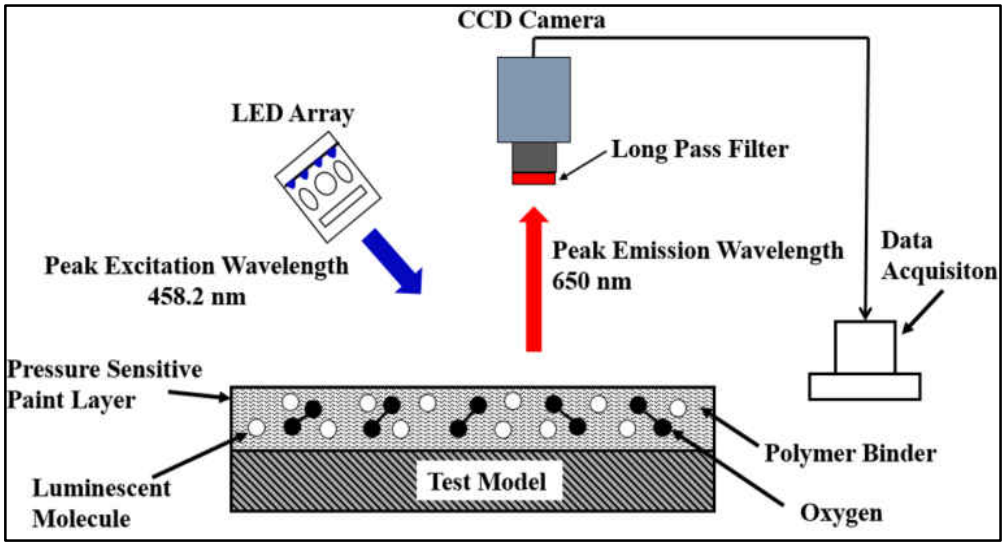

Figure 15: Pressure sensitive paint technique

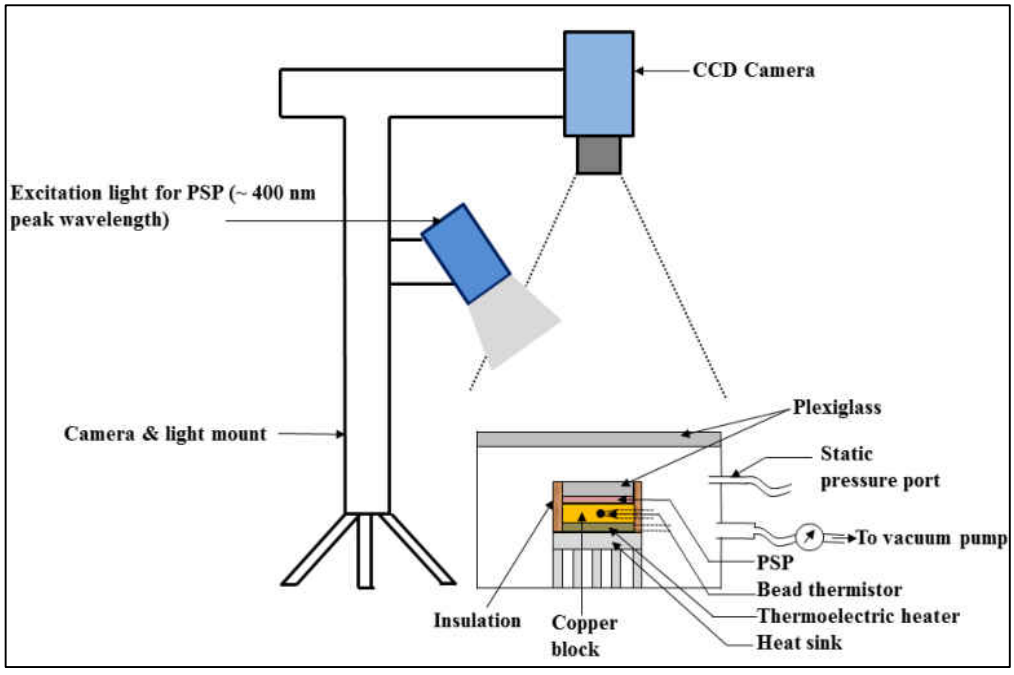

Figure 16: Pressure sensitive paint calibration setup

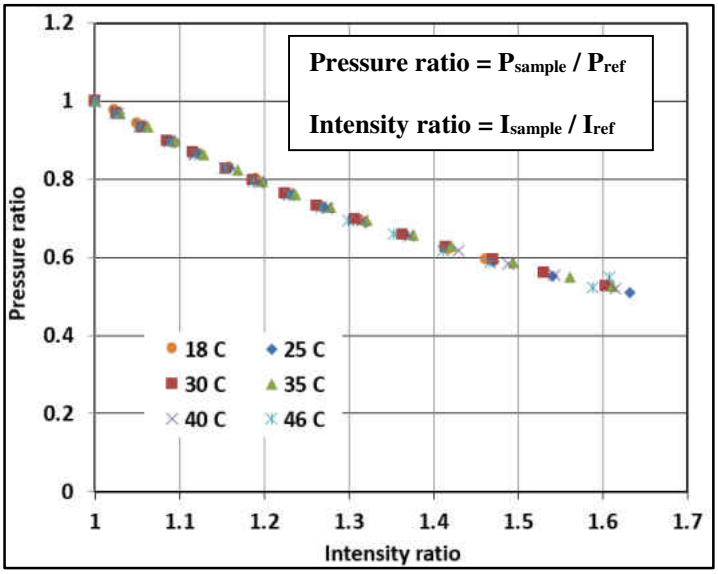

Figure 17: Pressure sensitive paint typical calibration curve

Calibration

As part of the PSP calibration process, a small coupon painted with PSP is placed inside a calibration chamber with a thermoelectric heater placed under it to keep the temperature approximately constant throughout the calibration. A reference image is taken at ambient conditions (reference pressure). A vacuum pump is used (since the cascade tunnel is operated under suction) to regulate the pressure inside the calibration chamber to the desired value. The pressure inside the calibration chamber is monitored using static pressure taps (mounted flush with the wall of the calibration chamber) connected via plastic tubing to a hand-held manometer. By taking the ratio of PSP images at various gauge pressures to the reference image, a calibration curve with intensity ratio on the abscissa and pressure ratio on the ordinate is obtained for a fixed temperature. Since PSP is temperature sensitive, the calibration is repeated at different temperatures. For the temperature range observed in the experiment, the PSP calibration curve exhibited negligible change between

temperatures. Using an in-house MATLAB code, the static pressure on the surface is obtained from the image intensity using calibration curve.

Five-hole Probe Measurements

Using multi-hole probes for total pressure measurements is mainly due to their ability to provide the correct flow information when the direction of the flow is not known beforehand. This type of measurement is called the non-nulling technique [2] in which the probe undergoes extensive calibration for different yaw and pitch angles of the flow. The nomenclature of the five-hole probe is shown in Figure 18 based on [2].

The five-hole probe has five pneumatic tubes which carry information of the flow dynamics. The center pressure port (P1) measures the stagnation pressure in the case of a mainstream flow parallel to the probe. There are four pressure ports (P2, P3, P4, P5) located on the periphery of the probe cone which measure the static or stagnation pressure depending on the orientation of the probe with respect to the incoming flow.

Construction

A necked five-hole probe was used which has a robust stainless steel construction. The drawing of the probe is shown in Figure 19. The probe tip has a cone with a half angle of 30°. Connecting all the five ports on the cone are pneumatic stainless steel tubing which is soldered to the ports and then fit into a larger tube enclosed within the probe shaft. The space between the pneumatic tubing and the probe shaft is filled with epoxy to avoid tubing

displacement. The end of the metal tubing is connected to flexible plastic tubing that in turn interfaces with the pressure transducer.

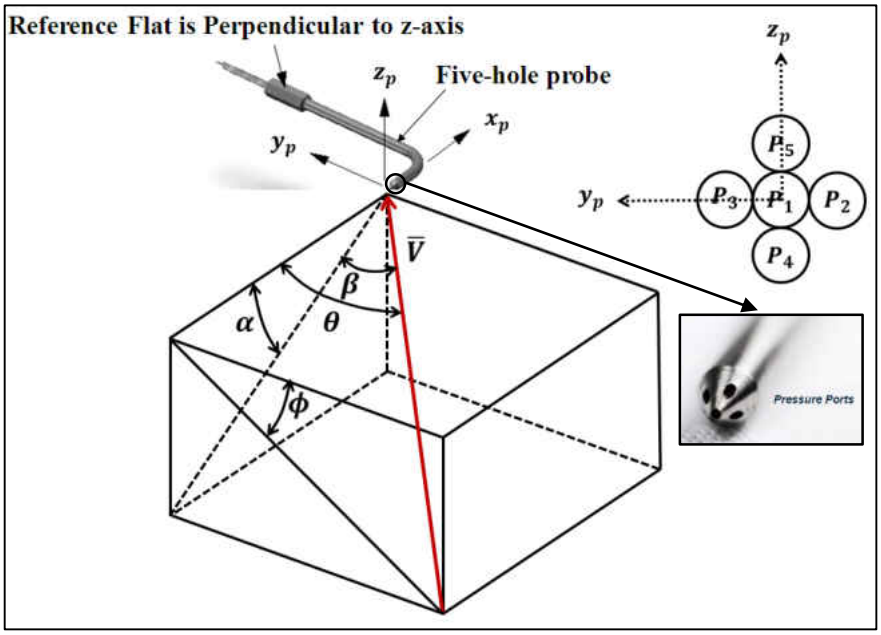

Figure 18: Five-hole probe nomenclature [2]

(All dimensions are in mm)

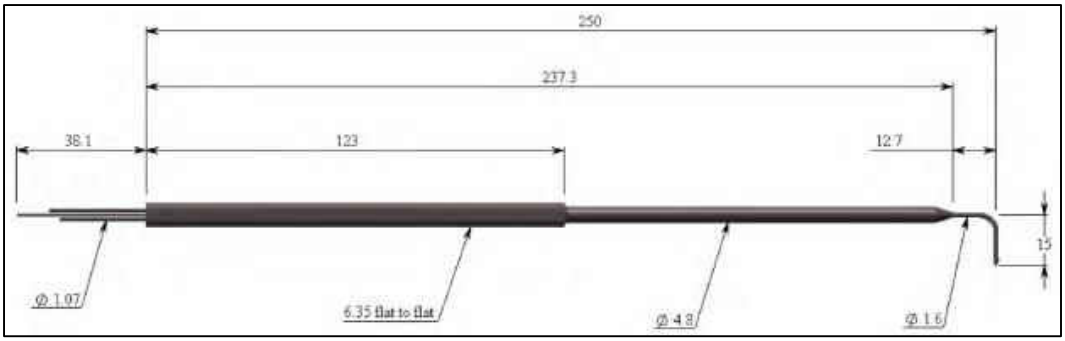

Figure 19: Dimensions of the five-hole probe [2]

Calibration

During calibration (performed by Aeroprobe Corp.), the probe is exposed to numerous yaw and pitch angles in the probe coordinate system. At each location, pressure data from all the five port pressures are recorded. The same procedure is repeated for different flow Mach numbers. A calibration chart is generated from the measurements which can be used to obtain the flow magnitude, direction and other flow quantities by interpolating between the five port pressures and using compressible flow equations. The five-hole probe in this study was calibrated for Mach numbers between 0.2 and 0.7 with ±60° yaw and pitch angle accuracy. It should be noted here that any deviation from the calibration range of the probe can lead to separated flow near the vicinity of the pressure ports, which will give incorrect flow information. Thus it is critical to stay within the calibrated range of the probe. A data-reduction software (Multi-probe) provided by Aeroprobe Corporation was used to reduce the pressure data from the five ports to meaningful flow quantities.

Measurements

The five-hole probe was used to measure the total pressure, static pressure, velocity components, pitch, yaw, and roll angle of the flow relative to the probe reference flat. These measurements were performed at few discrete locations at the cascade inlet plane. Before being introduced into the flow, the probe is inspected under a microscope to confirm that there are no foreign particles blocking the ports. High pressure air is blown through the pneumatic tubing to clear the tubing path. A manual traverse system that can locate the

probe in the flow circumferentially and radially with an accuracy of ±1.5 mm was used for the discrete point measurements. The primary purpose of the measurements were to ascertain the cascade inlet plane velocity, total, and static pressure before film cooling measurements were performed.

Hot-wire Measurements

In order to measure the streamwise instantaneous velocity and thereby the turbulence intensity in the flow field, a constant temperature thermal anemometer with a single hot film sensor was used. The film sensor is a disposable probe with a platinum film (TSI T1201) and can be used in the flow field up to a fluid maximum temperature of 60ºC. The film sensors are more rigid and less susceptible to get damaged by the foreign particles in the flow which was the reason behind the introducing the sensor in a high Mach number open circuit wind tunnel. On the other hand, the response time of the film sensors are lower than the wire sensors due to their low length to diameter ratio ($L/ D_W \cong 20$) [3].

Principle of Operation

The basic principle behind hot-wire anemometry is the measurement of fluid velocities by changes in heat transfer of a small electrically heated element that is exposed to the measuring medium. Inside the anemometer is a Wheatstone bridge that can operate in a constant temperature or constant current mode. The former used for the case of the hot wire measurements comprises a velocity and temperature compensation sensor in the lower leg of the bridge. The upper leg comprises two known resistances. An operational amplifier

controls the power delivered to the upper part of the bridge based on the change in resistance of the lower part such that the bridge remains balanced.

A schematic of a constant temperature anemometer circuit is shown in Figure 20. As the flow moves past the velocity sensor, the resistance of the sensor decreases which triggers the temperature compensation sensor to provide a feedback to the operational amplifier which supplies power to the upper half of the bridge network. The amount of power supplied to the upper half of the bridge is related to the fluid velocity in terms of voltage. By performing a calibration of voltage versus velocity, the flow speed is determined. The correlation for finding the velocity of the flow is provided in Equation 4.1. This correlation was reported by King [4].

$$\frac{R_w I^2}{R_w - R_a} = A + BU^n \tag{4.1}$$

where A, B, and n are calibration constants determined from the curve fit.

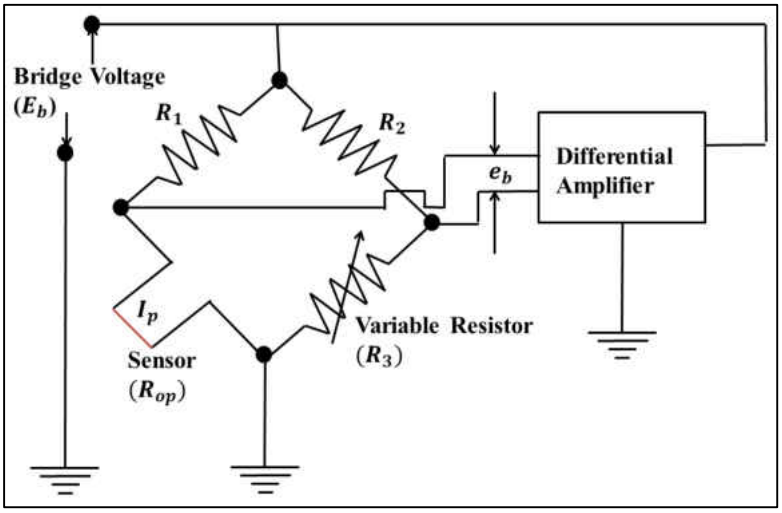

Figure 20: Circuit diagram of a constant temperature anemometer [3]

Calibration

A calibration nozzle (model 1125) provided by TSI Inc. [3] was used for calibrating the hot film sensor for the desired velocity range. The calibration nozzle contains three different nozzle diameter attachments to achieve a wide velocity range. For the present study, the smallest diameter nozzle (4mm) is used. Stagnation pressure is varied in the plenum corresponding to the required velocity at the nozzle exit. The hot film sensor (TSI T1201) is positioned approximately 2-3 mm away from the nozzle discharge location to reduce the disturbances caused by surrounding environment to the jet exiting the calibration nozzle. By monitoring the plenum pressure using a hand held manometer the output voltages are recorded using a voltmeter.

By graphing the voltage versus velocity and curve-fitting the data points, a relationship between the voltage and velocity is obtained in the calibrated velocity range. A Labview code with a National Instruments DAQ card is used for data acquisition. After calibration, the film sensor is positioned the exit of the nozzle and for a known pressure setting in the plenum, the nozzle exit velocity is measured. This validates the calibration curve for any discrepancy prior to data collection.

Pitot-static Tube Measurements

In order to ascertain the mass flow rate in the wind tunnel before every experiment, a Pitot-Static tube (United Sensor Corp.) was used. The total and static pressure ports were connected via flexible rubber tubing to a Fluke 922 air flow meter (Fluke Corp.) which outputs the velocity magnitude based on the measured differential pressure according to

the Bernoulli's equation (Equation 4.2). It is to be noted here that the Bernoulli's equation is valid for the calculation of velocity since the flow is incompressible at measurement location (Ma < 0.3). The fluid density is calculated based on the ideal gas law. The velocity measurements were made at the exit of nozzle – 1 (see chapter 8, Figure 43) at several discrete locations along the plane centerline in the spanwise direction.

$$u = \sqrt{\frac{2(P_0 - P_s)}{\frac{P_s}{RT_s}}} \tag{4.2}$$

Static Pressure Tap Measurements

In order to measure the airfoil passage periodicity, holes for static pressure taps were machined on the outer endwall of the cascade test section. The drilling of the holes were performed in two phases. As part of first phase, 1/32 inch (0.793 mm) through holes were drilled from the flow side on the outer endwall to ensure a smooth surface facing the mainstream flow. In the second phase, 1/16 inch (1.587 mm) holes were drilled from the non-flow side up to half the thickness on the outer endwall to enable insertion of the metal pressure tubing. This also ensures that the metal tubing does not accidentally protrude into the mainstream flow resulting in erroneous static pressure measurements.

Since the static pressure taps are required to be normal to the test surface, it was needed to position the drilling tool normal to the test surface. Due to the surface curvature of the outer endwall, the drilling of wall-normal holes were a challenge. A CNC drilling machine was used with a custom-design drill jig made to fit the curvature of the outer endwall. The drill jig is shown in Figure 21. The drill-head was indexed appropriately to ensure that the drilling tool was normal to the outer endwall before each drilling operation.

After drilling the holes, metal tubing (≅ 25.4 mm in length) was inserted into the hole and a small amount of two-part epoxy was applied around the metal tubing on the non-flow side of the outer endwall. Once the epoxy cured completely, clear flexible plastic tubing (purchased from Scannivalve Corp.) was cut to the desired length and attached to the open end of the metal tubing. A 47 port multiplexer along with a ± 5 psi (± 34,473 Pa) pressure transducer (purchased from Scannivalve Inc.) was used to obtain the static pressure measurements after appropriate port bias corrections. The outer endwall with the static pressure taps is shown in Figure 22.

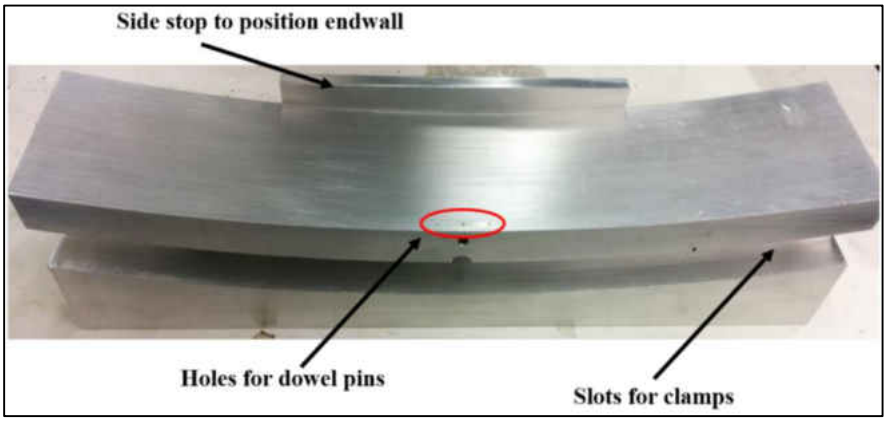

Figure 21: Drill jig for machining endwall static pressure tap holes

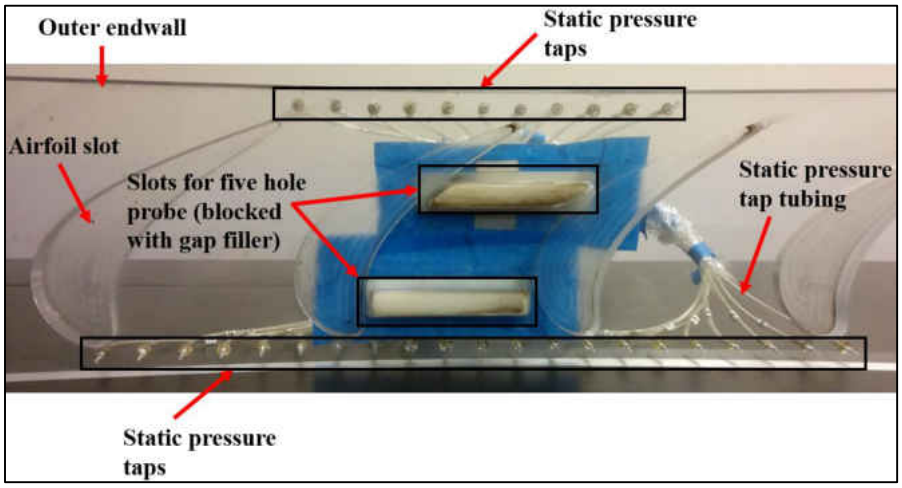

Figure 22: Outer endwall with static pressure taps and five-hole probe slots

Surface Oil Visualization

The endwall surface flow is visualized by applying a mixture of titanium dioxide powder and vacuum pump oil to the surface of interest. A few drops of oleic acid is added to reduce the viscosity of the mixture to help follow the endwall surface flow closely. Approximately 5-10 minutes after applying the mixture to the test surface, the wind tunnel is operated for a short duration (approximately 6-7 minutes). This time duration was based on several iterations since the endwall shear stress dictates the trajectory of the oil mixture which in turn is strongly dependent on the local flow velocity in the passage. After completion of the experiment, images of the surface flow pattern on the test surface are taken using a high resolution camera. In the cases with film injection, the coolant flow is turned on before activating the mainstream flow and the same imaging procedure is followed.

References

[1] Liu, Q., 2006, "Study of heat transfer characteristics of impinging air jet using pressure and temperature sensitive luminescent paint", *Ph.D. dissertation*, University of Central Florida, Orlando, USA.

[2] Aeroprobe Corp., 2008, "Five and Seven Probe Manual," Blacksburg, VA.

[3] TSI Corp., 2008, "Hot Wire Catalog," Shoreview, MN.

[4] King, L. V., 1914, "On the convection of heat from small cylinders in a stream of fluid: Determination of the convection constants of small platinum wires with applications to hot-wire anemometry", *Philosophical Transactions of the Royal Society,* A214, pp. 373-432.

CHAPTER 5: EXPERIMENTAL SETUP

Unsteady Passing Wake Effect on a Pitchwise-curved Surface

Mainstream Flow

All experiments were conducted in a low subsonic open-loop wind tunnel. The test section comprises a 30° annular duct made of acrylic supports and lexan polycarbonate walls for optical access. A 20 HP (14.91 kW) AC motor is used to power the blower. In order to isolate the effect of the airfoils, they are excluded from the test surface. A rotating spoke wheel is placed upstream of the test section to generate unsteady passing wakes. The spoke-wheel is driven by a 5 HP (3.73 kW) motor that is controlled by a variable frequency drive to allow control over the wake Strouhal number (see chapter 6 for equation). The spoke wheel was calibrated against a thermal anemometer for the appropriate wake passing frequency prior to the measurements. The test benefit of an annular channel is that the tangential velocity of rod is constant along the pitchwise coordinate of the test surface. This cannot be achieved in the more common rectangular test channels. The wake wheel has 12 rods with the ratio of rod to film hole diameter fixed at 2.375. This ratio was selected based on a parametric study performed by Golsen et al. [1] and a typical airfoil trailing edge to film cooling hole diameter ratio in an aircraft engine.

The average mainstream flow velocity (U_∞) was kept constant at ≅ 12 m/s for all the experiments. The mainstream flow was at room temperature (≅ 23°C). The mainstream velocity profile and turbulence intensity in the streamwise direction were measured in the absence of wakes using a TSI IFA 300 hot wire anemometer using a hot film probe (TSI 1201) at the film injection location. The measured value of the mainstream turbulence

intensity was ≅ 1.5%. The average fluid velocities were verified with Pitot-static tube measurements. The Reynolds number based on average mainstream velocity and the film hole diameter was ≅ 6.304×10^3. The experimental flow loop is shown in Figure 23.

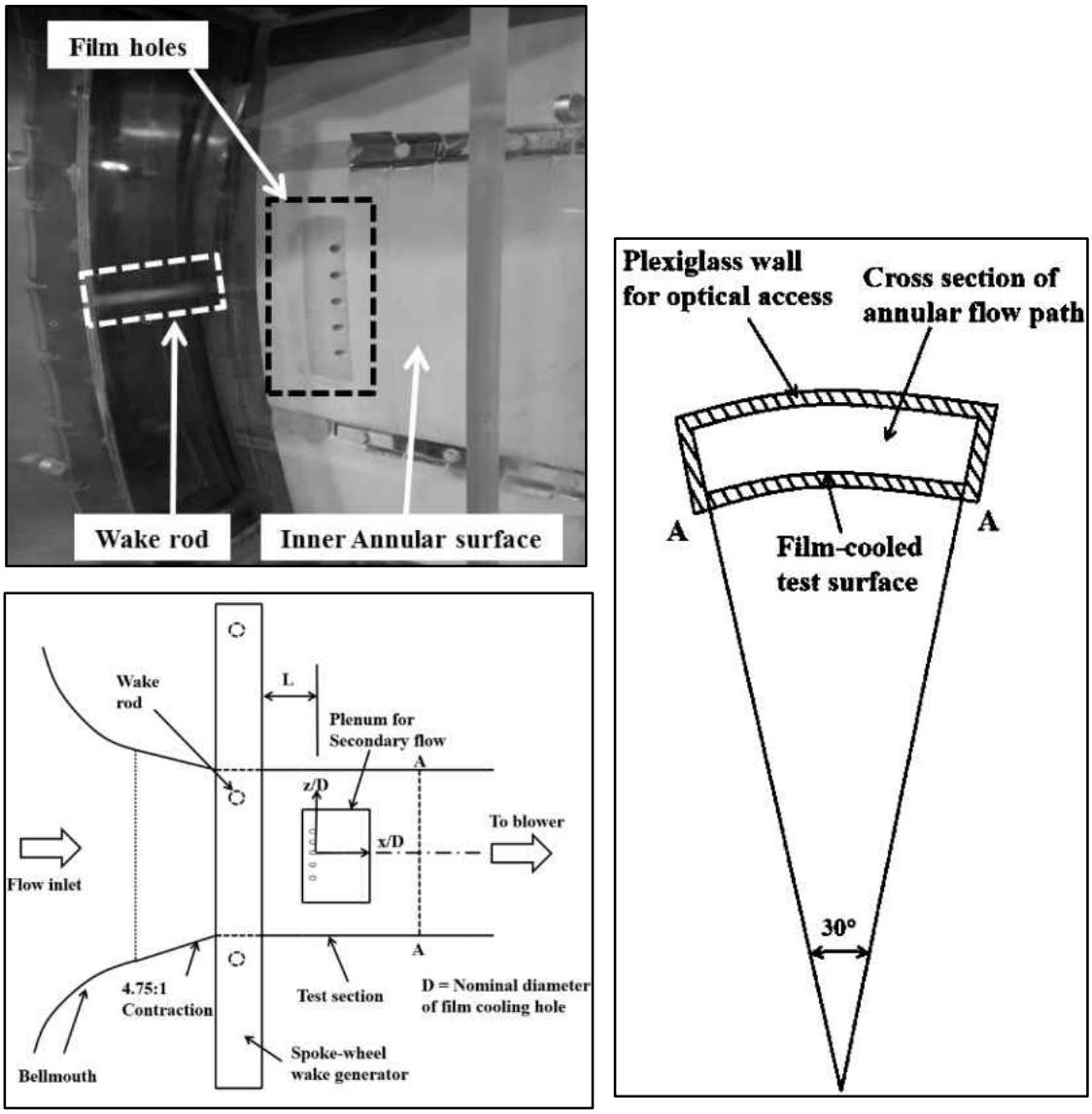

Figure 23: Schematic of experimental flow loop

Due to the presence of the wake generator casing, the mainstream flow was tripped at the wake generator interface which made the boundary layer turbulent. No extra

sandpaper trip was used for this purpose. The boundary layer thickness (evaluated at 99% of U_∞) measured in the absence of the wakes was ≅ 1.58D at the film injection location. From the measured velocity profile, the displacement and momentum thickness were calculated to be ≅ 0.322D and 0.193D respectively which yields a shape factor of 1.66 approximately. The top and bottom of the pitchwise-curved surface extend ± 15 degrees from the centerline.

Heat Transfer Measurements

For the heat transfer measurements, a constant heat flux boundary condition was needed. Discrete strips of stainless steel foils are adhered to a 1.27 cm low thermal conductivity material (k ≅ 0.028 W/mK) called 'Rohacell' (Model - RIMA 110, Evonik Inc.) using Kapton tape. The Rohacell surface is glued to a polycarbonate substrate (k = 0.2 W/mK) for increased structural strength. The back side heat conduction loss was measured to be < 3%. The Kapton tape is made from Kapton polyimide film with silicon adhesive. The thickness ranges between 0.025 mm to 0.127 mm and they are compatible over a wide temperature range (-269°C to 400°C) with a thermal conductivity of ≅ 0.5 W/mK and an electrical resistance of 1×10^{12} ohms approximately. The lowest thickness Kapton tape was used with the foil heaters.

The stainless steel (type 321) foil heater strips of nominal thickness (≅ 51μm) were connected in series using copper bus bars to increase the total resistance of the foil. Volumetric or Joule heating of the stainless steel foil is achieved by passing electric current through the copper bus bars. The density ratio was maintained approximately at 1 for all

the heat transfer experiments with the mainstream and coolant flow at ≅ 23°C. The test surface setup and the cross section of the coolant plenum are shown in Figure 24.

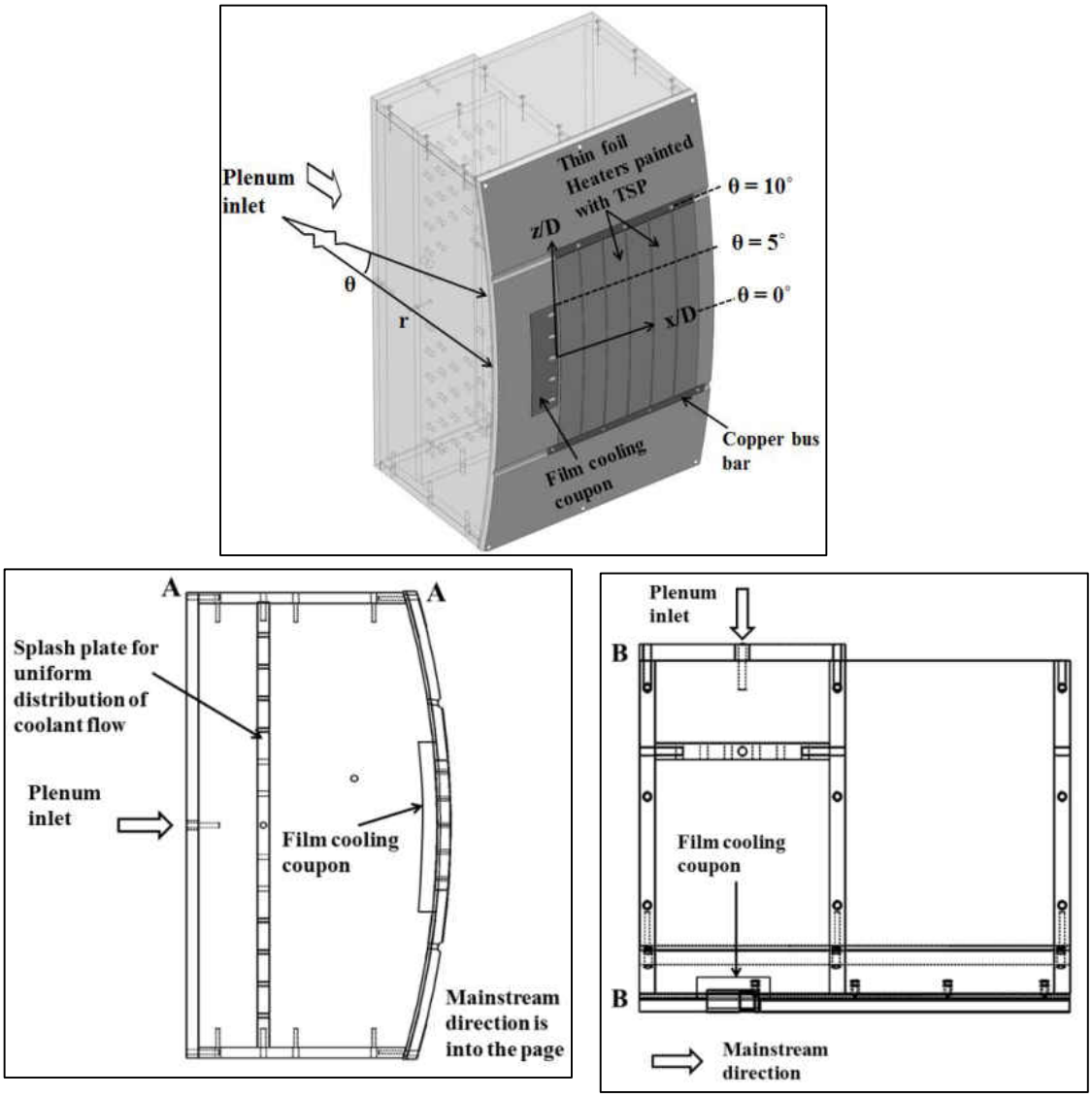

Figure 24: Test surface setup for heat transfer measurements

The film cooling coupon was made using high resolution stereo-lithography with a step size of ≅ 0.1 mm. The inclination angle of the film cooling hole (α) was 35°, the compound angle (β) was 0°, and the L/D was 8. It was pointed out by Lutum and Johnson

[2] that a film hole L/D > 5 reduces the premature jet lift-off especially at higher blowing ratios. The p/D was maintained at 3 for all the experiments. The film injection location was located ≅ 8.83D downstream of the wake generator inlet. The coolant flow is supplied from a plenum that contains a perforated plate near the compressed air inlet which disrupts the jetting of the compressed air flow to provide close to a uniform flow at the film cooling coupon inlet. A pressure regulator and a calibrated thermal mass flow meter (Model - FMA 1843, Omega Inc.) are used to establish control over the coolant flow rate.

In the downstream region of the test section (≅ 23D from the exit of the film cooling hole), two T-type thermocouples were placed touching the test surface to measure the recovery temperature. There was negligible difference between the two thermocouple readings. In addition to this, local recovery temperature measurements were taken using the TSP technique. The measurements indicated negligible variation in the recovery temperature on the test surface. The test matrix for the heat transfer measurements is given in Table 2.

Table 2: Test matrix for heat transfer measurements

Cooling method	Measurement	M	I	VR	DR	S	d/D
Discrete film (Cylindrical hole)	Heat transfer	0	0	0	1	0,0.15,0.3	2.375
		0.25	0.062	0.25			
		0.5	0.25	0.5			
		0.75	0.562	0.75			

Endwall Film Cooling in a High Subsonic Annular Cascade

Mainstream Flow

The experiments were conducted in a high subsonic 25˚ sector-annular cascade. This comprised four full airfoils and two half-airfoils resulting in five airfoil passages. The airfoils represent a 3X-scaled model of the first rotor stage of the GE-E^3 engine. Since a cascade is operated under stationary conditions, the velocity triangles do not differ along the span of the airfoil unlike a real gas turbine which involves rotation. In order to maintain close to zero incidence angle throughout the airfoil span, the mid-span profile of the rotor was used for the cross section of the low aspect ratio airfoil. The specifications of the airfoil and the approximate flow angles are given in Table 3. The cascade mainstream flow loop and the studied airfoil passage is shown in Figure 25.

Table 3: Airfoil geometry specifications and flow angles

Parameter	Value
Aspect ratio	1.2
Span	12.7 cm
Incidence angle	≅ 0˚
Inlet flow angle	≅ 43˚
Outlet flow angle	≅ -67˚

During the design phase of the cascade, tail boards were used to adjust the mass flow between the airfoil passages to achieve periodicity. This is necessary to imitate the presence of numerous airfoil passages similar to a real gas turbine. More details on the complete design and flow analysis of the cascade can be found in McDonald [3]**.** The flow periodicity between airfoil passages 2,3,4 were measured on the outer endwall using static

pressure taps. The static pressure on inner endwall of passage-3 was measured using the Pressure Sensitive Paint technique and compared with the static pressure tap data on the outer endwall (see chapter 8, Figure 46). A 350 hp (261.1 kW) centrifugal blower was used to provide the required mass flow in the cascade tunnel which is operated in an open flow loop configuration under suction. A flow conditioning section (with one honeycomb and two mesh screens) followed by two 3.2:1 contractions ensures close to a uniform inlet flow to the test section. In order to isolate the propagation of blower non-uniformities into the test section, the exit flow is directed to a large plenum through a straight duct and a diffuser. Optical access is provided using plexiglass endwalls manufactured using the thermal-forming process by House of Plastics Unlimited.

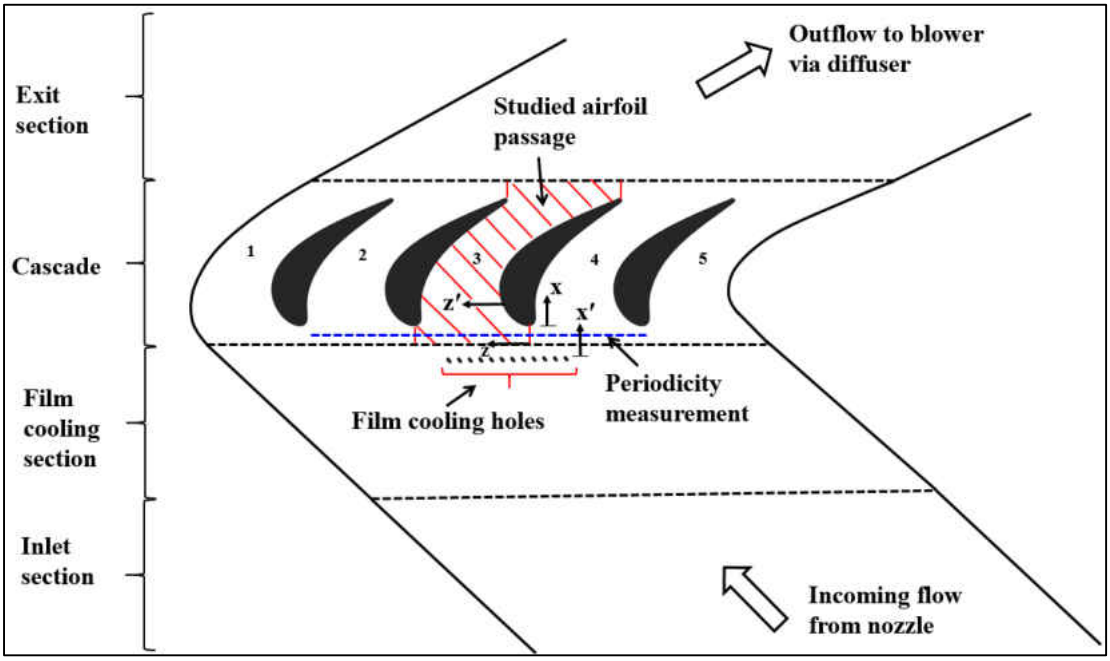

Figure 25: Schematic of the high subsonic cascade tunnel flow loop

The average mainstream flow velocity (U_∞) was kept constant at ≅ 105 m/s at the inlet of the cascade for all the experiments. The mainstream flow was at room temperature that

varied between 23°C and 29°C depending on the ambient conditions during different tests. The flow parameters were monitored closely during all experiments to ensure that the required corrections were made in the coolant flow rate. The turbulence intensity in the streamwise direction was measured using a TSI IFA 300 hot wire anemometer using a 50 μm diameter probe (TSI T1201) at the exit plane of nozzle 2-C (see chapter 8, Figure 44). The average value of the mainstream turbulence intensity in the bulk flow region was ≅ 1.8%. The average fluid velocities in the pitchwise direction were verified using Pitot-static tube measurements.

Due to certain experimental rig access constraints, the incoming velocity profile was obtained from computations. Details on the computational model are provided in chapter 8. The Mach number at the film injection location (Ma_{inj}) and at the throat (Ma_t) were 0.29 and 0.68 approximately. The Reynolds number based on the average mainstream velocity at film cooling hole exit and the airfoil true chord was calculated to be $\cong 6.43\times10^5$. The coolant jet Reynolds number based on the average mainstream velocity at film cooling hole exit and the film cooling hole diameter was calculated to be $\cong 1.21\times10^4$. From the CFD predictions, the mainstream boundary layer, displacement, and momentum thickness were calculated to be 6.312 D (0.099 S), 0.526 D (0.008 S), and 0.389 D (0.006 S) at the film injection location for the averaged hydrodynamic boundary layer (average of 12 individual hole exit mainstream boundary layer profiles). The resulting boundary layer shape factor was calculated to be ≅ 1.35. The predicted boundary layer profiles are shown in Figure 26.

Film Cooling Effectiveness Measurements

A 2.54 cm thick thermal formed plexiglass curved wall with a thermal conductivity of 0.2 W/mK (Evonik Inc.) was used for the test surface. Based on a typical airfoil leading-edge diameter to film cooling hole diameter ratio and location in an aircraft engine and the feasibility of the experimental setup, the film cooling hole diameter and upstream film injection distance were selected. A total of 12 film cooling holes (based on one geometric airfoil pitch) are placed ≅ 20 mm upstream of the airfoil leading-edge. The film cooling holes are cylindrical in cross section with a nominal diameter (D) of 2 mm. The p/D was maintained at ≅ 3.55 for all the experiments. The streamwise inclination angle (α) of the film cooling hole was 30°, the compound angle (β) was ≅ 0° (at the film injection location), resulting in a L/D of 17 approximately. It was pointed out by Lutum and Johnson [2] that a film cooling hole with L/D > 5 does not experience undeveloped flow inside the hole or an increased effective inclination angle especially at higher blowing ratios.

The coolant flow is supplied from a plenum that contains a perforated plate near the compressed air inlet which disrupts the jetting of the inlet air flow to provide close to a uniform flow at the film cooling hole inlet. A pressure regulator and a calibrated thermal mass flow meter (Model-GFM 77, Aalborg Inc.) were used to establish control over the coolant flow rate. Prior to injection into mainstream, the coolant fluid is heated using two inline heaters to ≅ 72°C as measured at the entrance to the coolant hole. Since the film hole diameter is very small (≅ 2 mm), inserting a thermocouple (bead diameter ≅ 1mm) into the hole to measure the temperature drop across the hole can cause significant blockage

and disturbance to the coolant flow. Due to this, the temperature drop across the coolant hole was obtained from conjugate heat transfer simulations detailed in chapter 8.

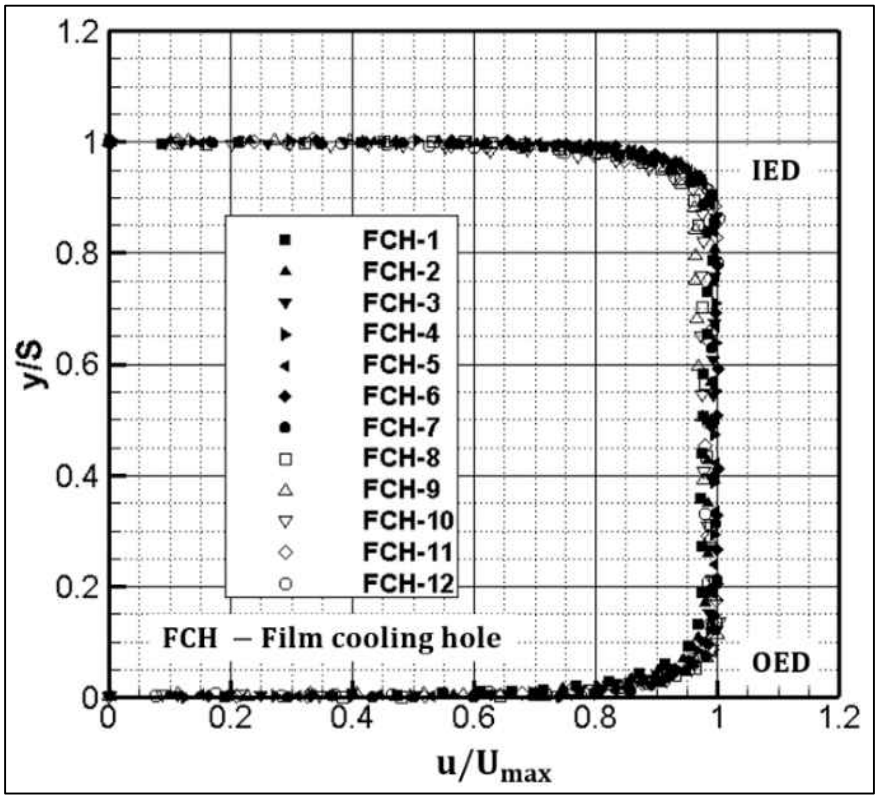

Figure 26: Predicted mainstream hydrodynamic boundary layer

On an average, the temperature difference between the coolant exit and the mainstream was ≅ 37.4°C, resulting in a coolant to mainstream density ratio of 0.89 approximately. The recovery temperature on the test surface was measured using the TSP technique. In addition two T-type (Copper-Constantan) thermocouples were placed touching the test surface at the exit of the airfoil passage-3 to validate the TSP measurements. The coolant flow setup is shown in Figure 27. The test matrix for the film cooling effectiveness and surface oil visualization experiments is given in Table 4 and Table 5 respectively.

Table 4: Test matrix for endwall film effectiveness measurements

Cooling method	Measurement	M_{avg}	I_{avg}	DR	p/D	L/D	Case no.
Discrete film (Cylindrical hole)	Film cooling effectiveness	0.56	0.35	0.89	3.55	17	1
		0.83	0.77				2
		1.11	1.38				3

Table 5: Test matrix for surface oil visualization experiments

Cooling method	Measurement	M_{avg}	I_{avg}	DR	p/D	L/D	Case no.
Discrete film (Cylindrical hole)	Saddle point shift	0	0	1	3.55	17	-
		0.56	0.31				1
		0.83	0.69				2
		1.11	1.23				3

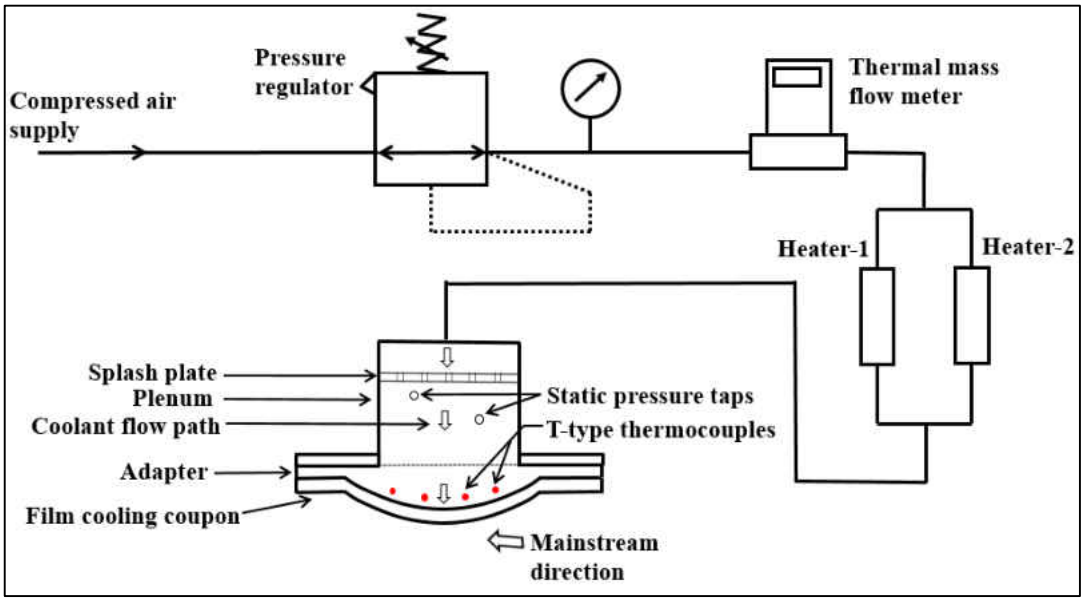

Figure 27: Coolant flow setup for film cooling effectiveness measurements

References

[1] Golsen, M., Ricklick, M., and Kapat, J.S., "Investigation of the Effects of Rod to Film Cooling Hole Diameter Ratio in Unsteady Wake Studies", 47th AIAA/ASME/SAE/ASEE Joint Propulsion Conference & Exhibit, AIAA 2011-6096, 2011.

[2] Lutum, E., and Johnson, B. V., 1998, "Influence of hole length-to-diameter ratio on film cooling with cylindrical holes", *Journal of Turbomachinery*, Vol. 121, pp. 209-216.

[3] McDonald, W. J., 2008, "Design and computational analysis of aerodynamics in an annular cascade", *Undergraduate Honors Thesis*, University of Central Florida, Orlando, USA.

CHAPTER 6: EQUATIONS AND DATA REDUCTION

Mainstream Flow

The flow Reynolds number can be defined based on the (i) entry length (L) which is measured from the starting point of the test surface to the trailing edge of the film hole in the case of a flat plate, (ii) airfoil true chord (C) in the case of a cascade, and (iii) the film cooling hole diameter (D) in the case of film injection The entry length definition is used to ascertain the inlet boundary layer thickness at the point of film injection. The definition based on the airfoil chord is used for scaling with engine conditions. Defining the Reynolds number based on the film cooling hole diameter enables better understanding of the flow field near the film injection location. The Reynolds number definitions are given in Equations 6.1, 6.2 and 6.3.

$$Re_L = \frac{U_\infty L}{\nu} \tag{6.1}$$

$$Re_C = \frac{U_\infty C}{\nu} \tag{6.2}$$

$$Re_D = \frac{U_\infty D}{\nu} \tag{6.3}$$

The flow compressibility is quantified using the Mach number, defined in Equation 6.4.

$$Ma_\infty = \frac{U_\infty}{\sqrt{(\gamma R T_\infty)}} \tag{6.4}$$

where, U_∞ and T_∞ are the free-stream velocity and static temperature respectively.

The inlet boundary layer thickness was calculated based on 99% of the free-stream velocity. Following this, the displacement and momentum thicknesses were calculated as shown in Equations 6.5 and 6.6.

$$\delta_1 \approx \int_0^{\delta} \left(1 - \frac{u(y)}{U_\infty}\right) dy \tag{6.5}$$

$$\delta_2 \approx \int_0^{\delta} \frac{u(y)}{U_\infty}\left(1 - \frac{u(y)}{U_\infty}\right) dy \tag{6.6}$$

The turbulence intensity is calculated as shown in Equation 6.7.

$$Tu = \frac{u'_{RMS}}{U_\infty} \tag{6.7}$$

Coolant Flow

The coolant-to-mainstream mass flux ratio (or blowing ratio) and the momentum flux ratio defined in Equation 6.8 and Equation 6.9 quantify the relative strength of the coolant jet compared to the mainstream flow on a local basis.

$$M = \frac{\rho_c U_c}{\rho_\infty U_\infty} \tag{6.8}$$

$$I = \frac{\rho_c {U_c}^2}{\rho_\infty {U_\infty}^2} = \frac{M^2}{DR} \tag{6.9}$$

where, DR is the density ratio of the coolant to mainstream which was held approximately constant at 0.89 and 1 for film cooling effectiveness and heat transfer measurements respectively.

Since there is a variation in the blowing ratio between the film cooling holes in a cascade, an average blowing ratio definition is necessary as shown in Equation 6.10.

$$M_{avg} = \frac{\rho_c U_{c,avg}}{\rho_\infty U_{\infty,avg}} \tag{6.10}$$

where, $U_{c,avg}$ and $U_{\infty,avg}$ are the averaged coolant and free-stream velocities at the film injection location.

Discharge Coefficient

In order to quantify the individual film cooling hole discharge coefficient, the coolant plenum total pressure, film cooling hole exit static pressure (for the no film cooling case), and the actual mass flow rate through each film cooling hole was obtained from computations. The discharge coefficient for a compressible flow based on Rowbury et al. [1] is defined in 6.11.

$$C_d = \frac{\dot{m}_{act}}{A_h P_{o,c} \left(\frac{P_{s,\infty}}{P_{o,c}}\right)^{\frac{1}{\gamma}} \left[\left\{\left(\frac{P_{o,c}}{P_{s,\infty}}\right)^{\frac{\gamma-1}{\gamma}} - 1\right\} \frac{2\gamma}{\gamma-1} \frac{1}{RT_{o,c}}\right]^{0.5}} \tag{6.11}$$

Pressure Coefficient

In order to quantify the periodicity between the airfoil passages, the static pressure was measured on the outer endwall using static pressure taps. On the inner endwall, pressure sensitive paint was used to measure the static pressure in the airfoil passage-3. A pressure coefficient is defined in Equation 6.12 which provides a normalized representation

of the static pressure variation on the endwall. The free-stream velocity, density, and static pressure used in Equation 6.12 were obtained at the exit plane of nozzle 2-C (see Figure 44, chapter 8).

$$C_p = \frac{(P - P_\infty)}{\frac{\rho_\infty U_\infty^2}{2}} \tag{6.12}$$

Saddle Point Shift

The saddle point distance from the airfoil leading-edge provides a measure of the horseshoe vortex location. With coolant injection, the shift in the saddle point relative to the baseline (i.e. no coolant injection) case is quantified as shown in Equation 6.13.

$$SP_{shift} = 100 * \frac{SP}{D_{LE}} \tag{6.13}$$

where, D_{LE} is the leading-edge diameter of the airfoil and SP is the distance of the saddle point from the airfoil leading-edge.

Wake Strouhal Number

A wake Strouhal number can be defined as the ratio of rod velocity to the free-stream velocity as shown in Equation 6.14. The wake tangential velocity is influenced by rod rotational speed, number of rods, and the rod diameter.

$$S = \frac{2\pi\ N\ d\ n}{60\ U_\infty} \tag{6.14}$$

Film Cooling Effectiveness

A non-dimensional temperature called the film cooling effectiveness is used to quantify the efficiency of film cooling on a local basis. It is defined in Equation 6.15 and comprises three temperatures namely, the adiabatic wall temperature (measured by TSP), recovery temperature (measured by TSP), and the coolant temperature. The coolant temperature is measured using 4 T-type (Copper-Constantan) thermocouples placed near the coolant hole inlet.

For the cascade film cooling experiments, the temperature drop across the coolant hole was obtained from conjugate heat transfer simulations explained in chapter 8. This was due to the significantly small diameter of the film cooling hole compared to the unsteady wake experiment. The corrected coolant temperature is used for T_c in Equation 6.15. Due to the hot mainstream flow in a real gas turbine, the coolant temperature is lower than the recovery and film (i.e adiabatic wall) temperature and so the definition of film effectiveness needs to be adjusted accordingly. The pitch-averaged film effectiveness is calculated by integrating the local effectiveness values along the pitchwise coordinate at discrete streamwise locations along the airfoil axial chord. These integrated quantities are then averaged to obtain a single value, representative of the entire pitch extent for a given streamwise location. The pitch-averaged film cooling effectiveness is defined in Equation 6.16.

$$\eta(x,z) = \frac{(T_{aw} - T_r)}{(T_c - T_r)} \tag{6.15}$$

$$\bar{\eta}(x) = \frac{\int \eta(x,z)\ dz}{\int dz} \tag{6.16}$$

In Equations 6.15 and 6.16, 'x' is the streamwise coordinate with origin at the airfoil leading-edge, 'z' is the pitchwise coordinate ($dz \cong Rd\theta$) with origin at the airfoil leading-edge and 'R' is the radius of the test surface. In the case of the unsteady passing wake study, 'x' and 'z' are the streamwise and pitchwise coordinates with origin at the trailing edge of the film cooling hole. In Equation 6.16, the pitchwise integration for $\bar{\eta}(x)$ was performed for $0.05 \leq z'/p \leq 0.95$ between $x/C_{ax} = 0$ and $x/C_{ax} = 0.8$.

A cooling uniformity coefficient (CUC) is defined in Equation 6.17 as an additional parameter to interpret the uniformity in film cooling effectiveness for the case of endwall film cooling.

$$CUC = \frac{\eta(x,z)}{\bar{\eta}(x)} \tag{6.17}$$

where, $\bar{\eta}(x)$ is the pitch-averaged film cooling effectiveness at each streamwise location. A CUC value > 1 implies an over-cooled region and vice-versa.

Heat Transfer

The measured voltage (V) input and heater resistance are first converted into an input heat flux after accounting for the heater surface area exposed to the mainstream flow (A_s). The heat flux generated by the heater is given in Equation 6.18.

$$q''_{gen} = \frac{V^2}{R_{el} \times A_s} \tag{6.18}$$

Since the resistivity of the stainless steel heater changes with temperature, a curve fit for resistivity versus temperature was used to correct for the changes in heater resistance during the experiment. The heater resistance defined in Equation 6.19 is calculated using

the resistivity and the dimensions of the heater. The length (l) of the heater is measured in pitchwise direction while the width (w) is measured in the streamwise direction. The thickness (t) of the stainless steel foil is measured in the wall-normal ('y') direction.

$$R = \frac{(\rho_{el} \times l)}{(w \times t)} \tag{6.19}$$

The actual heat flux out of the test surface into the flow is obtained after accounting for the heat conduction and radiation losses. Figure 28 shows a schematic of the test surface with the various heat losses. The heat losses and the actual heat flux input are defined in Equations 6.20-6.22.

$$q''_{act} = q''_{gen} - q''_{cond} - q''_{rad} + q''_{lat} \tag{6.20}$$

The heat generated by the heater varies for each experimental case. The lateral conduction calculation procedure is explained here. The first step involves obtaining the temperature distribution on the heater in the 'x' and 'z' directions from the temperature sensitive paint. The temperature gradient is then evaluated based on the temperature profile. By plotting the temperature gradient versus the 'x' and 'z' coordinate, the high temperature gradient locations are ascertained. These locations are then used as central nodes for performing the lateral conduction calculation with ≅ 8 nodes on either side of the central node to obtain a reasonable representation of the temperature gradient variation. This was done for the first two heaters since the downstream heaters exhibited close to uniform temperature along the test surface.

Figure 29 shows the temperature contour for M = 0.75; S = 0.3 with a typical control volume that was used for evaluating the lateral conduction. The lateral conduction calculation was performed for two cases (M = 0; S = 0 & M = 0.75; S = 0.3) to get an upper

and lower bound value. When comparing the values between the two cases, the maximum value of lateral conduction (≅ 6.33% of q''_{gen}) was observed on heater 1 for M = 0.75; S = 0.3. Correction for lateral conduction was not considered in the calculation of the actual heat flux since the typical uncertainty in q''_{gen} was greater than the lateral conduction contribution for the evaluated cases.

The conduction loss given in Equation 6.21 from the backside of the heater for the maximum temperature difference was calculated to be 2.3% approximately, which was within the uncertainty of the heat flux in the experiment and thus was not considered in the energy balance. The radiation heat loss was accounted by using a blackbody radiation exchange model (ε = 1) for the heater surface as given in Equation 6.22.

$$q''_{cond} = \left(\frac{L_{rohacell}}{k_{rohacell}}\right)^{-1}(T_b - T_{amb}) \tag{6.21}$$

$$q''_{rad} = \varepsilon\sigma(T_w^4 - T_{amb}^4) \tag{6.22}$$

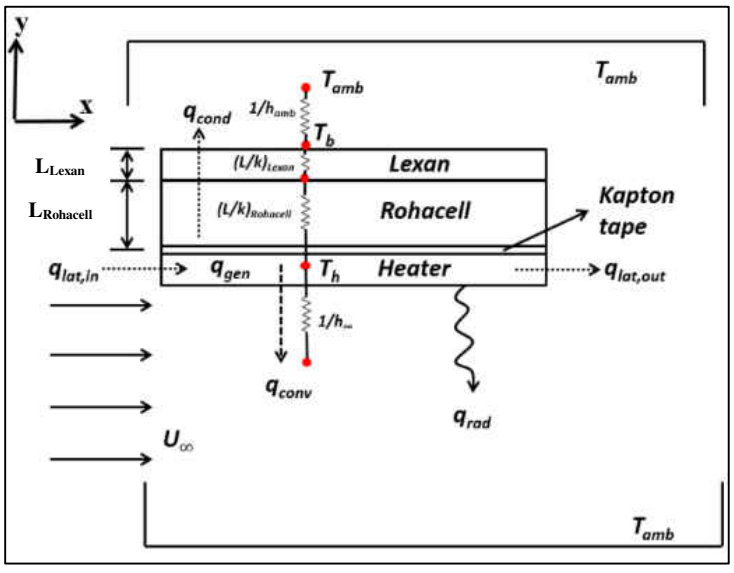

Figure 28: Heat losses in unsteady passing wake study

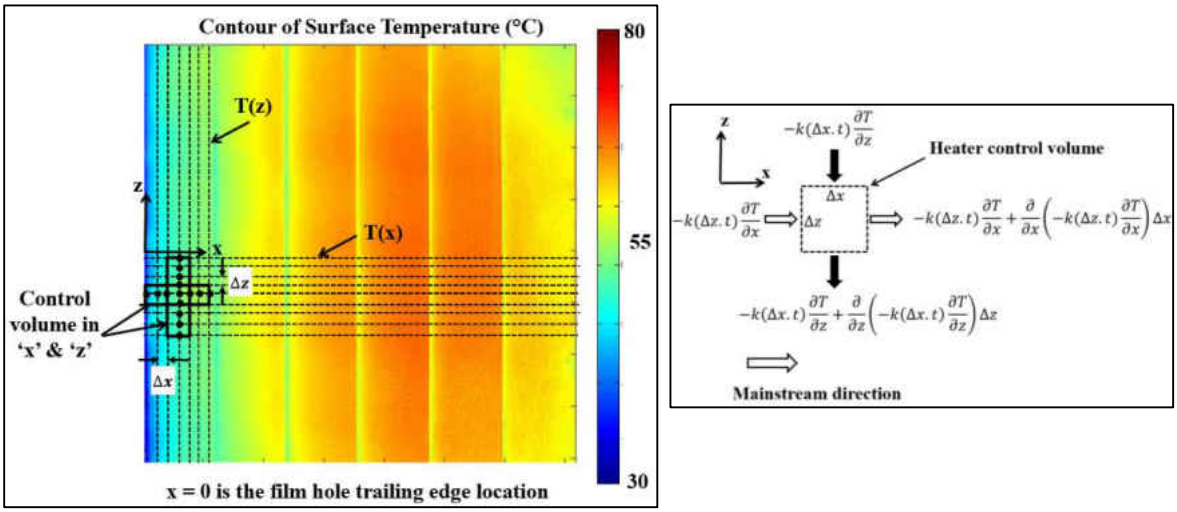

Figure 29: A typical control volume on test surface and energy balance

The lateral heat conduction is defined in Equation 6.23.

$$q''_{lat} = k\left(\frac{\partial^2 T}{\partial x^2}(\Delta x) + \frac{\partial^2 T}{\partial z^2}(\Delta z)\right) \tag{6.23}$$

The radiation heat loss was found to be the highest (≅ 10.8% of q''_{gen}) on heater 2 for M = 0; S = 0. This is because the highest temperature was observed on heater 2 when compared to heater 1. It was found that heaters downstream of heater 2 had a radiation heat loss less than heater 2. The radiation heat loss is accounted in the energy balance before arriving at the convective heat flux on the heater surface. The heat transfer coefficient is defined in Equation 6.24.

$$h = \frac{q''_{act}}{T_w - T_r} \tag{6.24}$$

The pitch-averaged heat transfer coefficient given in Equation 6.25, is calculated using a method similar to the film cooling effectiveness.

$$\bar{h}(x) = \frac{\int h(x,z)\ dz}{\int dz} \tag{6.25}$$

In Equation 6.25, the pitchwise integration for $\bar{h}(x)$ was performed for -3 ≤ z/D ≤ 3 between x/D = 1 and x/D = 14.

A heat transfer augmentation is defined in Equation 6.26 to quantify the impact of film injection and / or passing wake on heat transfer. This is a non-dimensional parameter which is the ratio of heat transfer with film cooling and / or passing wake to that without film cooling and no wake.

$$h_{aug} = \frac{\bar{h}}{\overline{h_o}} \tag{6.26}$$

References

[1] Rowbury, D. A., Oldfield, M. L. G., Lock, G. D., and Dancer, S. N., 1998, "Scaling of film cooling discharge coefficient measurements to engine conditions", *Proceedings of the International Gas Turbine and Aeroengine Congress and Exposition*, 98-GT-79, pp. 1-8.

CHAPTER 7: UNCERTAINTY ANALYSIS

A detailed uncertainty analysis was carried out to calculate both the systematic and random error in the experimental data. The analysis was performed based on the partial differentiation method proposed by Moffat [1] with a 95% confidence interval. Each measurand is split into numerous independent parameters which contribute to the total uncertainty. The systematic uncertainty (or bias) is obtained from the instrument specifications provided by the manufacturer. The random (or precision) uncertainty is calculated based on the standard deviation of the individual data sets (obtained from repeatability experiments) from the average data set for a fixed confidence interval.

Method of Error Propagation

The dependence of a resultant (R) can be expressed as shown in Equation 7.1.

$$R = R(X_1, X_2, X_3, X_4, \dots, X_N) \tag{7.1}$$

where $X_1, X_2, X_3, X_4, \dots, X_N$ are the independent parameters (measurands) contributing to the uncertainty in R. The uncertainty in R with respect to X_i is given in Equation 7.2.

$$uR_{X_i} = \frac{\partial R}{\partial X_i} uX_i \qquad for\ i = 1,2 \dots, N \tag{7.2}$$

where, $\frac{\partial R}{\partial X_i}$ is often called the sensitivity index or sensitivity coefficient for R with respect to X_i and u refers to the uncertainty of the measurand.

On combining all the independent variables that influence the uncertainty in 'R', Equation 7.3 is obtained.

$$uR = \sqrt{\left(\frac{\partial R}{\partial X_1} uX_1\right)^2 + \left(\frac{\partial R}{\partial X_2} uX_2\right)^2 + \left(\frac{\partial R}{\partial X_3} uX_3\right)^2 + \cdots + \left(\frac{\partial R}{\partial X_N} uX_N\right)^2} \qquad (7.3)$$

In Equation 7.3, the uX_N value called the total uncertainty contains both the systematic and random uncertainty combined using the root-sum-square method [1]. The validity of Equation 7.3 is based on satisfying the following conditions [1].

a) Every measurement made was independently.

b) Repetitions of the measurement will result in a Gaussian distribution.

c) The same confidence interval was used for each measurement uncertainty.

Uncertainty Tree

An uncertainty tree breaks down the various contributing measurands for a particular measurement quantity. This can help trace the high uncertainty measurands. The uncertainty tree for the measured quantities in the present study are given in Figures 30-41.

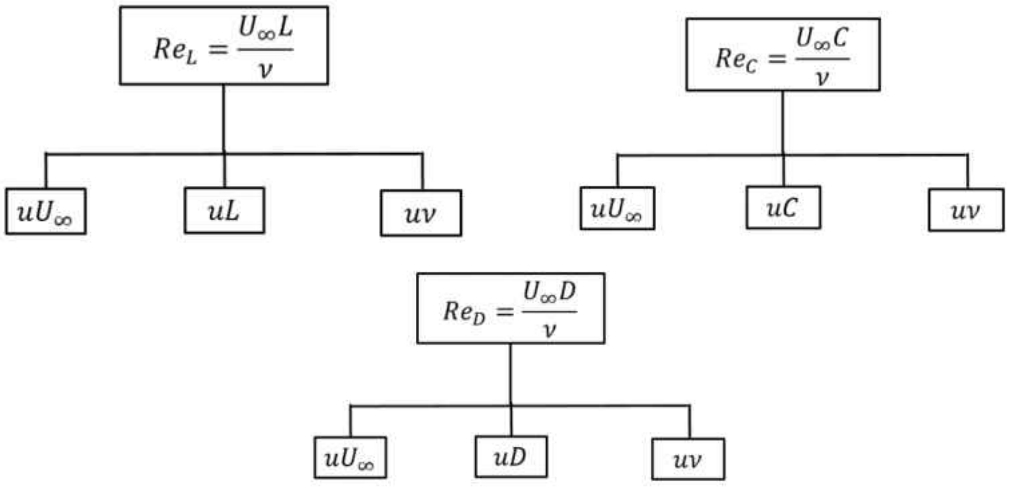

Figure 30: Uncertainty tree for Reynolds number

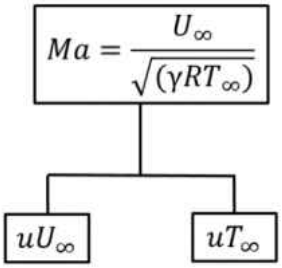

Figure 31: Uncertainty tree for Mach number

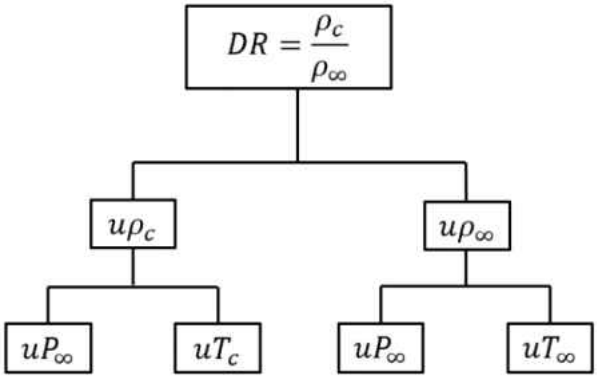

Figure 32: Uncertainty tree for density ratio

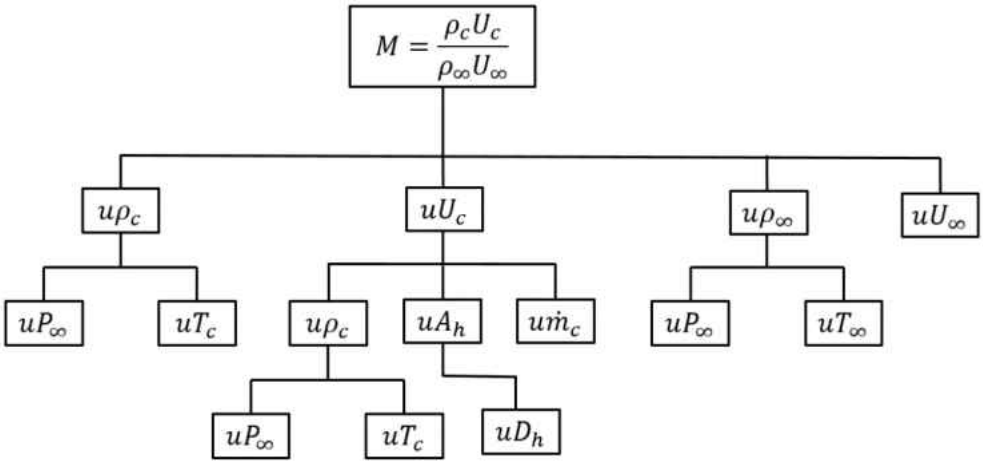

Figure 33: Uncertainty tree for blowing ratio

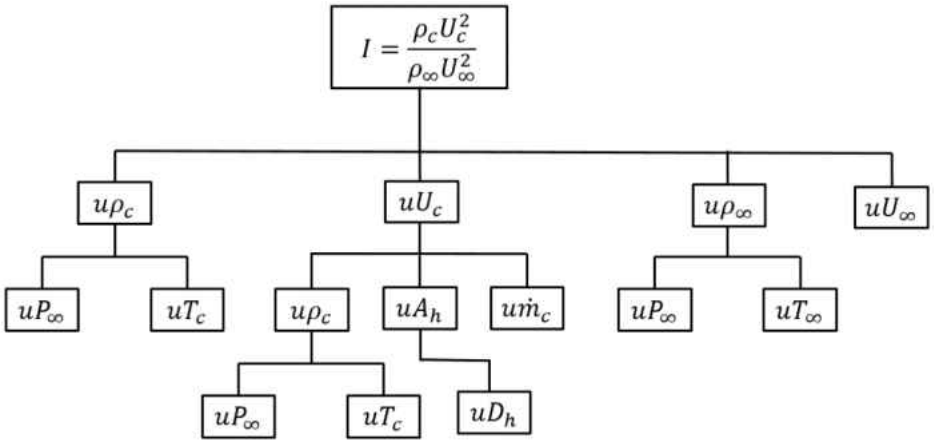

Figure 34: Uncertainty tree for momentum flux ratio

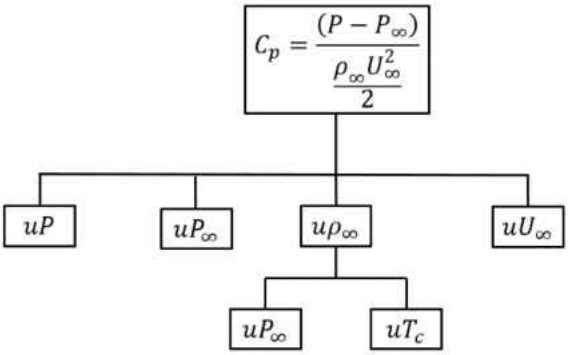

Figure 35: Uncertainty tree for pressure coefficient

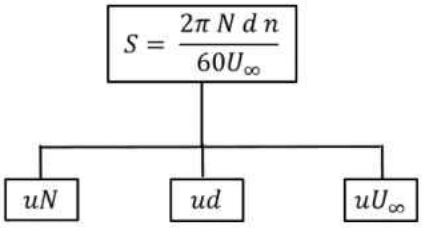

Figure 36: Uncertainty tree for Strouhal number

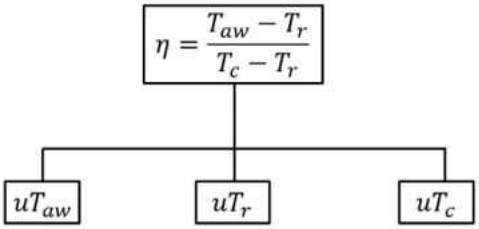

Figure 37: Uncertainty tree for film cooling effectiveness

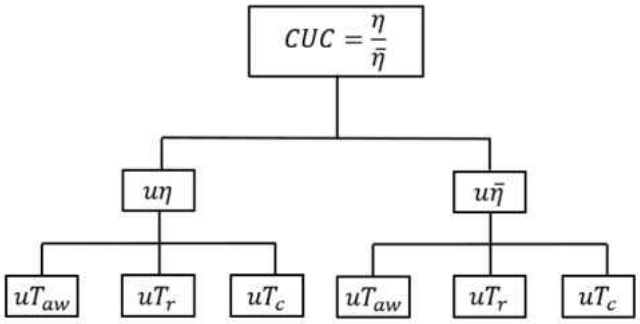

Figure 38: Uncertainty tree for cooling uniformity coefficient

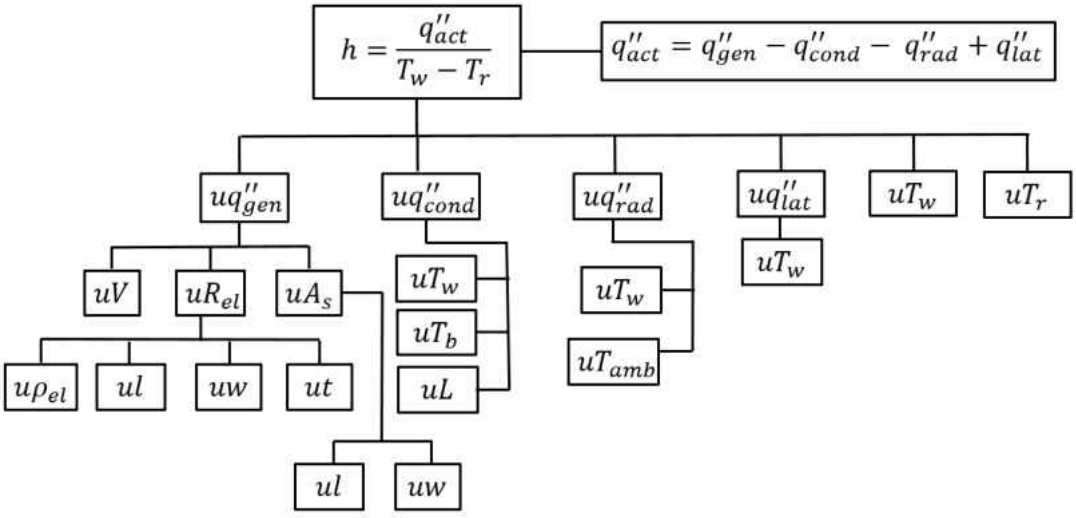

Figure 39: Uncertainty tree for heat transfer coefficient

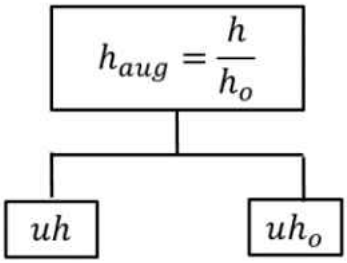

Figure 40: Uncertainty tree for heat transfer augmentation

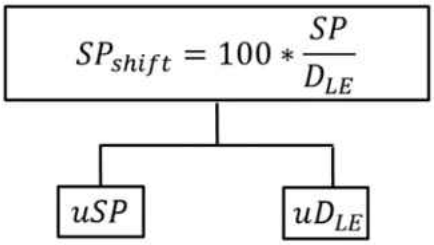

Figure 41: Uncertainty tree for saddle point shift

Total Uncertainty

A symbolic representation of the total uncertainty for the various measurement quantities and the total uncertainty values are given in Table 6. The error bars in the results reported in this study indicate the total uncertainty at each data point.

Table 6: Symbolic representation and magnitude of total uncertainty

Resultant	Expression	Symbolic expression for the total uncertainty	Total Uncertainty	
			Unsteady Wake Study	Cascade Study
Mach number	$Ma = \frac{U_\infty}{\sqrt{(\gamma R T_\infty)}}$	$uMa = \sqrt{\left(\frac{\partial Ma}{\partial U_\infty} uU_\infty\right)^2 + \left(\frac{\partial Ma}{\partial T_\infty} uT_\infty\right)^2}$	± 4.89%	± 4.83%
Reynolds number - A	$Re_L = \frac{U_\infty L}{\nu}$	$uRe_L = \sqrt{\left(\frac{\partial Re_L}{\partial U_\infty} uU_\infty\right)^2 + \left(\frac{\partial Re_L}{\partial L} uL\right)^2}$	± 4.41%	NA
Reynolds number - B	$Re_C = \frac{U_\infty C}{\nu}$	$uRe_C = \sqrt{\left(\frac{\partial Re_C}{\partial U_\infty} uU_\infty\right)^2 + \left(\frac{\partial Re_C}{\partial C} uC\right)^2}$	NA	± 5%
Reynolds number - C	$Re_D = \frac{U_\infty D}{\nu}$	$uRe_D = \sqrt{\left(\frac{\partial Re_D}{\partial U_\infty} uU_\infty\right)^2 + \left(\frac{\partial Re_D}{\partial D} uD\right)^2}$	± 4.18%	± 5.6%
Density ratio	$DR = \frac{\rho_c}{\rho_\infty}$	$uDR = \sqrt{\left(\frac{\partial DR}{\partial \rho_c} u\rho_c\right)^2 + \left(\frac{\partial DR}{\partial \rho_\infty} u\rho_\infty\right)^2}$	± 0.46%	± 0.49%
Blowing ratio	$M = \frac{\rho_c U_c}{\rho_\infty U_\infty}$	$uM = \sqrt{\left(\frac{\partial M}{\partial \rho_c} u\rho_c\right)^2 + \left(\frac{\partial M}{\partial \rho_\infty} u\rho_\infty\right)^2 + \left(\frac{\partial M}{\partial U_c} uU_c\right)^2 + \left(\frac{\partial M}{\partial U_\infty} uU_\infty\right)^2}$	± 6.4%	± 5.04%

Resultant	Expression	Symbolic expression for the total uncertainty	Total Uncertainty	
			Unsteady Wake Study	Cascade Study
Momentum flux ratio	$I = \frac{\rho_c U_c^2}{\rho_\infty U_\infty^2}$	$uI = \sqrt{\left(\frac{\partial I}{\partial \rho_c} u\rho_c\right)^2 + \left(\frac{\partial I}{\partial \rho_\infty} u\rho_\infty\right)^2 + \left(\frac{\partial I}{\partial U_c} uU_c\right)^2 + \left(\frac{\partial I}{\partial U_\infty} uU_\infty\right)^2}$	± 6.4%	± 10.04%
Pressure coefficient	$C_p = \frac{(P - P_\infty)}{\frac{\rho_\infty U_\infty^2}{2}}$	$uC_p = \sqrt{\left(\frac{\partial C_p}{\partial P} uP\right)^2 + \left(\frac{\partial C_p}{\partial P_\infty} uP_\infty\right)^2 + \left(\frac{\partial C_p}{\partial \rho_\infty} u\rho_\infty\right)^2 + \left(\frac{\partial C_p}{\partial U_\infty} uU_\infty\right)^2}$	NA	± 0.1 (absolute)
Strouhal number	$S = \frac{2\pi\, N\, d\, n}{60 U_\infty}$	$uS = \sqrt{\left(\frac{\partial S}{\partial N} uN\right)^2 + \left(\frac{\partial S}{\partial d} ud\right)^2 + \left(\frac{\partial S}{\partial U_\infty} uU_\infty\right)^2}$	± 1.18%	NA
Film cooling effectiveness	$\eta = \frac{T_{aw} - T_r}{T_c - T_r}$	$u\eta = \sqrt{\left(\frac{\partial \eta}{\partial T_{aw}} uT_{aw}\right)^2 + \left(\frac{\partial \eta}{\partial T_r} uT_r\right)^2 + \left(\frac{\partial \eta}{\partial T_c} uT_c\right)^2}$	± 0.03 - ±0.055 (absolute)	± 0.03 - ±0.035 (absolute)
Cooling uniformity coefficient	$CUC = \frac{\eta}{\bar{\eta}}$	$uCUC = \sqrt{\left(\frac{\partial CUC}{\partial \eta} u\eta\right)^2 + \left(\frac{\partial CUC}{\partial \bar{\eta}} u\bar{\eta}\right)^2}$	NA	± 0.19 (absolute)

Resultant	Expression	Symbolic Expression for the Total Uncertainty	Total Uncertainty	
			Unsteady Wake Study	Cascade Study
Radiation heat flux	$q''_{rad} = \varepsilon\sigma\left({T_w}^4 - {T_\infty}^4\right)$	$uq''_{rad} = \sqrt{\left(\frac{\partial q''_{rad}}{\partial T_w} uT_w\right)^2 + \left(\frac{\partial q''_{rad}}{\partial T_\infty} uT_\infty\right)^2}$	± 5.17%	NA
Conduction heat flux	$q''_{cond} = \frac{(T_w - T_b)}{(L/k)}$	$uq''_{cond} = \sqrt{\left(\frac{\partial q''_{cond}}{\partial T_w} uT_w\right)^2 + \left(\frac{\partial q''_{cond}}{\partial T_b} uT_b\right)^2 + \left(\frac{\partial q''_{cond}}{\partial L} uL\right)^2}$	± 1.2%	NA
Generated heat flux	$q''_{gen} = \frac{{V_{el}}^2}{R_{el}A_s}$	$uq''_{gen} = \sqrt{\left(\frac{\partial q''_{gen}}{\partial V_{el}} uV_{el}\right)^2 + \left(\frac{\partial q''_{gen}}{\partial R_{el}} uR_{el}\right)^2 + \left(\frac{\partial q''_{gen}}{\partial A_s} uA_s\right)^2}$	± 7.66%	NA
Actual heat flux	$q''_{act} = q''_{gen} - q''_{cond} - q''_{rad}$	$uq_{conv} = \sqrt{\left(\frac{\partial q''_{act}}{\partial q''_{gen}} uq''_{gen}\right)^2 + \left(\frac{\partial q''_{act}}{\partial q''_{cond}} uq''_{cond}\right)^2 + \left(\frac{\partial q''_{act}}{\partial q''_{rad}} uq''_{rad}\right)^2}$	± 7.7%	NA
Heat transfer coefficient	$h = \frac{q''_{act}}{T_w - T_r}$	$uh = \sqrt{\left(\frac{\partial h}{\partial q''_{act}} uq''_{act}\right)^2 + \left(\frac{\partial h}{\partial T_w} uT_w\right)^2 + \left(\frac{\partial h}{\partial T_r} uT_r\right)^2}$	± 3.29%	NA
Heat transfer augmentation	$h_{aug} = \frac{h}{h_o}$	$uh_{aug} = \sqrt{\left(\frac{\partial h_{aug}}{\partial h_o} uh_o\right)^2 + \left(\frac{\partial h_{aug}}{\partial h} uh\right)^2}$	± 5%	NA
Saddle point shift	$SP_{shift} = 100 * \frac{SP}{D_{LE}}$	$uSP_{shift} = \sqrt{\left(\frac{\partial SP_{shift}}{\partial SP} uSP\right)^2 + \left(\frac{\partial SP_{shift}}{\partial D_{LE}} uD_{LE}\right)^2}$	NA	± 7%

References

[1] Moffat, R.J., 1988, “Describing the uncertainties in experimental results”, *Journal of Experimental Thermal and Fluid Science*, Vol. 1, pp. 3–17.

CHAPTER 8: CFD MODELING

A CFD model was built replicating the cascade experimental setup closely in terms of geometry and boundary conditions. The geometry of the cascade was prepared using SolidWorks (Dassault Systems), a commercial CAD software. Since the experiments have limited instrumentation access in the cascade tunnel, the CFD model serves to provide valuable qualitative and quantitative information of the flow field.

Meshing Scheme

During the initial stage of the CFD model preparation, a structured (hexahedral) grid was generated for the baseline CFD model (i.e. without film cooling) using ICEM CFD (Ansys Inc.), a commercial CFD software [1]. Due to the mapped mesh condition for the entire CFD model, mesh refinement in a specific region increased the number of cells significantly in other regions of the computational model. The grid size could not be handled with the available computational facilities and so a hybrid mesh generated using StarCCM+ v10.02.012 (CD Adapco), a CFD commercial code [2] was used in this study.

A hexahedral (structured) meshing scheme was used near the walls of the computational domain maintaining the dimensionless wall distance (y^+) below 3.5 on all walls. The distribution of wall y^+ on the inner endwall is shown in Figure 42. The distance of the first cell from the wall was set to 0.013 mm from a preliminary shear stress calculation based on [2] and the target y^+ value. A two-layer all wall y^+ treatment described in [2] was used for the fluid continuum. The two-layer y^+ treatment blends the viscous sub-layer ($y^+ < 5$), buffer layer ($5 < y^+ < 30$) and the inertial sub-layer ($30 < y^+ < 200$) depending

on the value of y^+. Based on the thickness of the prism/boundary layer mesh, an appropriate growth factor is computed by the CFD software to enable a smooth transition from the structured mesh near the walls to a polyhedral mesh (unstructured) in the region away from the walls. All the interfaces had a conformal mesh to permit proper exchange of flow information. During grid refinement, the near wall cell distance was kept constant in order to obtain the same y^+ distribution for the various grids but with a different mesh size for the other cells.

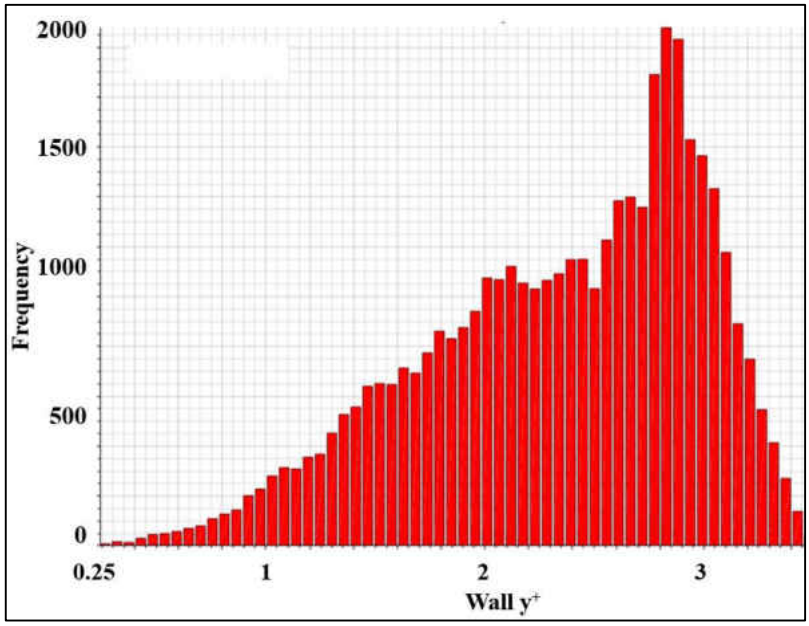

Figure 42: y^+ distribution on the inner endwall

Initial and Boundary Conditions

The boundary conditions were specified to closely replicate the flow conditions in the experiment. Since the entire computational domain with adequate mesh refinement was very large to analyze in a single simulation, the computations were performed in two parts. In the first part, the complete CFD domain shown in Figure 43 was analyzed for no the

film injection case. Although the coolant plenum and film cooling holes were not included in the baseline CFD model, the portion of the film cooling section connected to the mainstream flow was included in order to have the same hydrodynamic boundary layer at the cascade inlet. The inlet to nozzle-1 was defined as a stagnation inlet boundary. The measured pressure and temperature from the experiment was specified at this boundary. A mass flow boundary condition was specified at the outlet of the exit duct. The mass flow rate and temperature values from the experiment were specified at this boundary. The initial conditions were specified based on the experimental pressure, velocity and temperature data.

The second part of the computations were performed for the CFD domain shown in Figure 44 which excludes the first nozzle section and the first two parts of the second nozzle section. The film cooling holes, coupon, and the coolant plenum were included in the second CFD domain. The flow velocity components, total pressure, turbulent kinetic energy, turbulent dissipation rate and total temperature were mapped from the baseline simulation to the inlet of the second CFD domain. A mass flow boundary condition was specified at the outlet of the exit duct with the same values used in the baseline simulation. At the inlet of the coolant plenum, the total temperature and mass flow rate were specified. The physical and thermal properties for the plexiglass film cooling coupon (solid continuum) were obtained from the material data sheet provided by the manufacturer (Evonik Industries).

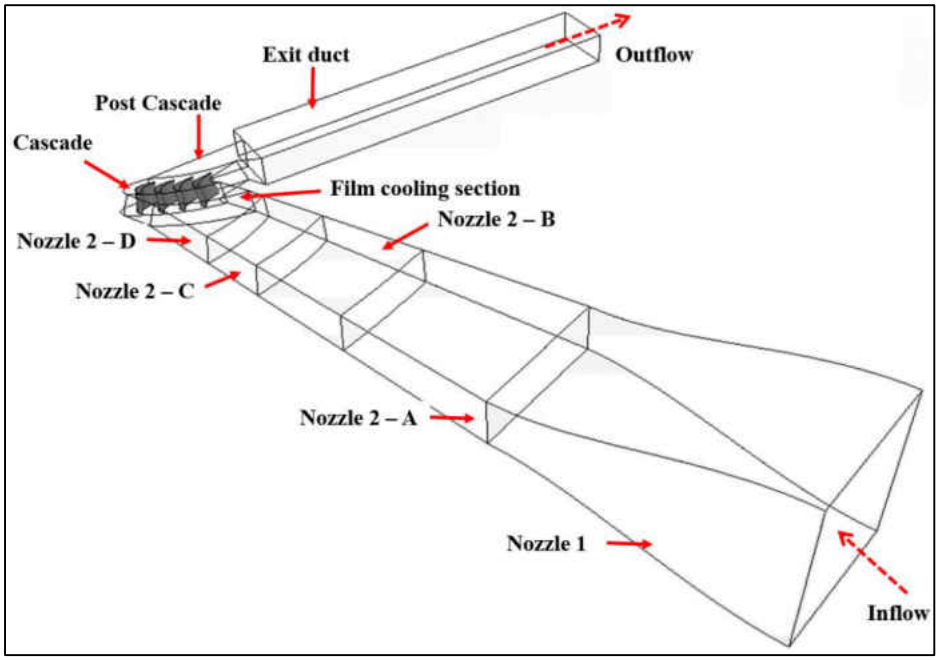

Figure 43: Baseline CFD model

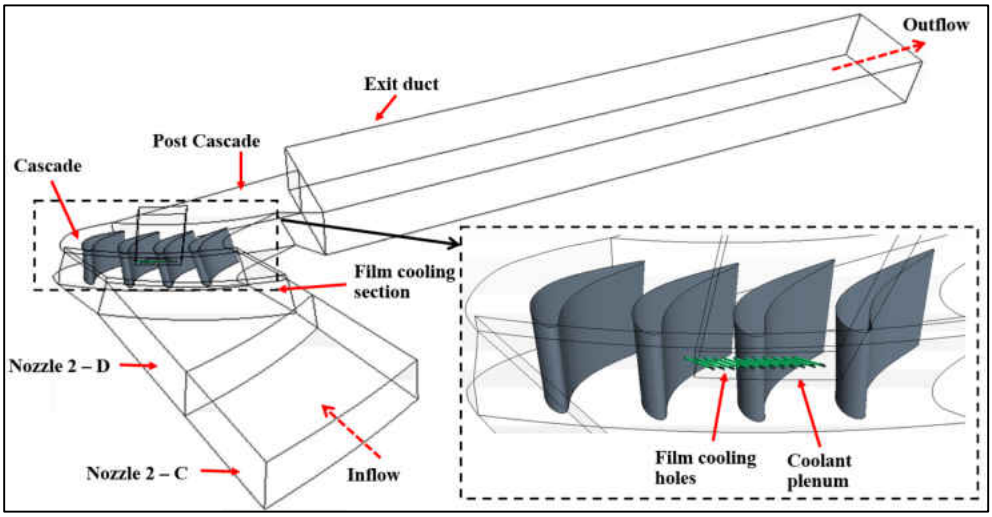

Figure 44: CFD model with film cooling

Grid Convergence Study

Two grid convergence studies were performed for the baseline and film cooling simulations respectively. Three grids were simulated as part of each grid convergence study. For the baseline case, the three grids included 6.75M, 9.93M, and 18.1M cells. The

convergence monitors in addition to the residuals included the mainstream mass flow rate, total pressure and average static pressure on the endwall. The total pressure and mass flow rate were monitored at multiple flow-normal planes inside the CFD model. Table 7 shows the order of magnitude of the residuals after convergence. The pressure coefficient distribution on the endwall at the inlet was compared between the three grids. The results showed an average difference of < 1% between the medium and fine grid computations. In order to ensure that the results do not change significantly between $y^+ < 3.5$ and $y^+ < 1$ grids, a computation was performed with the fine grid (18.1 M) with $y^+ < 1$. The results showed < 1.5% difference between $y^+ < 3.5$ and $y^+ < 1$ grids. The results reported are for the fine grid computations with $y^+ < 3.5$.

In the case of film cooling simulations, the three grids included 7.2M, 12.2M, and 20.1M cells. The convergence monitors in addition to the residuals included mainstream and coolant mass flow rate, coolant plenum total pressure and the average static temperature on the film cooling coupon. Table 7 shows the order of magnitude of the residuals after convergence. An average blowing ratio of 0.83 was used for the grid study as a representative case. The results exhibited a maximum difference of < 3.2% between the medium and fine grid computations. In order to ensure that the results do not change significantly between $y^+ < 3.5$ and $y^+ < 1$ grids, a computation was performed for M_{avg} = 0.83 (as a representative blowing ratio) with the medium grid (12.2 M) with $y^+ < 1$. The results showed < 1% difference between $y^+ < 3.5$ and $y^+ < 1$ grids. The results reported in this paper are for the medium grid computations with $y^+ < 3.5$. Figure 45 shows the medium grid CFD model used for the film cooling computations.

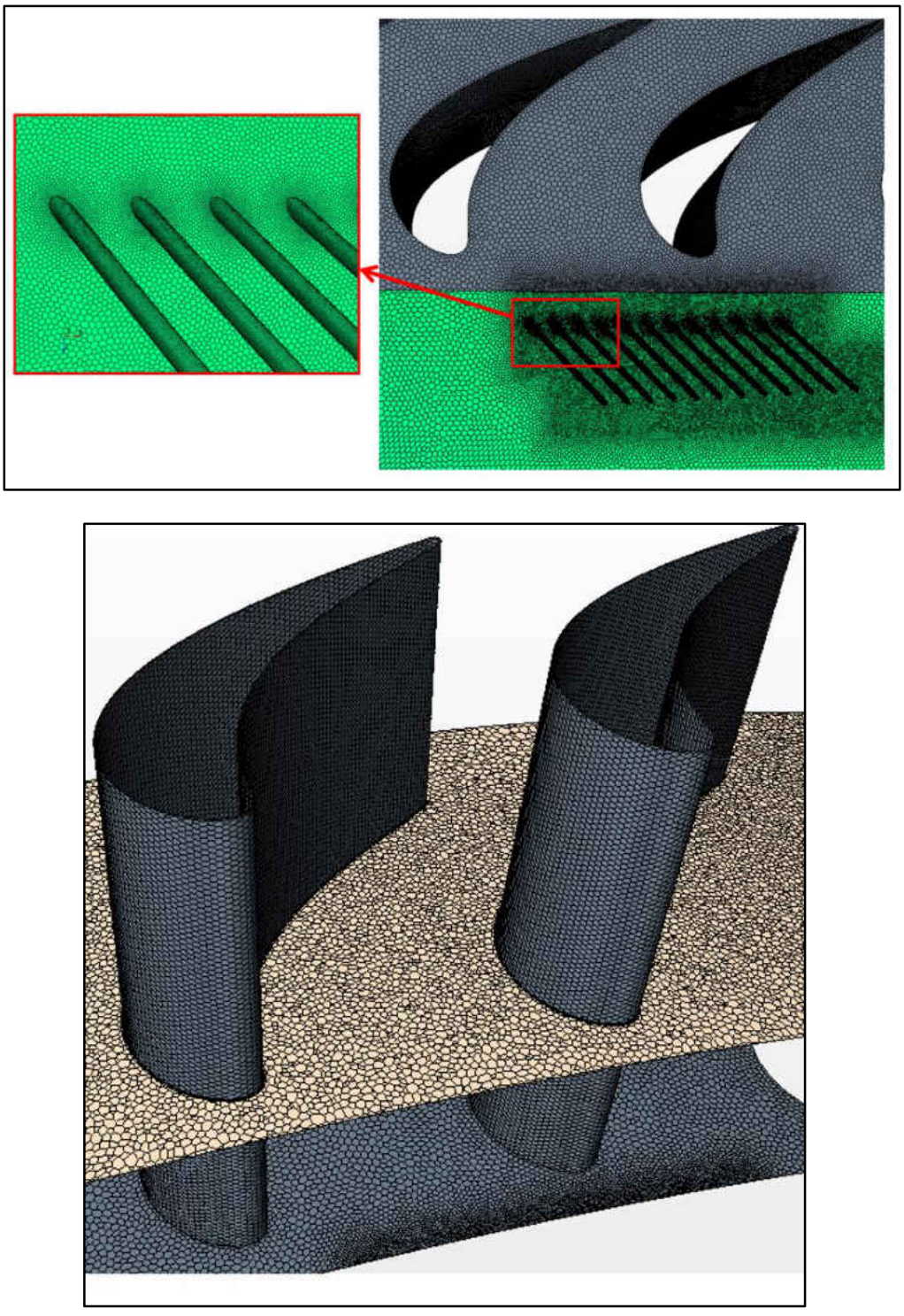

Figure 45: Medium grid CFD model

Table 7: Order of magnitude of residuals after convergence

Governing equation	Residual
Continuity	$< 10^{-4}$
x-momentum	$< 10^{-4}$
y-momentum	$< 10^{-4}$
z-momentum	$< 10^{-4}$
Energy	$\cong 10^{-3}$
Turbulent kinetic energy	$\cong 10^{-3}$
Turbulent dissipation rate	$\cong 10^{-3}$

Computational Solver and Turbulence Model

All computations were performed using StarCCM+ v10.02.012 [2]. The compressible Reynolds-Averaged Navier Stokes (RANS) solver with a second order coupled-energy formulation was used for the fluid domain. The realizable k-ε turbulence model was used for turbulence closure. A study by Davis et al. [3] showed that the realizable k-ε turbulence model performs better than other RANS-based turbulence models in flows with three-dimensional flow separation. The default coefficients were used with the realizable k-ε turbulence model and can be found in [2]. The film cooling simulations included the plexiglass film cooling coupon which was modeled as a solid continuum. A constant density coupled-energy solver was used for the solid continuum

Numerical Uncertainty

The CFD uncertainty in the coolant temperature drop across the film cooling hole was calculated according to the numerical accuracy procedure reported by Celik et al. [4]. Since the difference between the coolant mass flow rate values of the medium and fine grid

computations was very close to zero, the numerical accuracy procedure reported by [4] could not be used. Due to this constraint, an alternative method was used to calculate the CFD uncertainty. The average percentage difference of the fractional coolant mass flow rate between the medium and fine grid results was used to estimate the uncertainty in the discharge coefficient and the fractional coolant mass flow rate. The grid convergence index (GCI) for the coolant temperature drop and the fractional coolant mass flow rate for the different grids are given in Table 8 and Table 9 respectively.

Table 8: Grid convergence index for the coolant temperature drop

Grid no.	Grid size (in millions)	$(T_{c,i} - T_{c,e})/(T_{c,i} - T_{\infty})$	GCI_{32} (%)	GCI_{21} (%)
3	7.2	0.122	0.15	0.08
2	12.2	0.135		
1	20.1	0.14		

Table 9: Comparison of percentage coolant flow rate between grids

FCH no.	$\dot{m}_h/\dot{m}_{c,tot}$			% $Difference_{21}$
	7.2M	12.2M	20.1M	
1	8.185	8.188	8.200	0.150
2	8.284	8.286	8.277	0.112
3	8.412	8.392	8.387	0.056
4	8.533	8.504	8.479	0.302
5	8.603	8.555	8.540	0.177
6	8.604	8.561	8.552	0.107
7	8.537	8.499	8.489	0.118
8	8.376	8.368	8.371	0.038
9	8.195	8.233	8.240	0.081
10	8.080	8.143	8.147	0.040
11	8.067	8.113	8.136	0.289
12	8.125	8.156	8.181	0.307

Based on average percentage difference between the medium and fine grid values of $\dot{m}_h/\dot{m}_{c,tot}$ in Table 9, the uncertainty in the discharge coefficient and fractional coolant mass flow rate was calculated to be ≅ ±0.28% and ±0.15% respectively.

Validation of CFD model

The CFD model validation with experimental data for the airfoil passage periodicity (extracted at x/Cax ≅ - 0.075) is shown in Figure 46. The CFD results appear to be in good agreement with the experimental data except at the peak negative pressure region near the airfoil suction side. One reason for this deviation can be due to the inaccurate prediction of the three-dimensional flow near the airfoil suction side by the turbulence model. More effort in CFD modeling is required for better prediction of flow near the leading-edge.

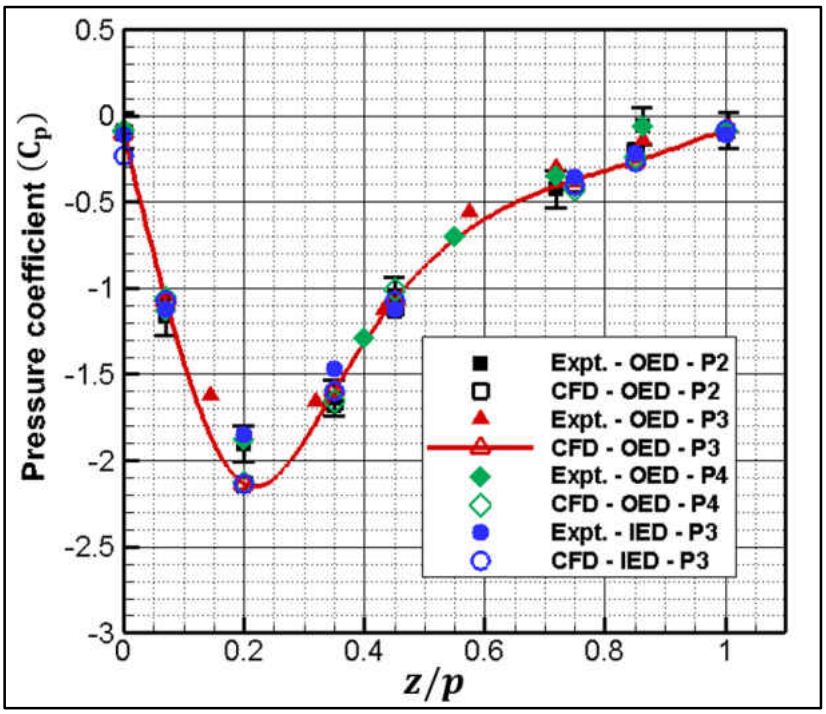

Figure 46: Validation of CFD model with experimental data

References

[1] Ansys Inc., 2013, “Ansys v15 documentation”, Canonsburg, Pennsylvania, USA

[2] CD Adapco, 2014, “StarCCM+ v10.02 documentation”, Melville, New York, USA

[3] Davis, P. L., Rinehimer, A. T., and Uddin, M., 2012, “A comparison of RANS-based turbulence modeling for flow over a wall-mounted square cylinder”, Proceedings of 20th Annual Conference of the CFD Society of Canada.

[4] Celik, I., Chen, C.J., Roache, P.J. and Scheurer, G., Eds., 1993, “Quantification of Uncertainty in Computational Fluid Dynamics,” *ASME Publ. No. FED-158*, ASME Fluids Engineering Division Summer Meeting.

CHAPTER 9: RESULTS AND DISCUSSION

Unsteady Passing Wake Effect on a Pitchwise-curved Surface

In order to validate the unsteady passing wake study for steady mainstream flow conditions, flat plate experiments with similar test parameters and film hole geometry were selected from the open literature for pitch-averaged and centerline heat transfer augmentation measurements. Since blowing ratio is not the only scaling parameter for describing film cooling performance, research studies with similar momentum flux ratios were also included in the experimental validation.

At this juncture, it is essential to point out the influence of an important non-dimensional parameter on heat transfer in the presence of film cooling. The ratio of displacement thickness to the film hole diameter (δ_1/D) provides the thickness of the incoming boundary layer relative to the film hole diameter. Depending on the boundary layer thickness at the film injection location, the value of δ_1/D can change significantly.

In connection with heat transfer, an increased boundary layer thickness offers a greater resistance to heat conduction near the wall compared to a thin boundary layer. A low momentum film jet thickens the boundary layer at the film injection location thereby adding to the near wall heat conduction resistance. On the other hand, a high momentum film jet penetrates into the boundary layer at the film injection location promoting turbulent mixing of the two fluid streams which enhances the heat transfer coefficient.

Pitch-averaged heat transfer augmentation

When comparing the different coolant to mainstream mass flux ratios for the baseline case (S = 0), it can be seen that the pitch-averaged heat transfer augmentation increases with the blowing ratio (Figure 47). The maximum increase in the pitch-averaged heat transfer augmentation is approximately 8%, 15%, and 20.5% for M = 0.25, 0.5, and 0.75 respectively. For all the blowing ratios presented, the maximum increase in the pitch-averaged heat transfer augmentation occurs at x/D ≅ 0.9. It is worthwhile to mention here that the increase in heat transfer augmentation can be even higher at x/D < 0.9 since the region near film injection location experiences significant mixing between the coolant and the mainstream. A monotonically decreasing trend in the pitch-averaged heat transfer augmentation is seen for all the three blowing ratios with increasing streamwise distance from the film cooling hole.

Table 10 shows the pertinent parameters used for comparison between the present study and the published literature. Comparison between the case of M = 0.5 in the present study and Hay et al. [1] shows quantitative agreement at most of the streamwise locations (Figure 48). On the other hand, there is a significant difference when compared to the results reported by Eriksen and Goldstein [2] for a similar mass and momentum flux ratio. One reason for this could be a small δ_1/D value near the film injection location of [2]. The heat transfer in the case of Eriksen and Goldstein [2] could have been higher without film injection than with film jets at low momentum flux ratios leading to a heat transfer augmentation less than unity.

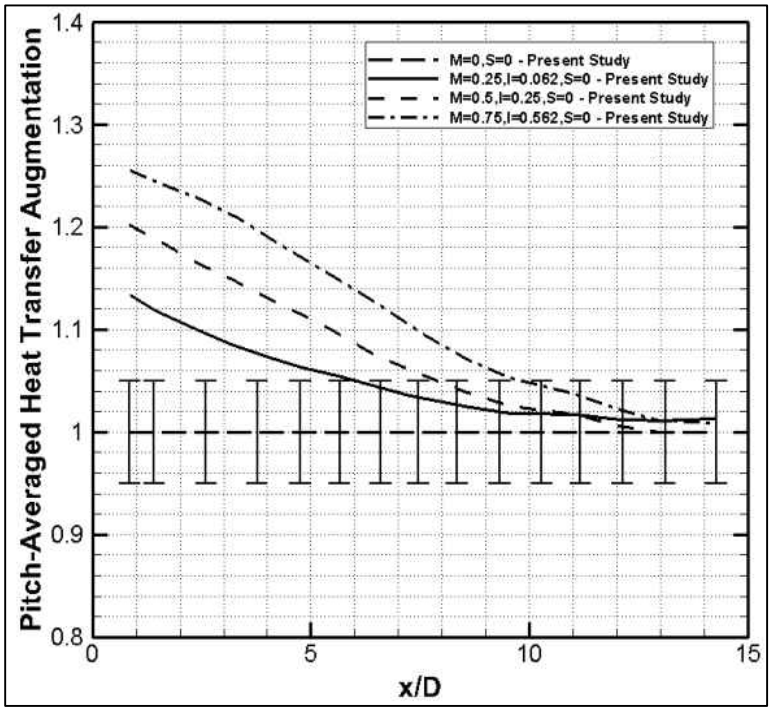

Figure 47: Pitch-averaged heat transfer augmentation - S = 0

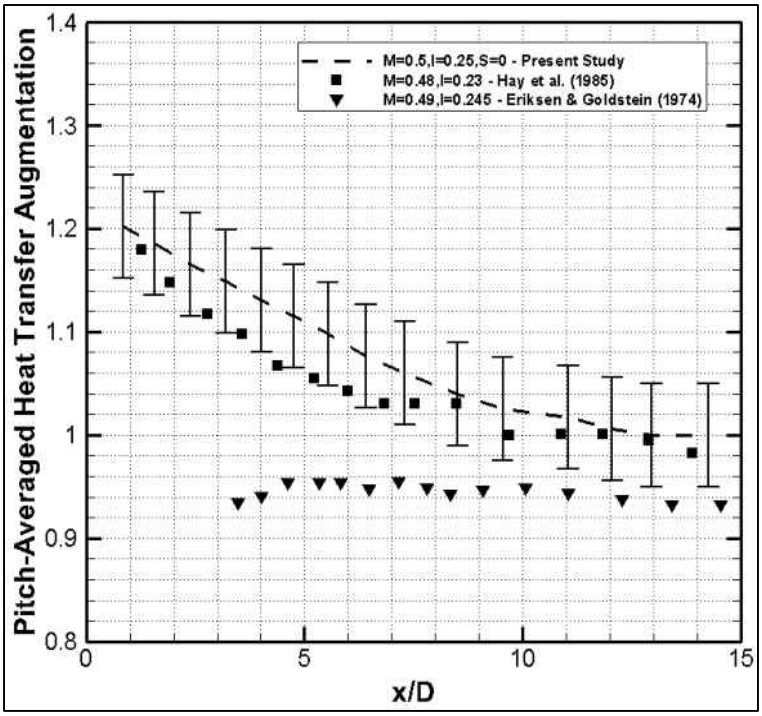

Figure 48: Literature comparison for pitch-averaged heat transfer augmentation - S = 0

Table 10: Parameters for comparison with published literature

Author(s)	Parameters used for comparison in unsteady wake study								
	M	DR	I	D (mm)	L/D	p/D	α	δ_1/D	% Tu
Present study	0.25	1	0.062	8	8	3	35˚	0.32	1.5
	0.5		0.25						
	0.75		0.562						
Hay et al. [1]	0.48	1	0.23	2.3	> 4	3	35˚	0.63	low
Yuen & Botas [4]	0.5	1	0.25	NA	4	Single hole	30˚	0.15	2.7
Eriksen & Goldstein [2]	0.49	0.98	0.24	11.8	> 4	3	35˚	0.06-0.12	0.5

The effect of unsteady passing wakes on the pitch-averaged heat transfer augmentation is shown in Figures 49-50. At S = 0.15 (Figure 49), there is negligible influence from the passing wake for the no film injection case (M = 0). The introduction of the film jets combined with the passing wakes produce a maximum heat transfer augmentation of ≅ 10.4%, 17.7%, and 24.3% for M = 0.25, M = 0.5, and M = 0.75 respectively. Comparing the above values with the results without the passing wakes (Figure 47), it can be seen that the contribution from the passing wakes towards heat transfer augmentation is ≅ 2.4%, 2.7%, and 3.8% for M = 0.25, M = 0.5, and M = 0.75 respectively.

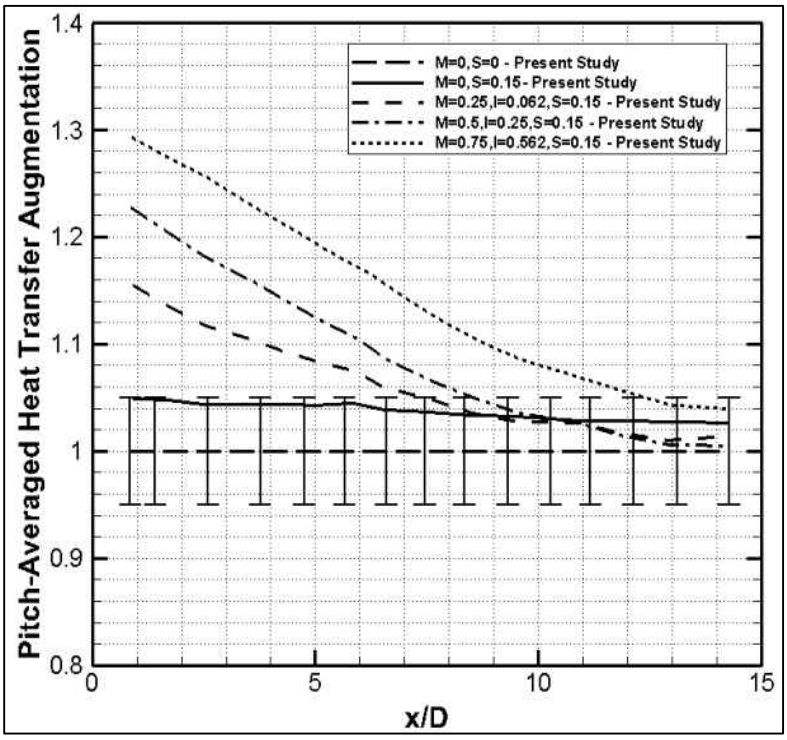

Figure 49: Pitch-averaged heat transfer augmentation - S = 0.15

Increasing the wake passing frequency enhances the heat transfer as shown in Figure 50. For the no film injection case, the passing wakes escalate the heat transfer by ≅ 6% relative to the baseline case (M = 0, S = 0). For the film injection cases (M = 0.25, 0.5, 0.75), the increase in heat transfer is ≅ 16%, 23%, and 28% respectively. The individual contribution of the passing wakes at S = 0.3 is ≅ 8% for M = 0.25, 0.5 and ≅ 7.5% for M = 0.75.

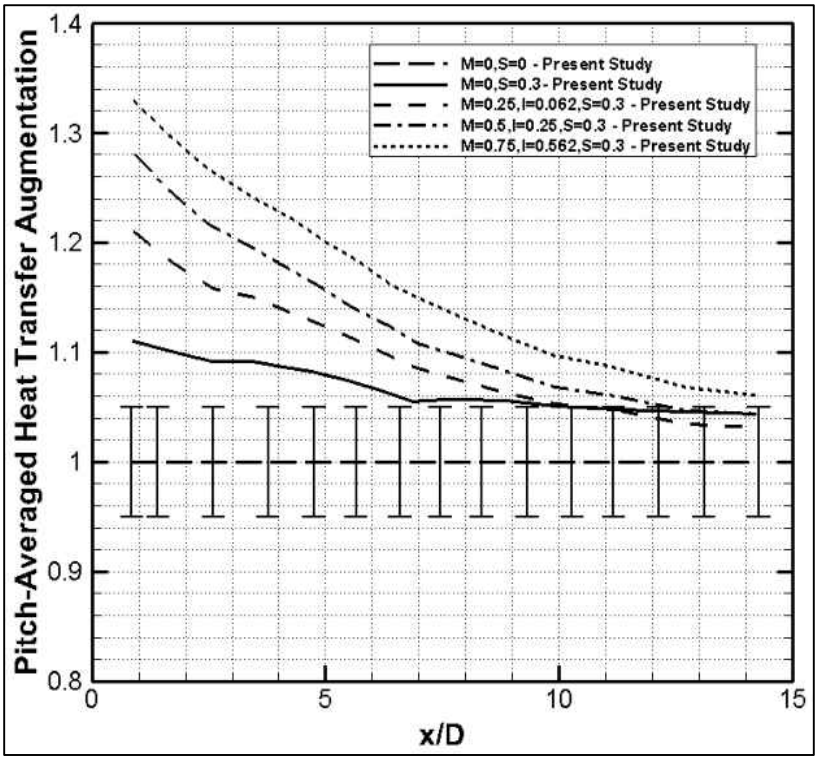

Figure 50: Pitch-averaged heat transfer augmentation - S = 0.3

Centerline Heat Transfer Augmentation

Figure 51 shows the baseline case (S = 0) of the centerline heat transfer augmentation for the present study. Increasing the jet momentum enhances the interaction between the film jet and the mainstream by mixing. Apart from this, at higher blowing ratios, the analogy of flow past a cylindrical rod can be used to explain the jet-mainstream interaction [3]. Although this creates a wake region under the film jet in the immediate vicinity of injection, it also increases the velocity fluctuations in this region. As the velocity fluctuations propagate along the streamwise and pitchwise directions, they increase the shear stress near the wall by altering the velocity gradient. This phenomenon eventually results in an increased heat transfer coefficient. Quantitatively, the maximum enhancement

in the heat transfer coefficient is ≅ 7.9%, 15.5%, and 24.3% for M = 0.25, M = 0.5, and M = 0.75 respectively. When comparing with the baseline case of the pitch-averaged heat transfer augmentation, the effect of film cooling on the heat transfer coefficient is similar between the centerline and pitch-averaged heat transfer augmentation with a slightly higher (≅ 3.8%) heat transfer augmentation for M = 0.75 at the film jet centerline.

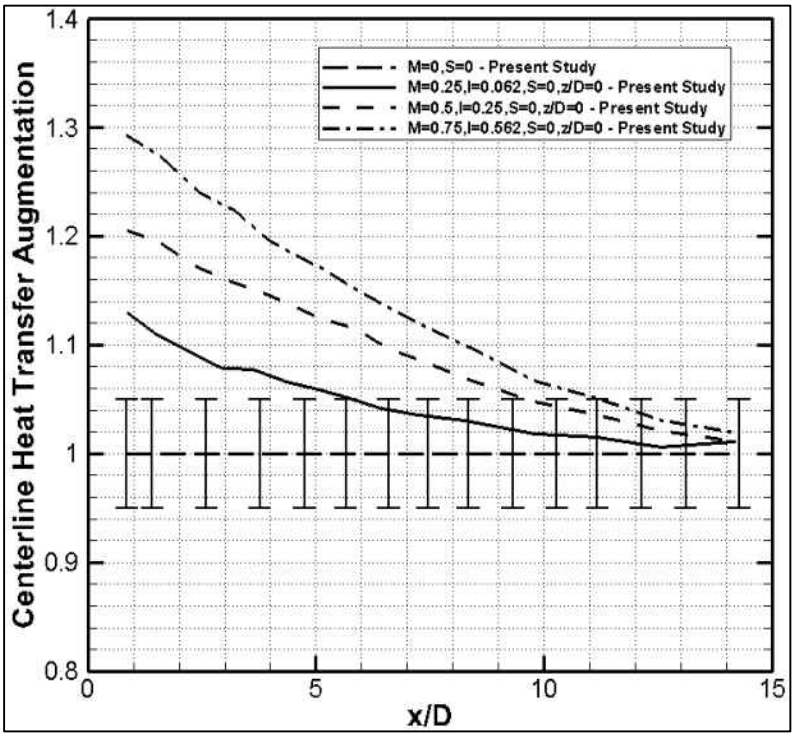

Figure 51: Centerline heat transfer augmentation - S = 0

In comparison with published literature (Figure 52) the centerline augmentation (M = 0.5) shows quantitative agreement with Hay et al. [1] till x/D ≅ 3.5 and past x/D ≅ 7 with Yuen and Botas [4]. Both the aforementioned studies have a significant difference in the displacement thickness to film hole diameter ratio as shown in Table 10. At the near hole region, the jet-to-mainstream interaction is significant which overrides the increase in

displacement thickness due to film injection at lower blowing ratios. With increasing streamwise distance, the displacement thickness becomes important as the heat transfer augmentation approaches unity in the case of the present study. In case of Hay et al. [1], the heat transfer augmentation falls below unity for x/D > 6. One reason for this could be the rise in near wall heat conduction resistance compared to the no film injection case.

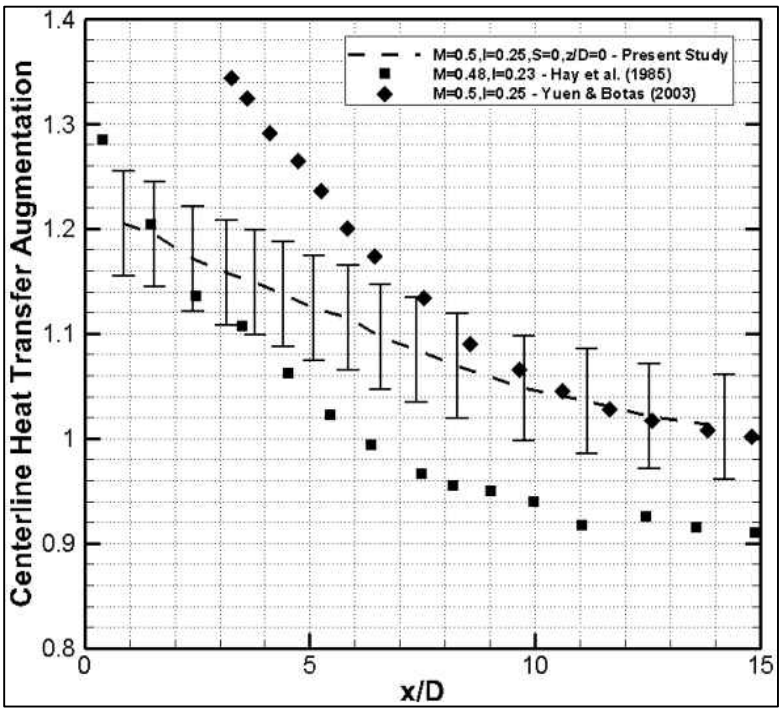

Figure 52: Literature comparison for centerline heat transfer augmentation - S = 0

With the introduction of passing wakes, there is a considerable impact on the centerline heat transfer coefficient. The passing wake is a low velocity fluid packet with increased unsteadiness. As it convects along the test surface, it acts on the film jets by mixing with them. When this happens, the film jets acquire part of the velocity fluctuations present in the passing wake which may be significant based on the film jet's momentum flux relative to the mainstream at the injection location. The passing wake-induced velocity

perturbations are one of the primary contributors towards the increased heat transfer augmentation.

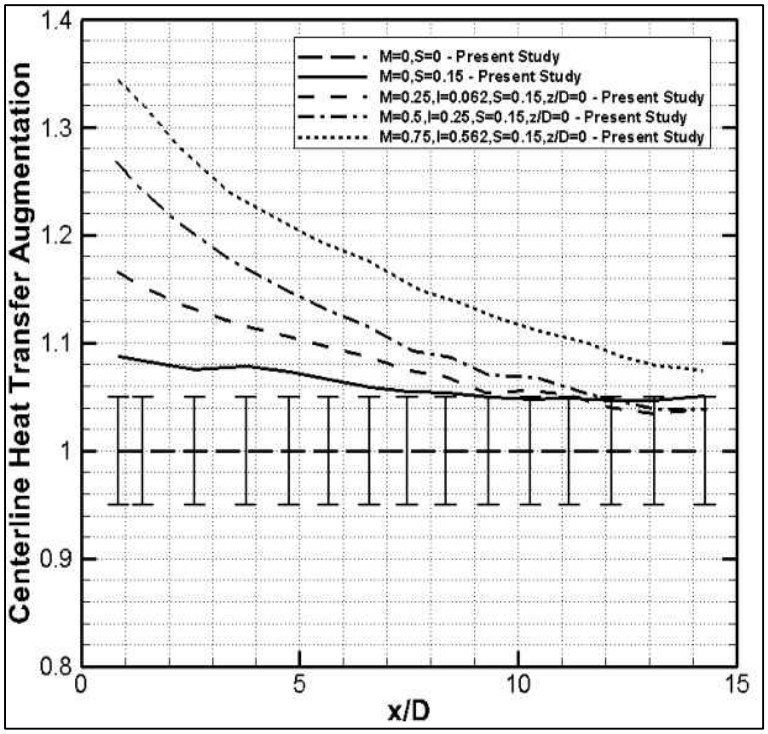

Figure 53: Centerline heat transfer augmentation - S = 0.15

For the low wake passing frequency (S = 0.15), an approximate increase of 11.6%, 21.7%, and 28.3% can observed for M = 0.25, M = 0.5, and M = 0.75 respectively (Figure 53). It is important to note that the maximum heat transfer augmentation with only the passing wakes is ≅ 3.7%. The contribution of the passing wakes towards heat transfer augmentation in addition to the film injection is 3.7%, 6.1%, and 4.7% (approximately) at M = 0.25, M = 0.5, and M = 0.75 respectively. At increased downstream locations, the heat transfer augmentation values decline monotonically to unity with the decay rate proportional to the coolant to mainstream mass flux ratio.

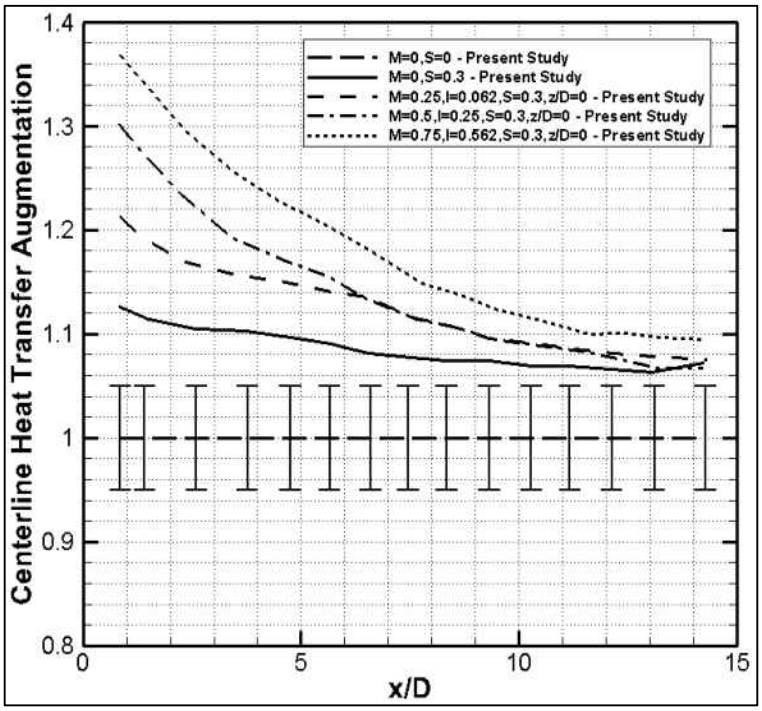

Figure 54: Centerline heat transfer augmentation - S = 0.3

At an elevated wake passing frequency (S = 0.3), the centerline heat transfer augmentation increases even further as shown in Figure 54. The approximate increase in the heat transfer augmentation is ≅ 7.6%, 16.3%, 25%, and 31.7% for M = 0, M = 0.25, M = 0.5, and M = 0.75 respectively. Compared to low wake passing frequency case, the maximum heat transfer augmentation with only the passing wakes exhibited an additional increase of ≅ 4%. This increase clearly signifies the amplification in the wake velocity perturbations which cause vigorous mixing with the film jets. With regard to the sole contribution of the passing wakes towards heat transfer augmentation in addition to the film injection, an increase of 8.3%, 9.4%, and 8.1% (approximately) is observed at M = 0.25, M = 0.5, and M = 0.75 respectively. The heat transfer augmentation decay trend with increased streamwise distance is similar to S = 0.15.

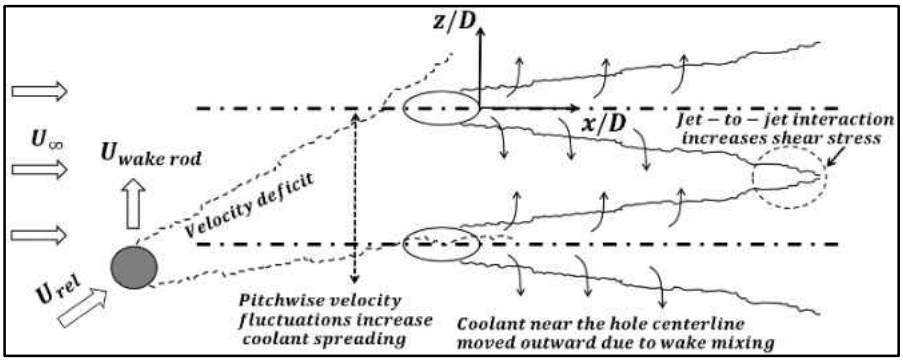

Figure 55: Simplified schematic of unsteady passing wake effect on film cooling

As seen in Figure 55, locations away from the film jet centerline experience shear layer interaction between adjacent film jets leading to continuous perturbation of the near wall velocity gradients. To better understand the effect of the jet-to-jet interaction and the wake influence, the centerline between two film holes (z/D = 1.5) was chosen in addition to the jet centerline to compare the differences. Figure 56 shows such a comparison for the no wake case.

It is evident that there is insignificant difference in the heat transfer augmentation between z/D = 0 and z/D = 1.5 for M = 0.25 and 0.5. At M = 0.75, there is an increase in the heat transfer augmentation at z/D = 1.5 (compared to z/D = 0) between x/D = 1.5 and x/D = 4.5 with the maximum increase (≅ 4.5%) measured at x/D ≅ 2.5. This rise in the heat transfer augmentation is conjectured to be due to the interaction between the film jets.

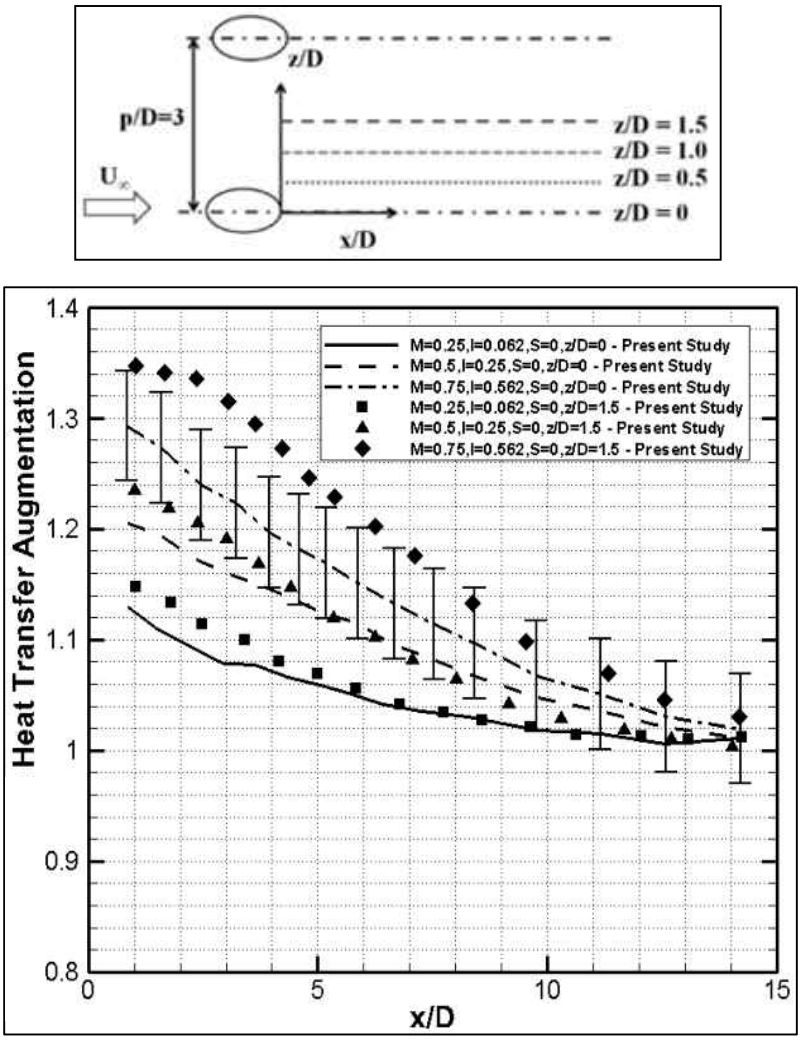

Figure 56: Centerline and off-centerline heat transfer augmentation - S = 0

At the low wake passing frequency (S = 0.15) shown in Figure 57, the variation between z/D = 0 and z/D = 1.5 decreases. No differentiation can be made for M = 0.25 and M = 0.5 between z/D = 0 and z/D = 1.5 whereas the increase in the heat transfer augmentation at the highest blowing ratio (M = 0.75) is ≅ 2.1% at x/D ≅ 3.2. At the highest wake passing frequency (S = 0.3) shown in Figure 58, the heat transfer enhancement occurs

between x/D = 4.5 and x/D = 8 at M = 0.5 and between x/D = 7 and x/D = 8.5 for M = 0.75. The maximum increase in the heat transfer augmentation is ≅ 2%.

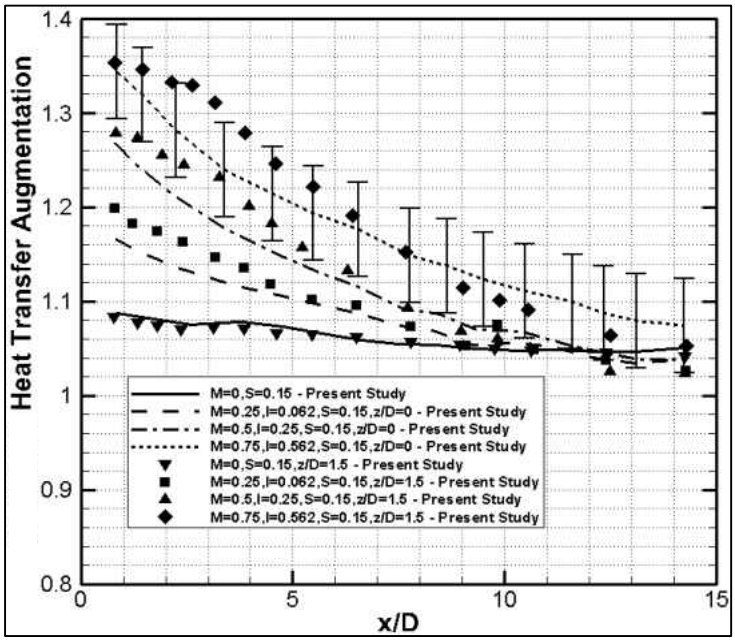

Figure 57: Centerline and off-centerline heat transfer augmentation - S = 0.15

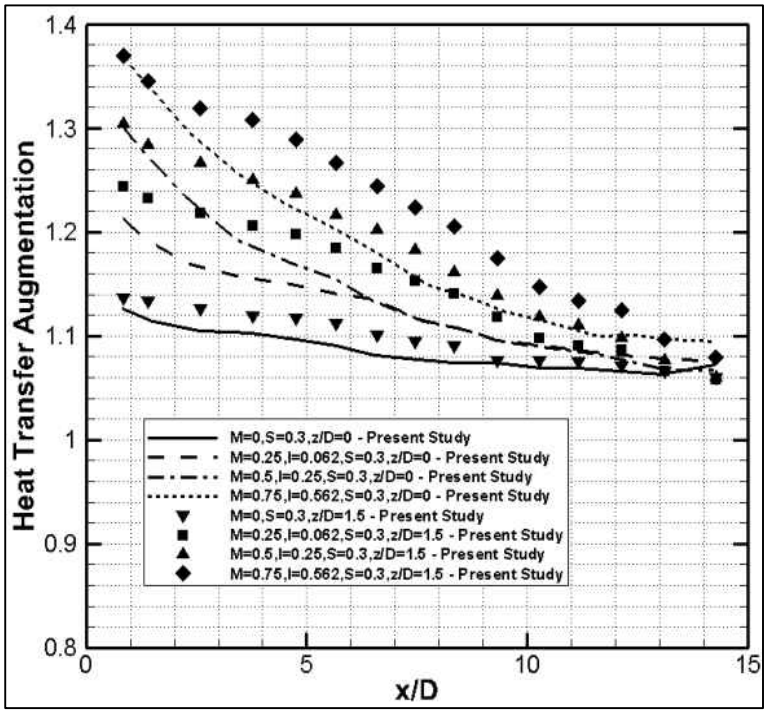

Figure 58: Centerline and off-centerline heat transfer augmentation - S = 0.3

Endwall Film Cooling in a High Subsonic Annular Cascade

Airfoil Passage Periodicity

The passage periodicity results along with the CFD model validation are shown in Figure 46 (chapter 8).

Coolant Temperature Drop across Film Cooling Hole

The predicted coolant temperature drop across the film cooling hole is provided in a normalized form in Figure 59. It is observed that the coolant temperature drop increases in a close to linear trend with blowing ratio. A maximum temperature drop of ≅ 9.34°C is noted at the highest blowing ratio. In the case of a real gas turbine, the coolant temperature increases as the coolant passes through the film cooling hole due to the heat convection from the wall of the film cooling hole to the fluid. This is often referred to as "heat pickup". It is essential to use the increased temperature of the coolant (i.e. at the exit of the film cooling hole) for the film cooling effectiveness calculations. This is analogous to accounting for the coolant temperature drop in the experiments of the present study.

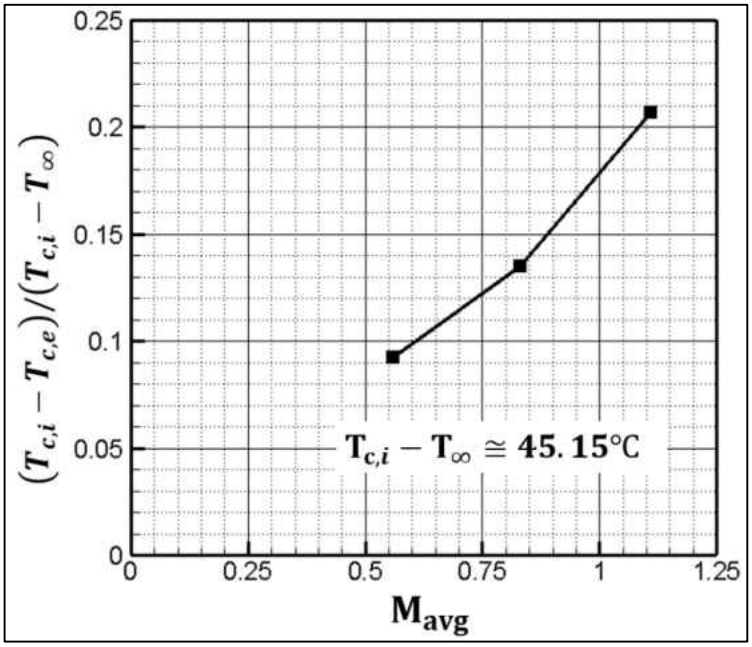

Figure 59: Predicted coolant temperature drop across film cooling hole

Endwall Surface Flow Visualization

A simplified representation of the pertinent vortex structures and the associated separation lines in the case of near-endwall flow are shown in Figure 60. The interaction between a non-uniform total pressure profile and the airfoil produces the horseshoe vortex at the airfoil leading-edge. Downstream of the leading-edge, the horseshoe vortex branches out into a pressure and a suction leg. The former is called the passage vortex (PV) and the latter is termed as the suction side horseshoe vortex (SHV). Due to the flow turning in the airfoil passage, a cross flow is generated from the pressure side to the suction side of the airfoil which contributes to the PV growth. This was reported earlier by Friedrichs [5]. The surface oil visualization was performed on the inner endwall of passage-3. The surface oil visualization results shown in Figures 61-64 provide insight into the complicated flow separation that occurs in an airfoil passage from a surface flow perspective.

Some of the important surface flow features include the saddle point (SP), leading-edge horseshoe vortex (LHV), passage vortex (PV), and corner vortex (CV). The saddle point is the location where the reversed flow at the leading-edge meets the oncoming mainstream flow. It was observed that film injection had a significant impact on the three-dimensional flow separation location as also reported by Friedrichs [5]. The saddle point location in the baseline case ($M_{avg} = 0$) shown in Figure 61 is used as a reference to quantify the saddle point shift in the film injection cases shown in Figures 62-64.

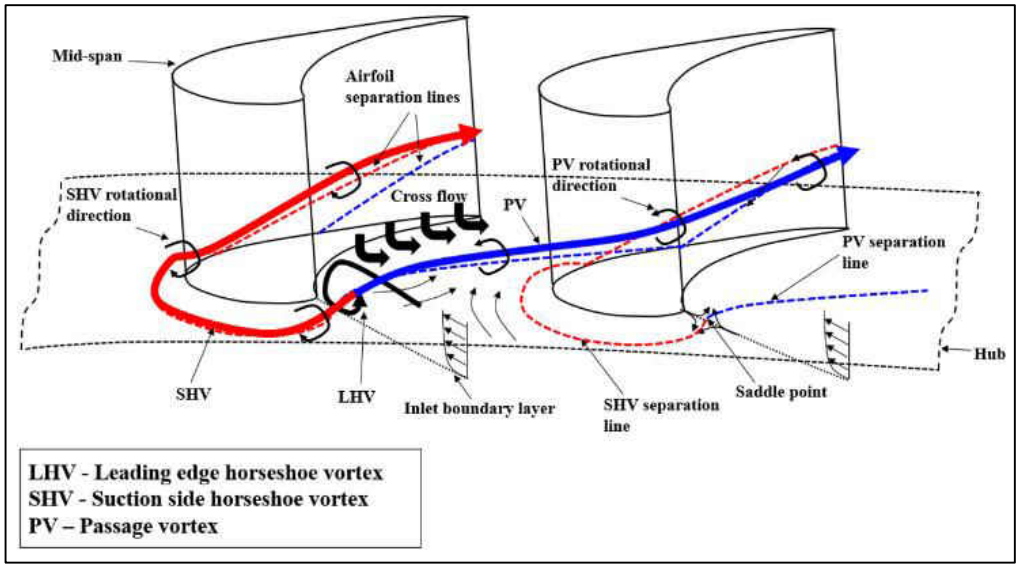

Figure 60: Simplified schematic of an endwall secondary flow system [6,7]

In order to quantify the influence of film injection on the endwall secondary flow, the location of the saddle point from the airfoil leading-edge is plotted as a function of the average blowing ratio in Figure 65, in which D_{LE} is the airfoil leading-edge diameter. For average blowing ratios between 0.56 and 1.11, the saddle point exhibits a movement towards the airfoil leading-edge. The highest shift in the saddle point is noticed at $M_{avg} = 1.11$ relative to the no film injection case.

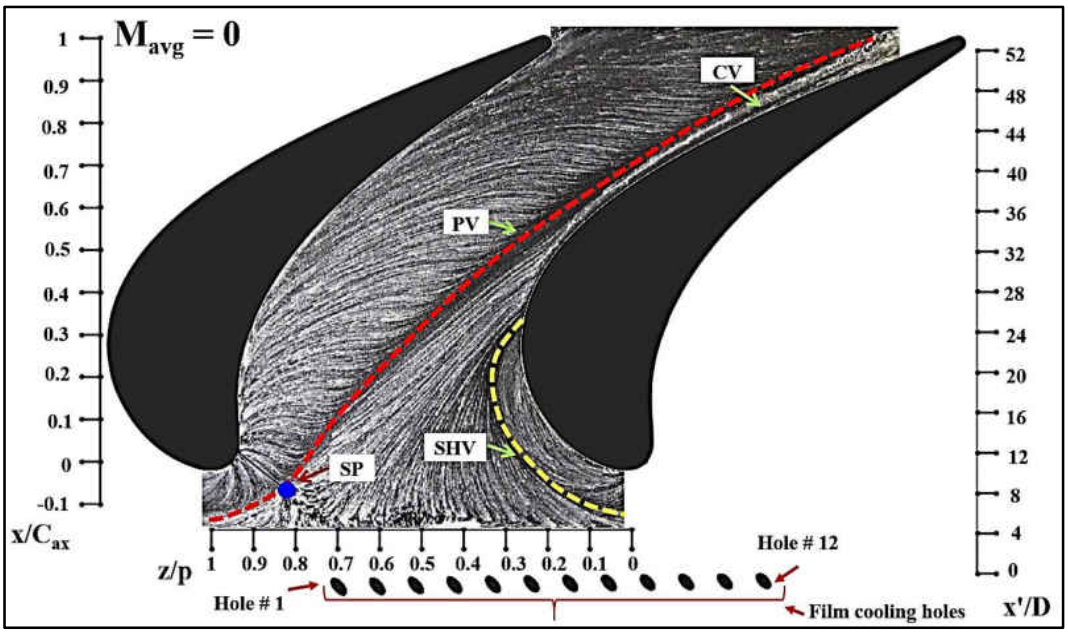

Figure 61: Endwall surface flow visualization without film injection

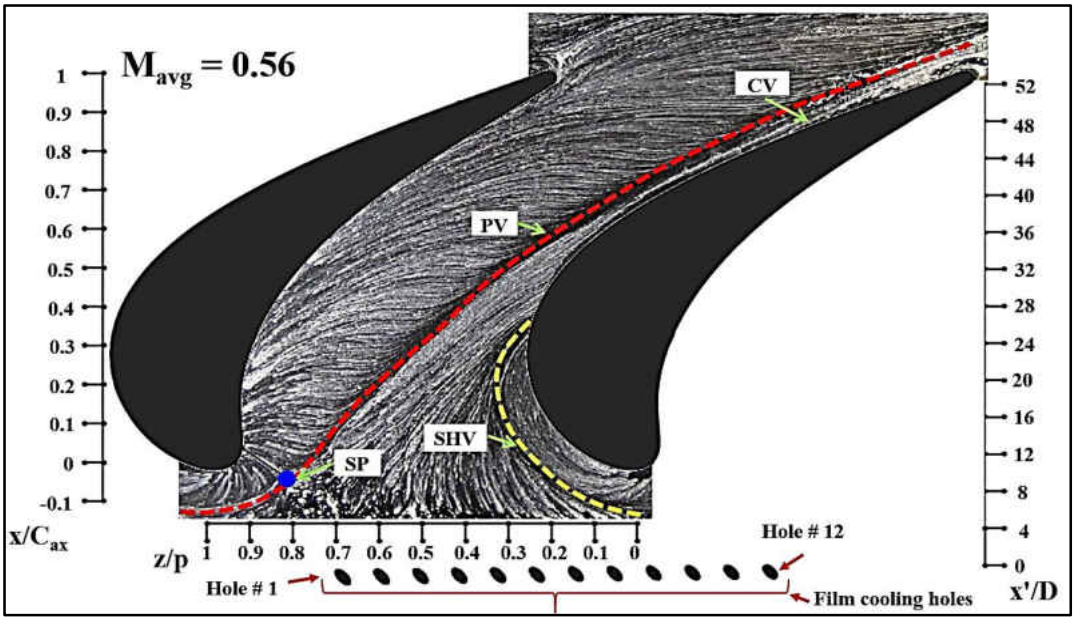

Figure 62: Endwall surface flow visualization with film injection - case 1

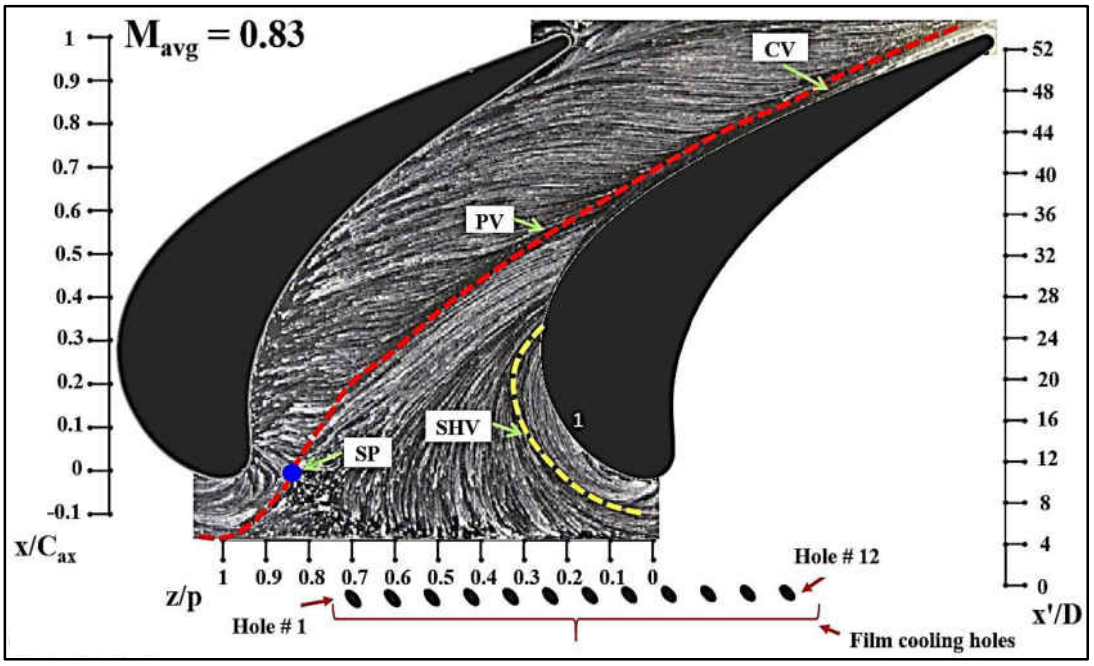

Figure 63: Endwall surface flow visualization with film injection - case 2

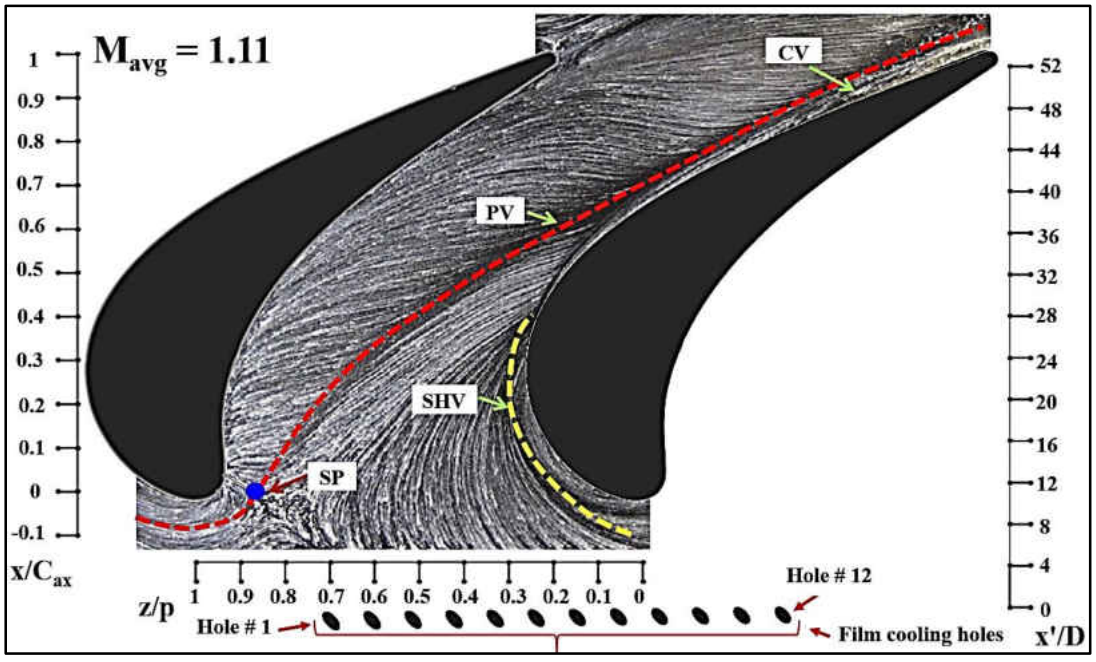

Figure 64: Endwall surface flow visualization with film injection - case 3

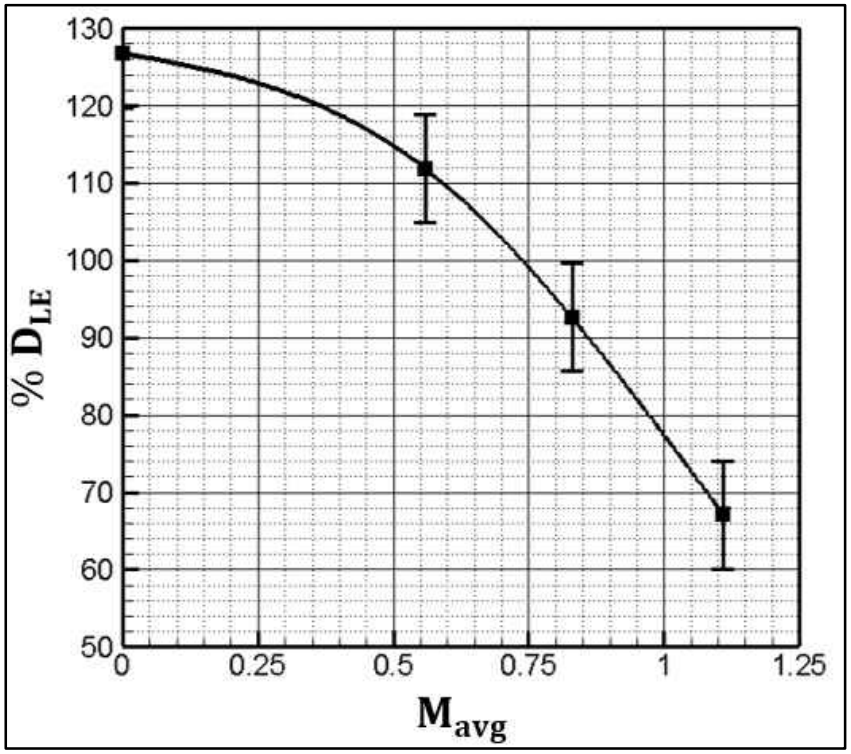

Figure 65: Location of saddle point with and without film injection

One of the main reason for the shift in the saddle point is due to the increased momentum flux of the film jet that provides the strength to penetrate into the mainstream flow near the airfoil-endwall junction. In addition to this, the separation lines move closer to the airfoil with increasing blowing ratio indicating that the injected film is strongly influencing the horseshoe vortex location. This movement in the separation lines due to the coolant injection upstream of separation lines agrees with the findings of Friedrichs [5]. For M_{avg} = 0.56, 0.83, and 1.11, the saddle point exhibits a close to linear shift of ≅ 11.7%, 27%, and 47% respectively relative to M_{avg} = 0.

Typically, at blowing ratios greater than 1, the film cooling jets can lift-off the endwall due to the increased momentum flux as reported by Friedrichs et al. [8]. While the jet lift-off threshold is well-defined in flat plate studies [9], the location of the film cooling holes relative to the airfoil leading-edge and the strong influence of the endwall secondary flow on the injected coolant make it difficult to define a universal jet lift-off threshold for cascade film cooling studies. Comparing the average blowing ratios in the present study, it appears that at M_{avg} = 0.56,0.83,1.11 the coolant jet-2 stays close to the endwall near the airfoil leading-edge. It should be noted here that jet lift-off may have occurred at M_{avg} = 0.83,1.11, but the film cooling jets near the airfoil leading-edge are still acting towards moving the LHV closer to the airfoil leading-edge.

Film Cooling Effectiveness

Impact of Endwall Surface Flow on Film Cooling Effectiveness Distribution

The film cooling effectiveness contours superimposed on the endwall surface flow are shown in Figures 66-68. For M_{avg} = 0.56 (Figure 66), it is observed that the coolant film extent is bounded primarily by the PV and the SHV separation lines. The vortices, due to their rotational motion distort the coolant film on the endwall by transporting the coolant into the mainstream flow away from the endwall. The transported coolant mixes with the mainstream flow and is considered lost from the endwall cooling perspective.

As a result of the induced incidence effect near the airfoil leading-edge, jet-1 tends to turn away from the airfoil pressure side as shown in Figure 70. This reduces the effective number of film jets contributing to film cooling for a single airfoil passage. Thus, it is

essential to account for the induced incidence effect in cascade film cooling experiments so that the individual film cooling hole mass flow rate and the film cooling jet trajectory are representative of a single airfoil passage. In the present study, the jet influenced by the induced incidence effect (jet-1) was not eliminated from the film cooling configuration since the number of film cooling holes were based on one geometric airfoil pitch. The individual film cooling hole fractional mass flow rate, discharge coefficients, and blowing ratios are provided in Figures 92-94 so that the jet behavior can be analyzed thoroughly.

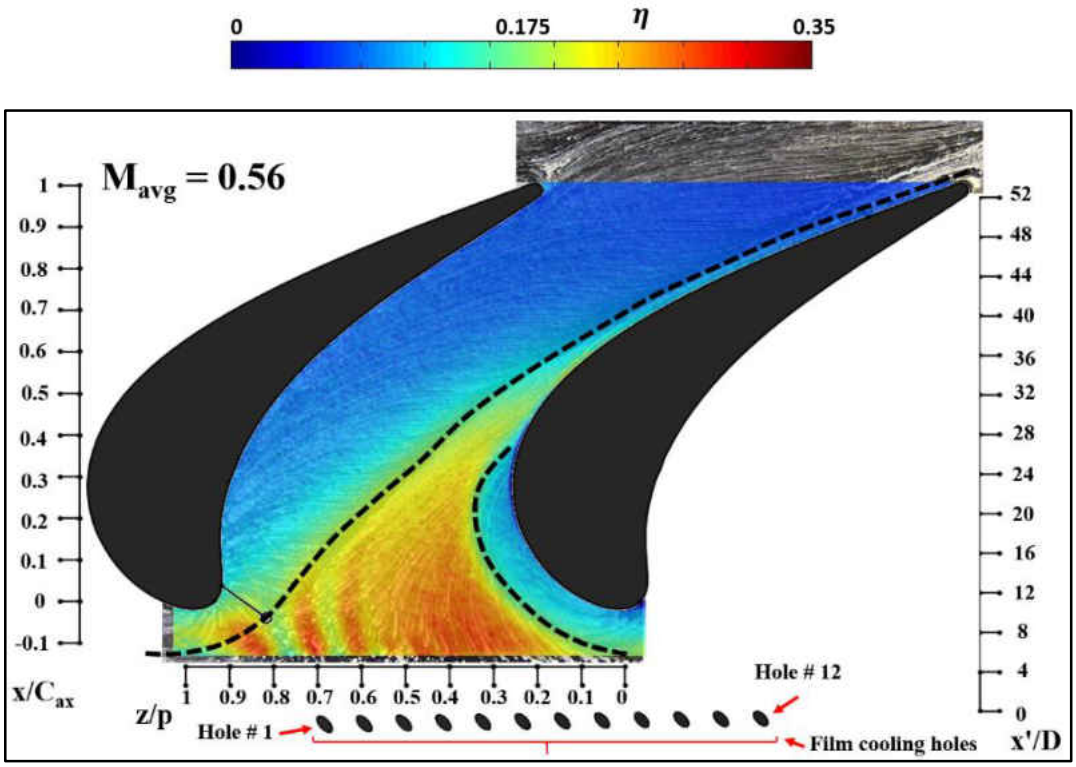

Figure 66: Film cooling effectiveness superimposed on surface flow - case 1

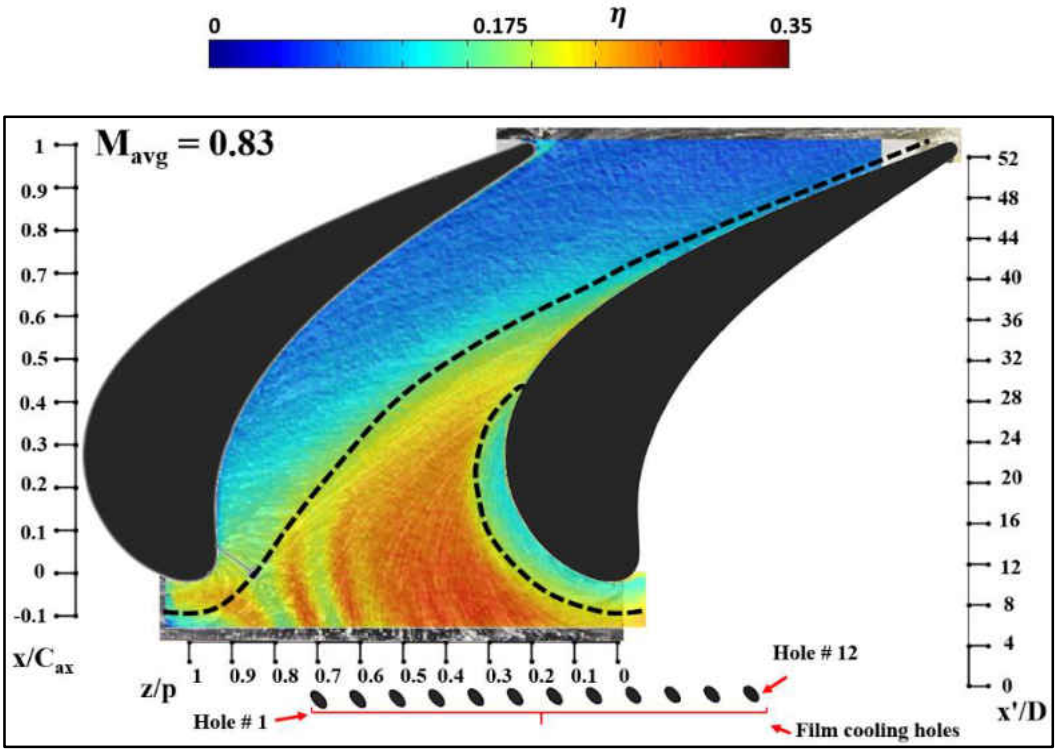

Figure 67: Film cooling effectiveness superimposed on surface flow - case 2

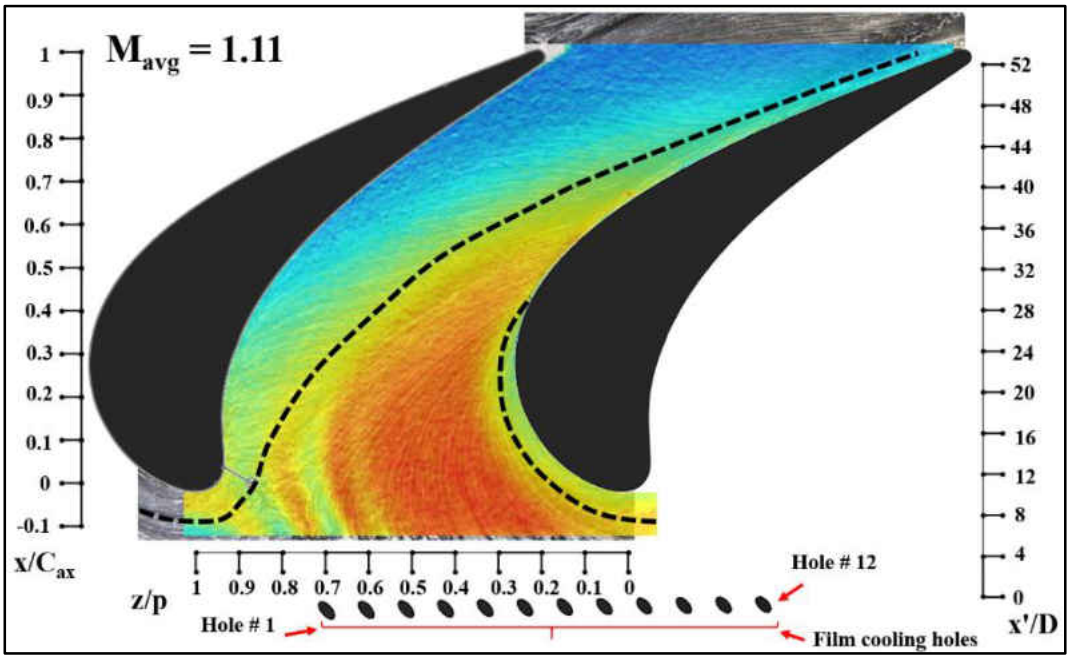

Figure 68: Film cooling effectiveness superimposed on surface flow - case 3

Comparing Figure 66 and Figure 70, it appears that film cooling jets 3-12 and the pressure side branch of jet-2 contribute completely towards film cooling in the studied passage. At $M_{avg} = 0.83$ (Figure 67), a reduction in the leading-edge separation zone occurs which provides increased coolant coverage. Similar to the lower blowing ratio case ($M_{avg} = 0.56$), majority of the coolant film is still bounded by the PV and SHV separation lines. There is slightly higher cooling near the airfoil leading-edge compared to $M_{avg} = 0.56$ which is due to the increased coolant momentum at $M_{avg} = 0.83$.

Increasing the blowing ratio above $M_{avg} = 0.83$ results in a significant coolant coverage compared to $M_{avg} = 0.56$. As inferred from the surface flow visualization results, the saddle point exhibits a shift of ≅ 47% for $M_{avg} = 1.11$. In addition, the SHV separation line has moved closer to the airfoil. This facilitates better cooling near the leading-edge, mid-pitch, and the suction side of the airfoil-endwall junction. Comparing with $M_{avg} = 0.83$, it can be seen from Figure 68 that the coolant jets-2,3 have lower film cooling effectiveness. This can be explained due to the increased momentum flux ratio ($I_{avg} = 1.38$) of the jets at $M_{avg} = 1.11$ which has resulted in jet lift-off.

Mainstream Flow and Coolant Jet Trajectory

From the CFD model, the streamlines for the mainstream flow and the coolant were obtained for $M_{avg} = 0$, $M_{avg} = 0.56$, and $M_{avg} = 1.11$ shown in Figures 69-75. This information is used to explain the secondary flow and coolant film interaction from a three-dimensional perspective. The locations of planes A,B,C,D,E shown in Figures 69-75 are for further analysis of the secondary flow and coolant film interaction discussed in the following section of this chapter. For the mainstream flow, the streamline seed is injected

at the inlet of the cascade section (≅ 2 mm from the inner endwall). In the case of coolant flow, the streamline seed is injected at a plane ≅ 1D upstream of the film cooling hole exit. The surface streamlines are visualized on a plane ≅ 2 mm from the inner endwall. The pressure and suction leg of the horseshoe vortex can be seen from Figure 69 for the baseline case. The pressure side leg of the horseshoe vortex, called the passage vortex meets the airfoil suction side at $x/C_{ax} \cong 0.5$ based on the surface flow pattern. By projecting the three-dimensional flow on the surface flow, it is observed that the PV and SHV lift-off along the surface flow separation lines.

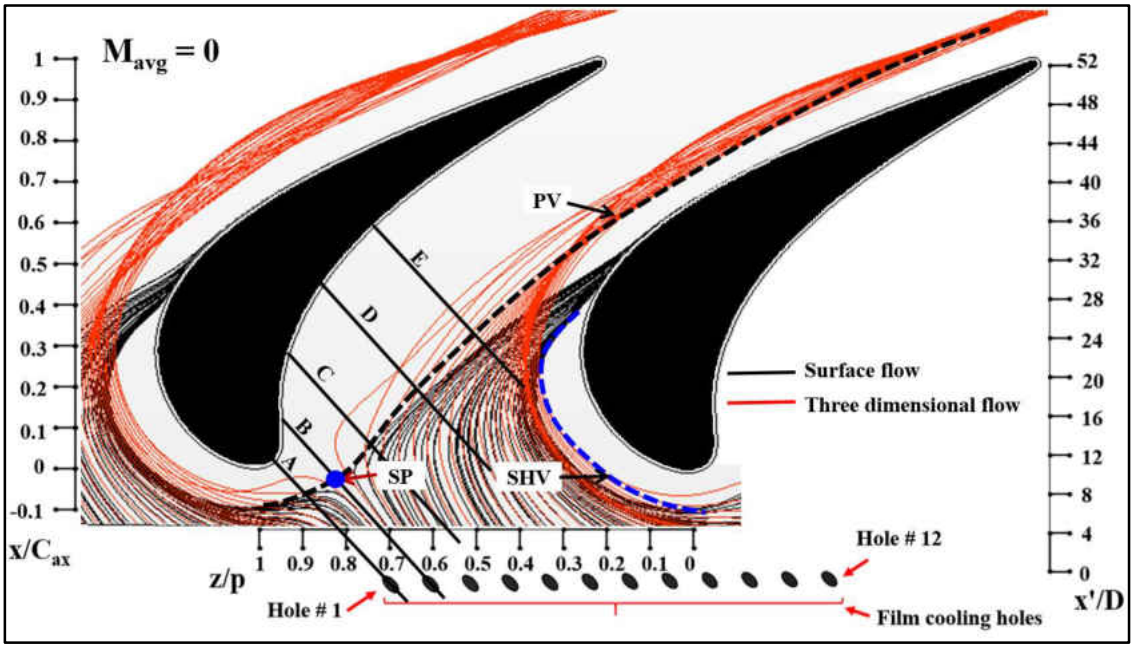

Figure 69: Predicted streamlines of mainstream flow without film injection

For the cases with film cooling, the coolant trajectory is superimposed on the three-dimensional mainstream flow to show the mixing of the coolant jets with the mainstream. Due to the complexity of the coolant-mainstream interaction, the coolant jets are split into 3 sets (4 holes each) to better explain the flow physics. In Figure 70, set-I of the film cooling

jets are shown along with the three-dimensional mainstream flow. Due to the induced incidence effect, jet-1 moves completely into the adjacent airfoil passage. The trajectory of jet-2 shows two vortex branches near the airfoil leading-edge. The suction side branch merges with the SHV of the adjacent passage. The pressure side branch exhibits a strong rotational motion and convects downstream merging with the passage vortex. As the film cooling jets-3,4 convect downstream, they are entrained into the passage vortex at $x'/D \cong 18$ and $x'/D \cong 24$ respectively.

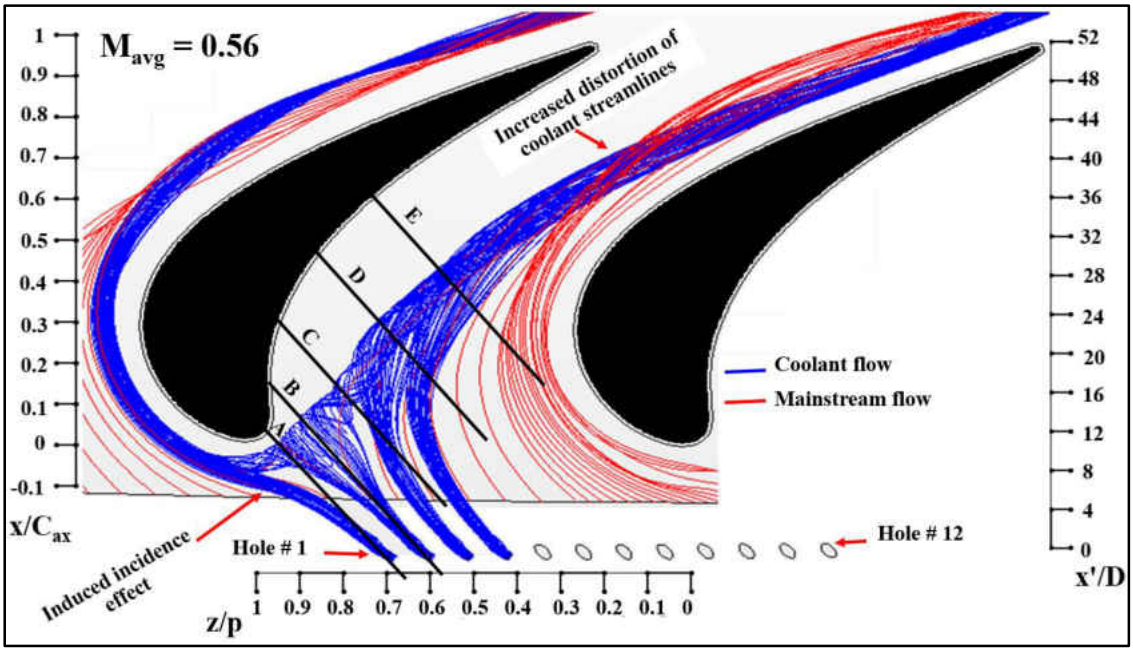

Figure 70: Predicted streamlines of mainstream and coolant flow - case 1a

The set-II of film cooling jets comprising jets 5-8 are shown in Figure 71. These jets have the least influence from the PV and SHV and hence persist for a longer distance downstream of the film injection location before getting entrained into the PV. Relating this information with Figure 66, it is noted that the film cooling effectiveness is significant for an increased downstream region of jets 5-8. Figure 72 shows the coolant trajectory for

jets 9-12. It is seen that jet-12 exhibits increased turning due to the induced incidence effect of the adjacent airfoil passage. The jets 9-12 remain close to the airfoil suction side as they move downstream. The local blowing ratios of these jets are higher compared to jets 5-8 and hence the jets are more susceptible to lift-off.

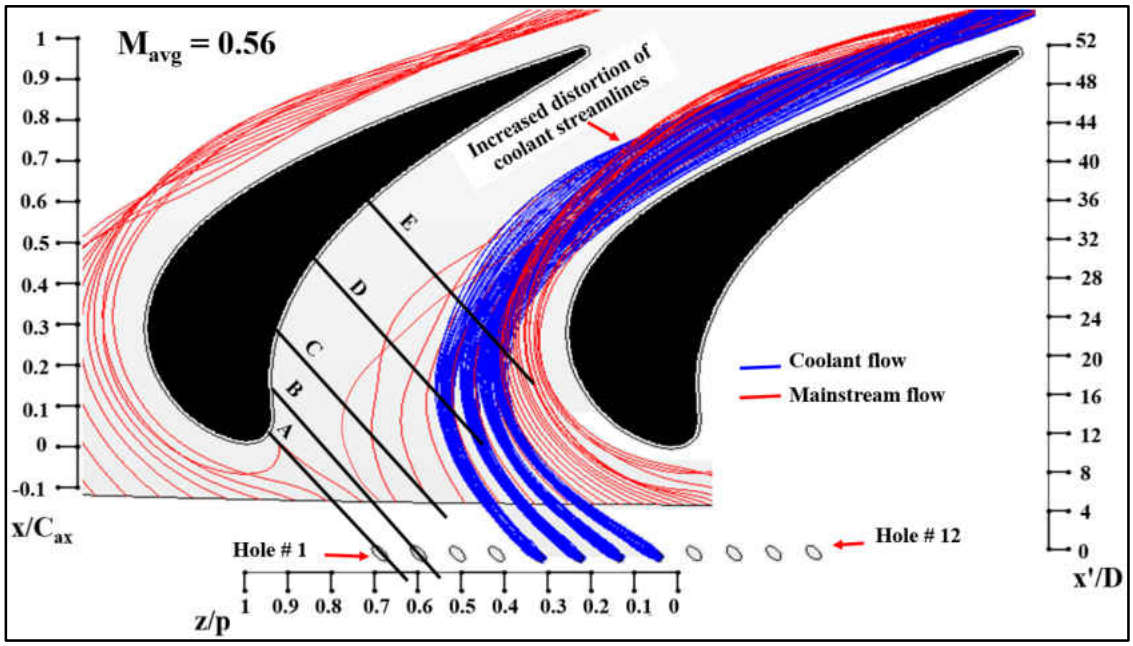

Figure 71: Predicted streamlines of mainstream and coolant flow - case 1b

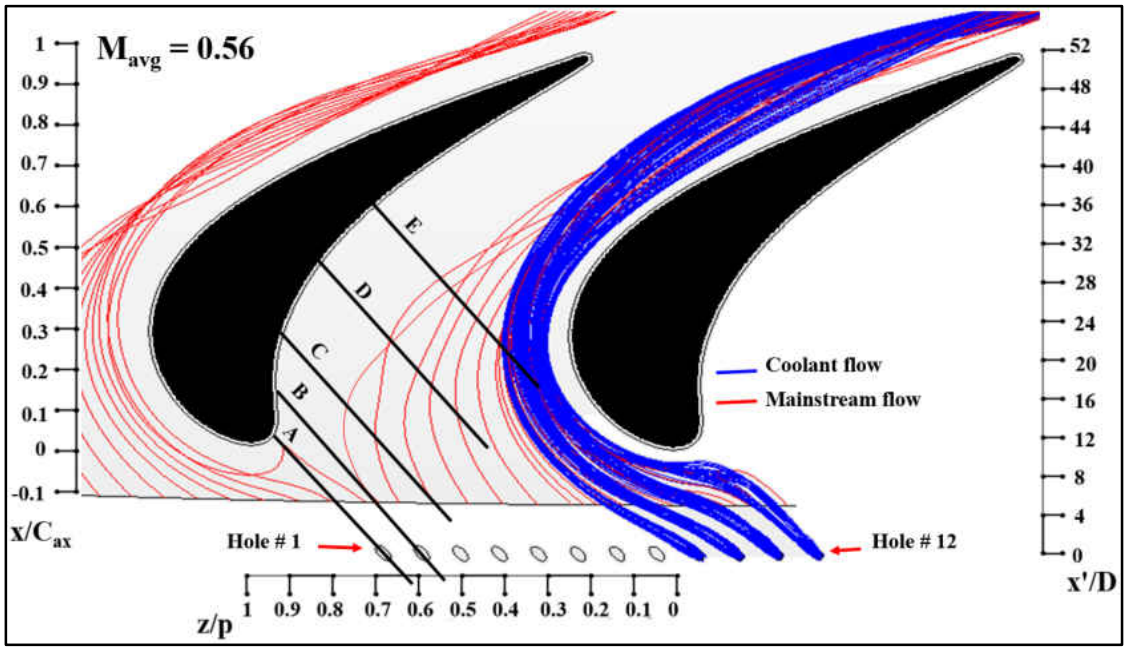

Figure 72: Predicted streamlines of mainstream and coolant flow - case 1c

In the case of set-I film cooling jets in M_{avg} = 1.11 (Figure 73), it can be seen that jet-1 exhibits a similar trajectory as observed in Figure 70. The jets 2-4 have pushed the PV separation line towards the airfoil pressure side due to the increased momentum flux ratio. The vortex structures formed due to the interaction between jet-2 and the airfoil are similar to M_{avg} = 0.56 as observed from the top view of a three-dimensional flow field. In addition, jets-3,4 experience delayed flow turning inside the airfoil passage which is a result of the high momentum flux ratio. Moving downstream, it is noted that the coolant flow streamlines experience less distortion in the downstream region compared to M_{avg} = 0.56, which can be attributed to the film jets retaining their identity better amidst the endwall secondary flows.

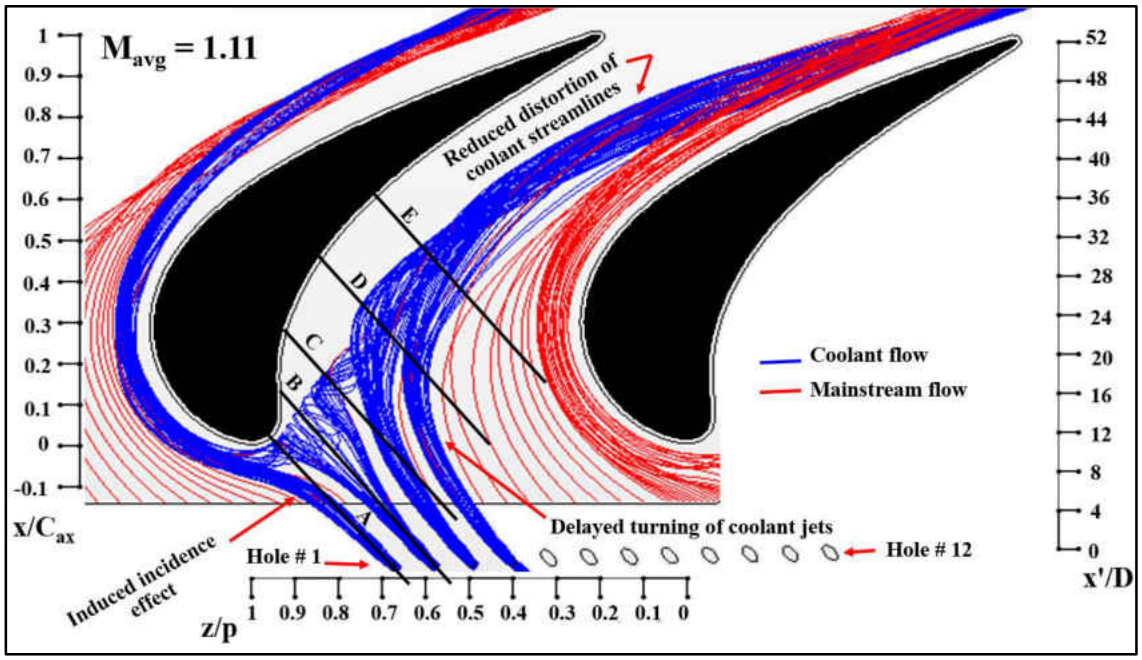

Figure 73: Predicted streamlines of mainstream and coolant flow - case 3a

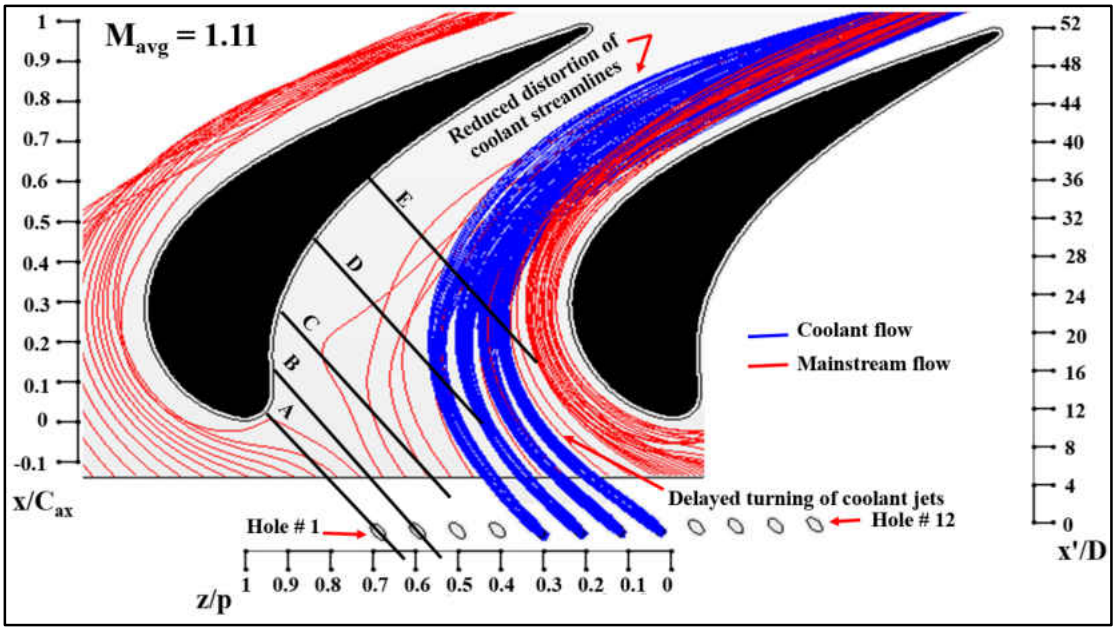

Figure 74: Predicted streamlines of mainstream and coolant flow - case 3b

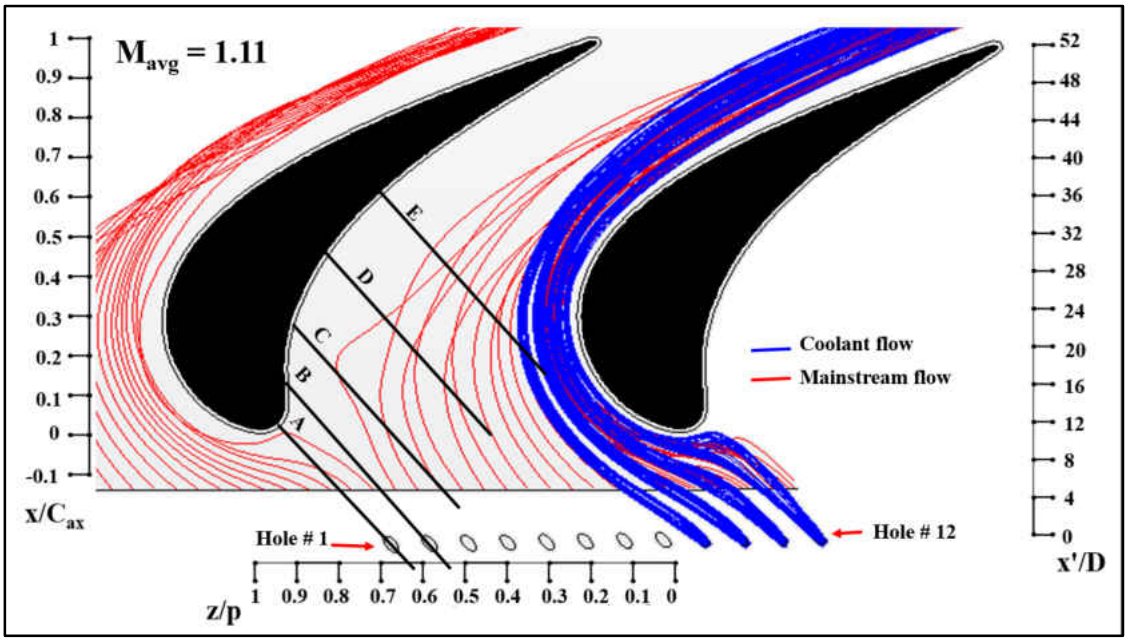

Figure 75: Predicted streamlines of mainstream and coolant flow - case 3c

The film cooling jets 5-8 shown in Figure 74 have a lower blowing ratio compared to the jets located near the airfoil pressure side and hence they have less impact from the jet lift-off consequences. In the downstream region, the reduced impact of the secondary flow on the coolant jets at $M_{avg} = 1.11$ compared to $M_{avg} = 0.56$ is evident from the reduced distortion of the coolant streamlines. The jets 10-12 in $M_{avg} = 1.11$ (Figure 75) exhibit significant turning upstream of the airfoil leading-edge. It can be noted that the uncooled region near the suction side present in $M_{avg} = 0.56$ (Figure 72) has reduced substantially due to the ability of jet-12 to influence the SHV. In the downstream region, the coolant flow streamlines are well-behaved without any significant distortion.

Horseshoe Vortex Dynamics

Due to the complexity in a film-cooled cascade flow field, it is essential to study the coolant - mainstream interaction from different perspectives. In the present study, 5 planes placed at different airfoil chord locations and oriented as shown in Figure 76 were used to visualize the predicted mainstream streamline pattern for $M_{avg} = 0,0.56,1.11$. The planes are also shown in Figures 69-75 to establish the connection with Figures 77-91. The turbulent kinetic energy (k^*) in a normalized form is used to quantify the strength of the secondary flow. The information provided in Figures 77-91 can be used to understand the influence of film injection on the leading-edge horseshoe vortex (LHV) and passage vortex (PV).

In the case of $M_{avg} = 0$ at $s/C = 0$ (Figure 77), it is seen that the streamlines roll up into a horseshoe vortex due to the stagnation pressure gradient near the airfoil leading-edge. The core of the horseshoe vortex is observed to be located at $s'/D_{LE} \cong 0.61$ and y/S

≅ 0.01, where D_{LE} is the leading-edge diameter of the airfoil. Except for the flow near the leading-edge, the streamlines along the airfoil span exhibit close to a horizontal pattern. When film injection is introduced at an average blowing ratio of 0.56 (Figure 78), the streamlines are deflected from the endwall at $s'/D_{LE} \cong 3.3$ due to coolant injection. The suction leg of jet-2 is the primary contributor at s/C = 0 since jet-1 moves into the adjacent airfoil passage due to the induced incidence effect (shown in Figure 70). The LHV has shifted away from the leading-edge due to the endwall cross flow and moved upward compared to $M_{avg} = 0$. The size of the LHV has increased at $M_{avg} = 0.56$ due to the interaction with the suction leg of jet-2. Increasing the blowing ratio to $M_{avg} = 1.11$ (Figure 79) offsets the lift-off location of the streamlines to $s'/D_{LE} \cong 2.94$. The LHV has shifted towards the leading-edge relative to $M_{avg} = 0$ due to the high momentum flux of jet-2. The core of the LHV is positioned at $s'/D_{LE} \cong 0.438$ and $y/S \cong 0.01$.

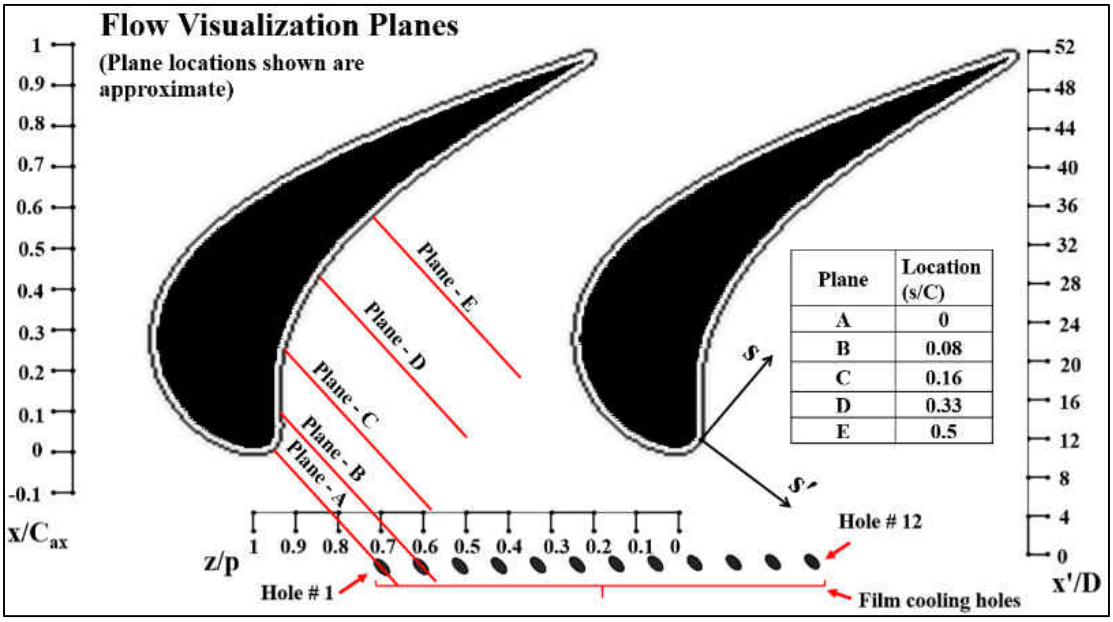

Figure 76: Flow visualization planes for predicted streamlines

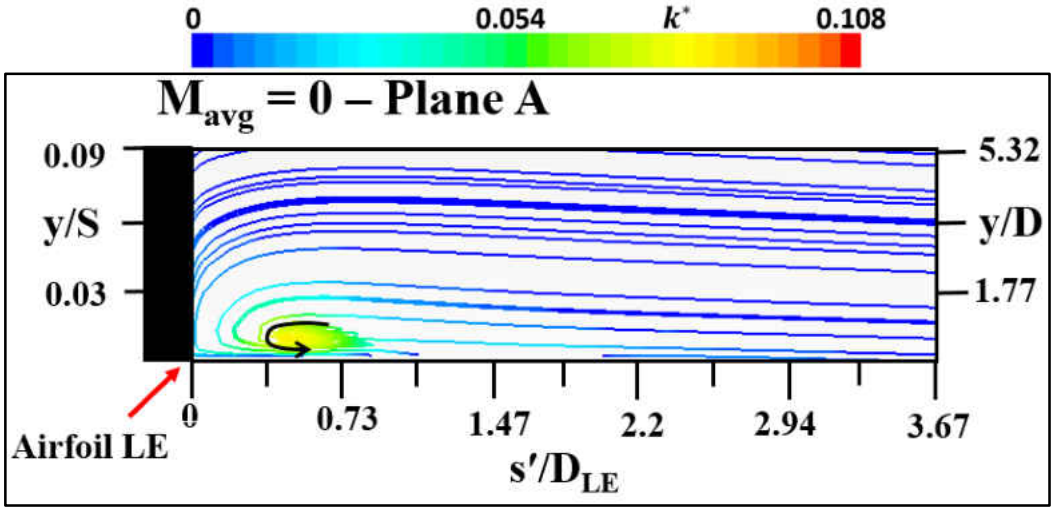

Figure 77: Predicted streamlines for no film injection - plane A

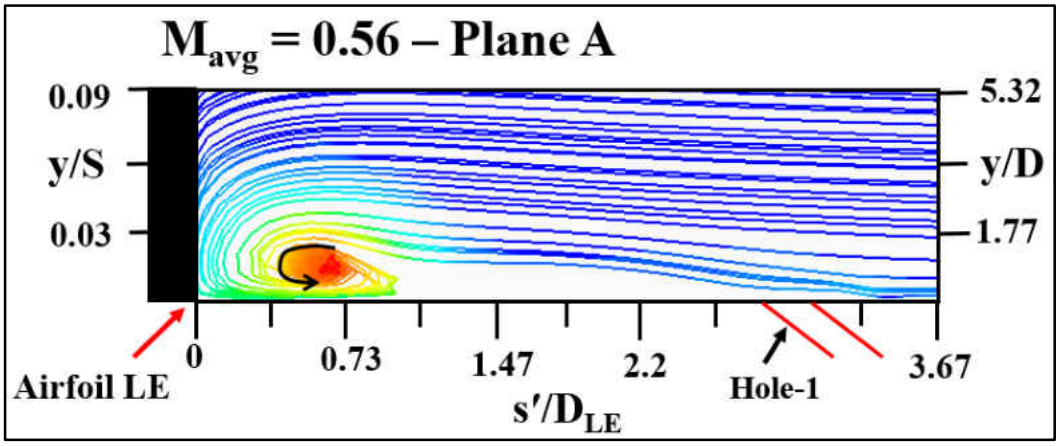

Figure 78: Predicted streamlines for case 1 - plane A

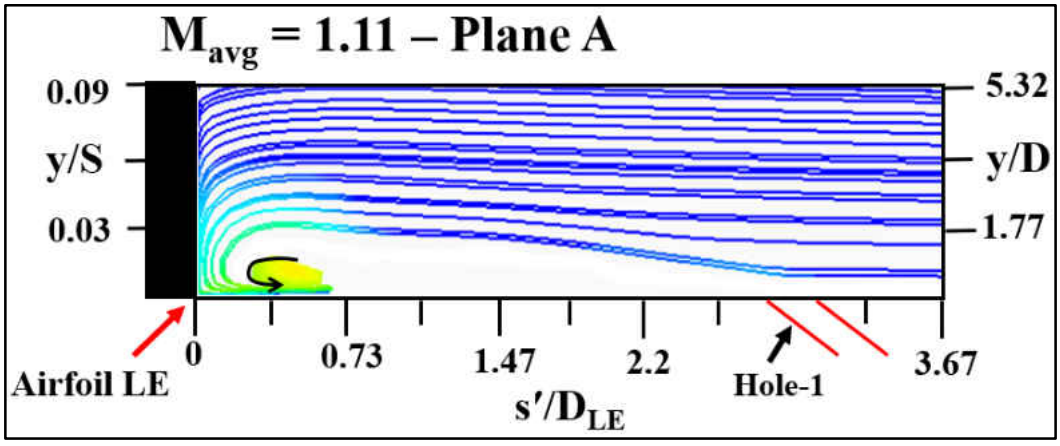

Figure 79: Predicted streamlines for case 3 - plane A

Moving downstream to s/C = 0.08, it is observed that part of the mainstream flow stagnates behind the HV for $M_{avg} = 0$ (Figure 80). This flow stagnation is due to blockage presented by the HV. There is a shift in the core of the HV towards the suction side due to the effect of the endwall cross flow. In the case of $M_{avg} = 0.56$ (Figure 81), jet-2 significantly augments the HV since the direction of jet-2 is aligned with the mainstream streamlines near the airfoil stagnation region. It should be noted here that jet-2 is the sole contributor to the coolant flow at s/C = 0.08. As the average blowing ratio is increased to $M_{avg} = 1.11$ (Figure 82), the HV is intensified due to the influence of jet-2 similar to $M_{avg} = 0.56$. The core of the HV has advanced slightly towards the airfoil pressure side due to the high momentum of jet-2. Although jet-2 has increased strength to penetrate into the mainstream flow at $M_{avg} = 1.11$, it appears that the velocity components of jet-2 decay faster compared to the low momentum film injection. This is indicated by the lower turbulent kinetic energy in the HV at $M_{avg} = 1.11$.

Since s/C = 0.16 is located on the airfoil pressure side, the HV can be referred to as the passage vortex (PV). At s/C = 0.16, it is noticed that for $M_{avg} = 0$ (Figure 83), the flow beneath the PV has started moving the stagnated fluid behind it away from the airfoil pressure side. One major reason for this phenomenon is the increased cross flow at downstream locations inside the airfoil passage. In the case of $M_{avg} = 0.56$ (Figure 84), the PV size has decreased primarily due to the decay of jet-2 and the PV core has shifted away from the airfoil pressure side (due to the endwall cross flow) to $s'/D_{LE} \cong 1.277$. At $M_{avg} = 1.11$ (Figure 85), a decrease in the PV size is noted due to the decay of jet-2 similar to the low blowing ratio case but no significant shift in the PV core is observed.

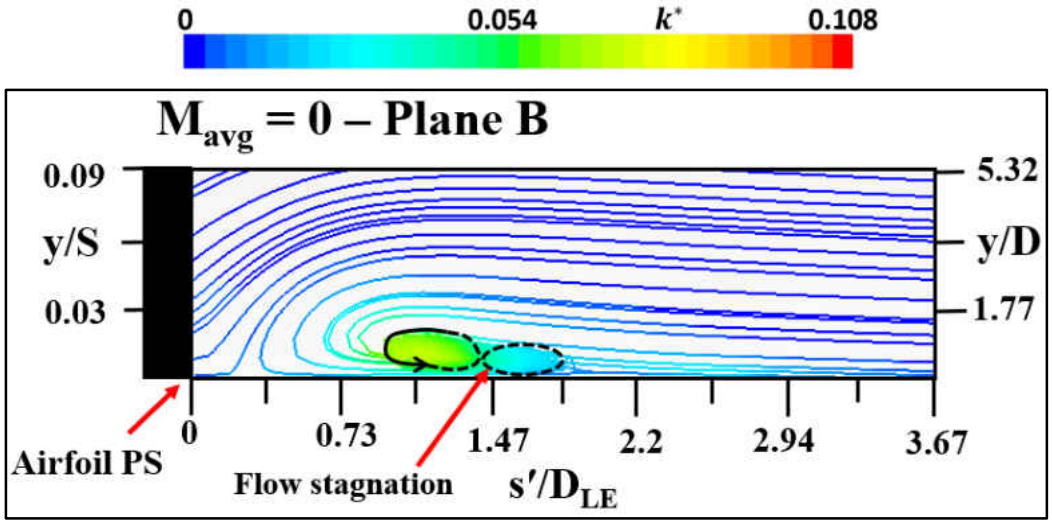

Figure 80: Predicted streamlines for no film injection - plane B

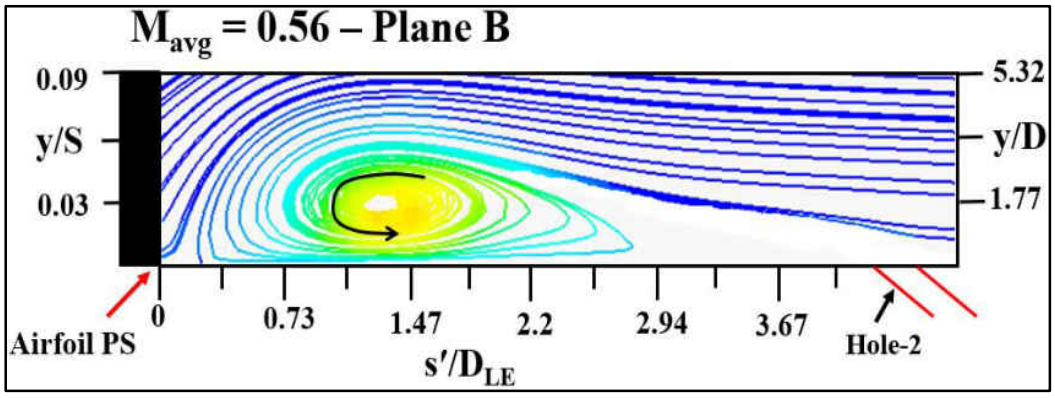

Figure 81: Predicted streamlines for case 1 - plane B

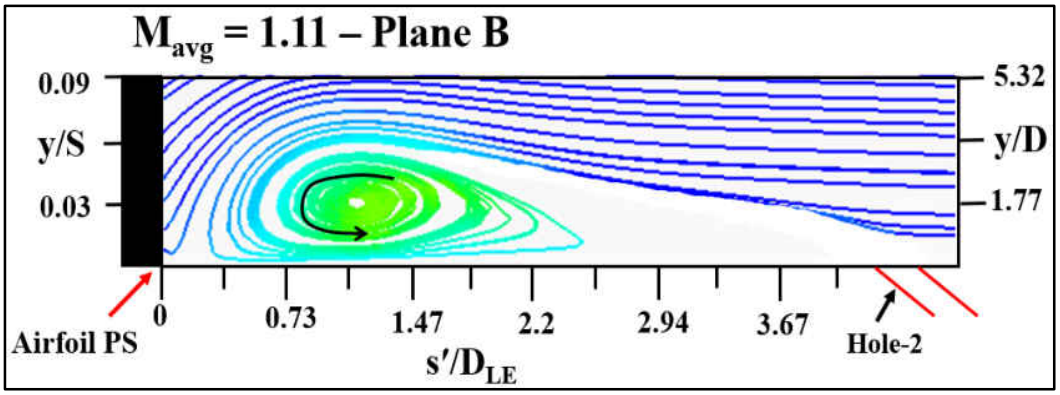

Figure 82: Predicted streamlines for case 3 - plane B

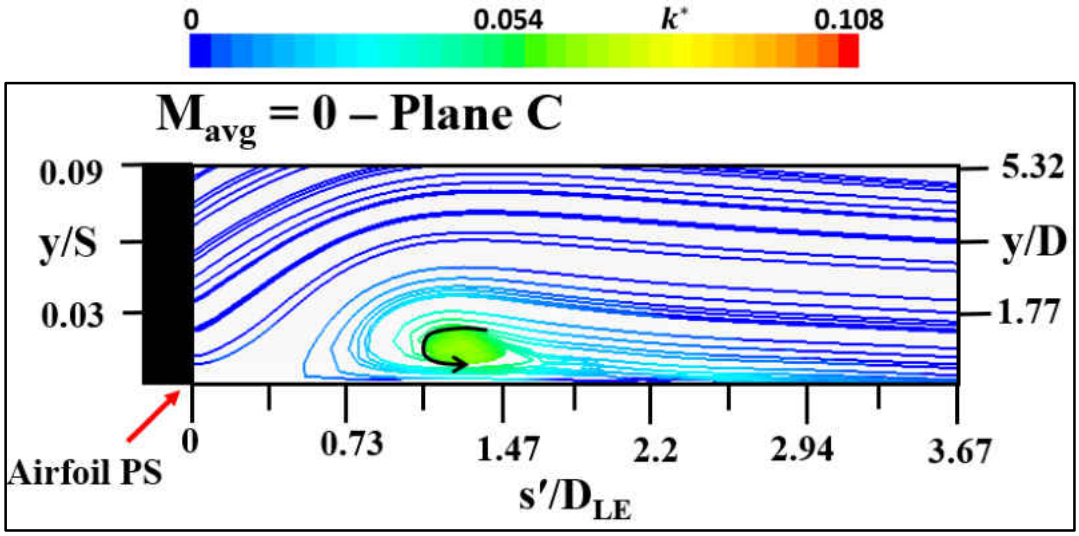

Figure 83: Predicted streamlines for no film injection - plane C

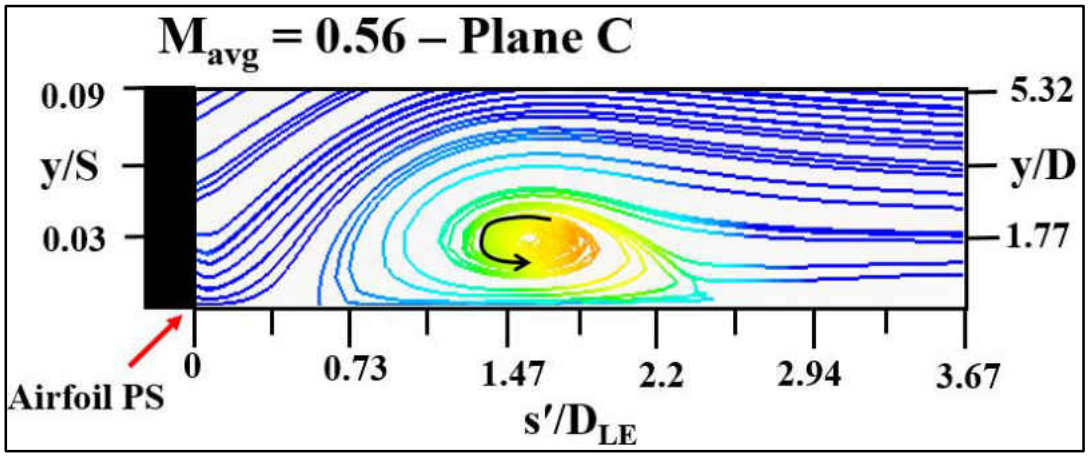

Figure 84: Predicted streamlines for case 1 - plane C

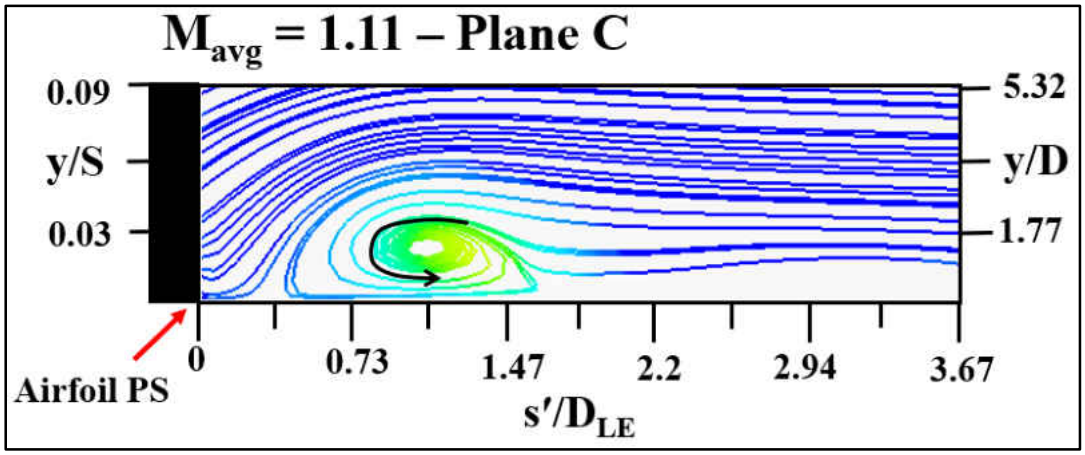

Figure 85: Predicted streamlines for case 3 - plane C

Moving downstream along the airfoil chord to s/C = 0.33, Figure 86 shows the presence of a secondary vortex for $M_{avg} = 0$ with its core located at $s'/D_{LE} \cong 2.75$. Although the PV has moved away from the airfoil pressure side compared to s/C = 0.16, the size is relatively unchanged. This indicates that the secondary vortex structure is formed most likely due to the flow reversal behind the PV and not as a result of PV breakdown. In the case of $M_{avg} = 0.56$ (Figure 87), the PV has decreased in size relative to s/C = 0.16. One major reason for this is that the PV structure is strongly influenced by jets-3,4 at s/C = 0.33. The jets-3,4 experience less streamline distortion as they convect downstream compared to jet-2 since jets-3,4 do not interact with the airfoil. This results in the mitigation of the PV. At $M_{avg} = 1.11$ (Figure 88), it is noted that the PV size has decreased relative to s/C = 0.16 due to the influence of jets-3,4, a similar effect observed at $M_{avg} = 0.56$. The core of the PV has shifted slightly towards the airfoil pressure side due to the high momentum of jets-3,4.

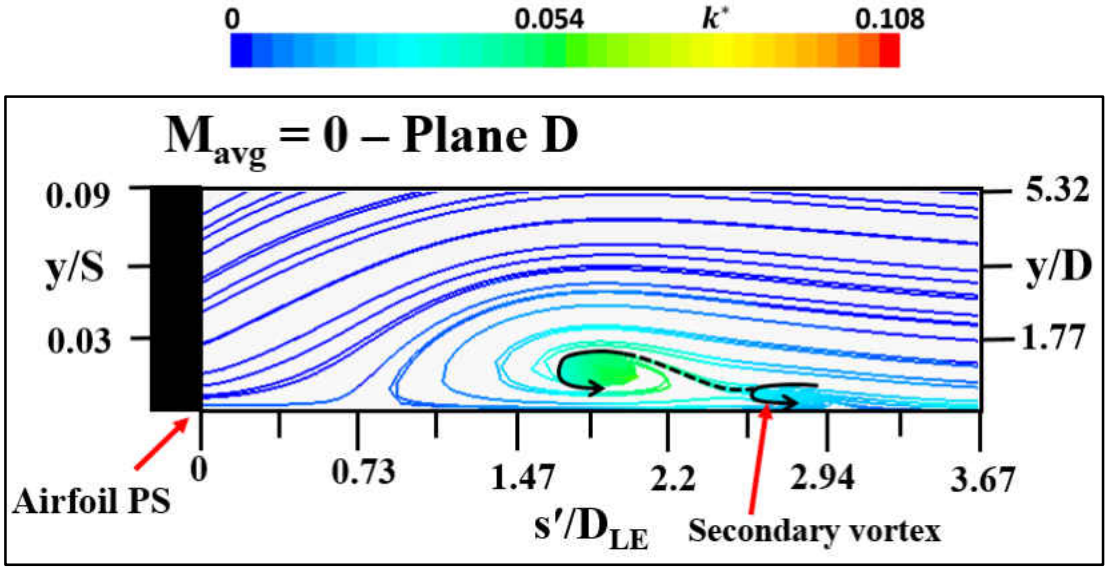

Figure 86: Predicted streamlines for no film injection - plane D

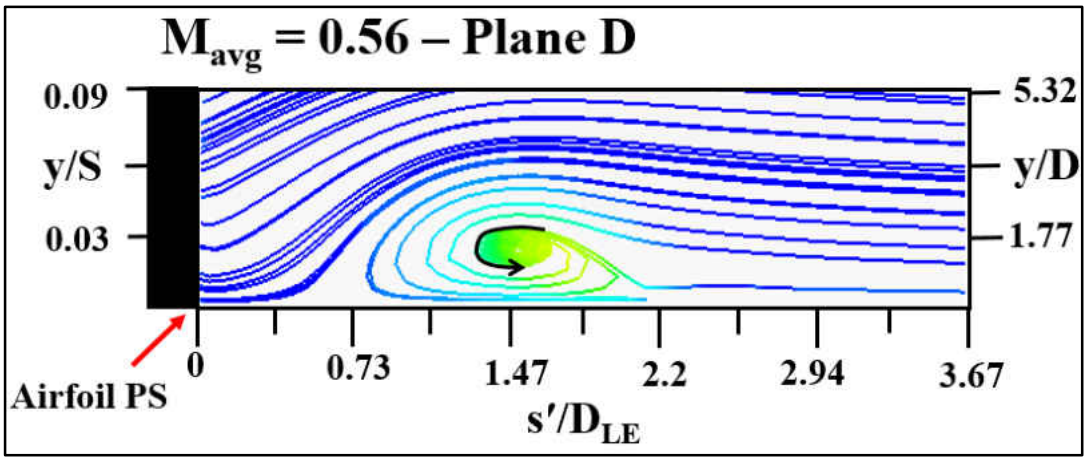

Figure 87: Predicted streamlines for case 1 - plane D

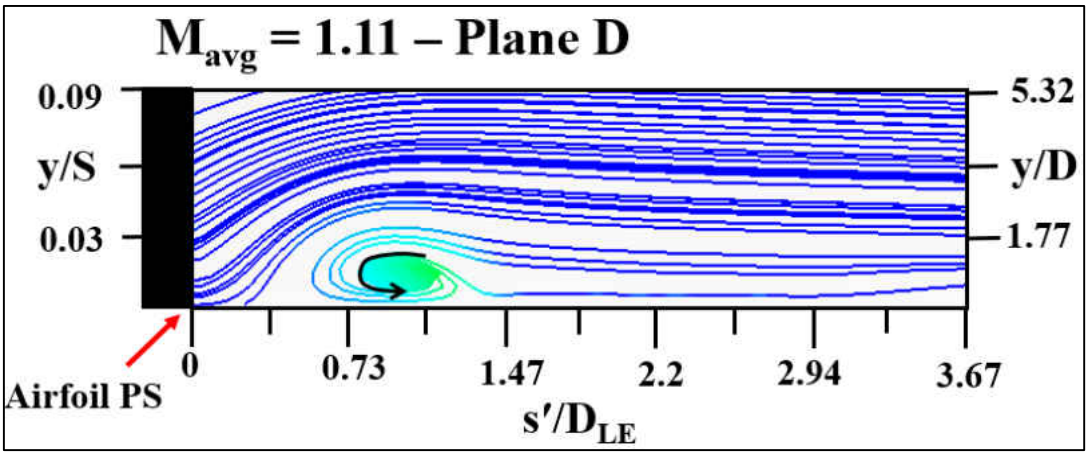

Figure 88: Predicted streamlines for case 3 - plane D

At s/C = 0.5, it is seen that for M_{avg} = 0 (Figure 89) the secondary vortex formed behind the PV at s/C = 0.33 is absent. By comparing Figure 89 and Figure 86, it appears that the secondary vortex has been convected by the accelerating mainstream flow and entrained in the upwash of the PV. This results in an increased fluid accumulation below the PV. When the average blowing ratio is increased to 0.56 (Figure 90), the PV exhibits a slight shift away from the airfoil pressure side due to the endwall cross flow but there is insignificant difference in the PV size and the turbulent kinetic energy relative to s/C =

0.33. This indicates that the contribution from jets-3,4 is similar between s/C = 0.33 and s/C = 0.5. At M_{avg} = 1.11 (Figure 91), the PV shows a size reduction relative to s/C = 0.33. By comparing the PV structure between s/C = 0.33 and s/C = 0.5, it can be said that the jet-4 interaction is significant at s/C = 0.5 which results in a size reduction of the PV.

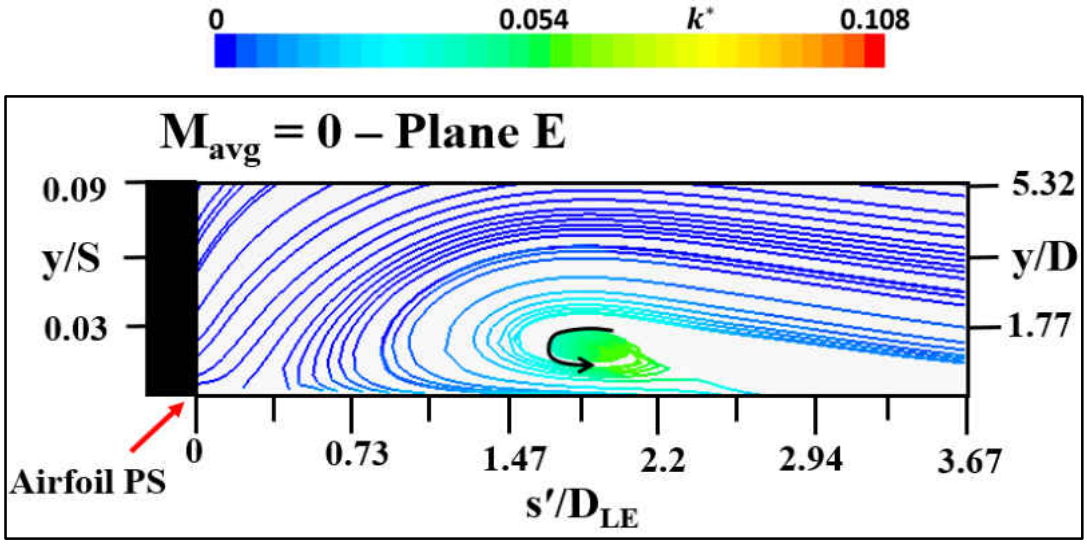

Figure 89: Predicted streamlines for no film injection - plane E

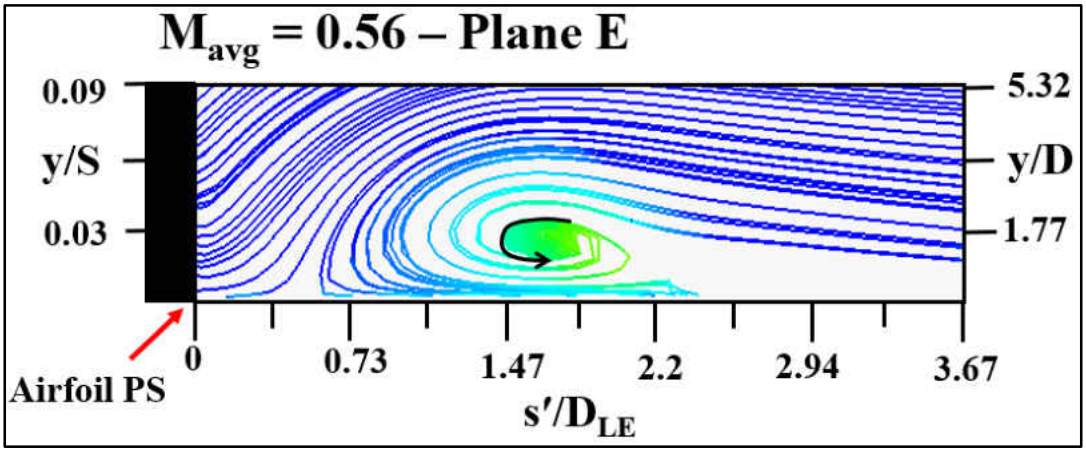

Figure 90: Predicted streamlines for case 1 - plane E

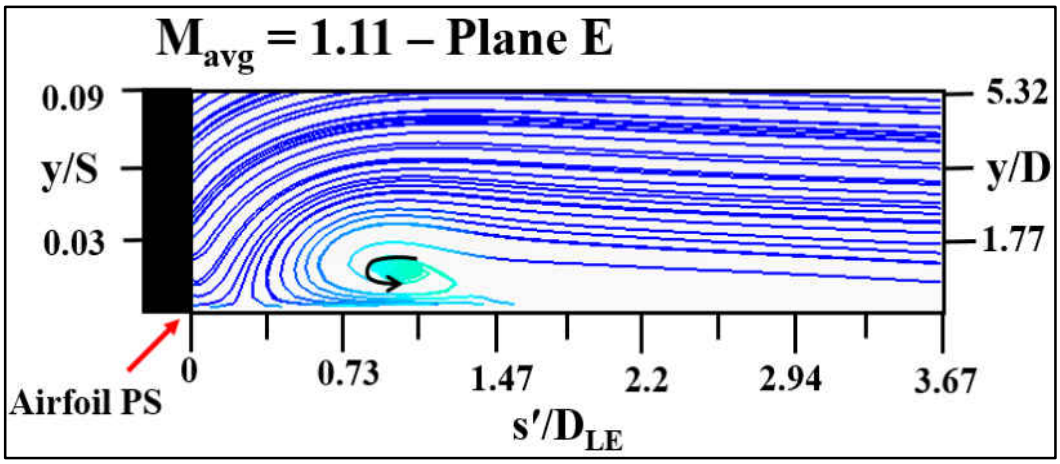

Figure 91: Predicted streamlines for case 3 - plane E

Effect of Discharge Coefficient on Film Cooling Effectiveness

As the coolant jet enters the mainstream flow, it is exposed to a pitchwise variation in the static pressure distribution combined with the saddle point flow at the airfoil-endwall junction. This creates a difference in the flow resistance as experienced by the film cooling jets resulting in varying film cooling hole discharge for the same average blowing ratio. It is essential to know the individual film cooling hole mass flow rate for a given cooling configuration to obtain the local blowing ratio for the film cooling holes (after considering the corresponding local mainstream velocity and density ratio). The individual film cooling hole mass flow rate as a percentage of the total coolant mass flow rate is given in Figure 92. The discharge coefficient for each film cooling hole at different average blowing ratios is shown in Figure 93.

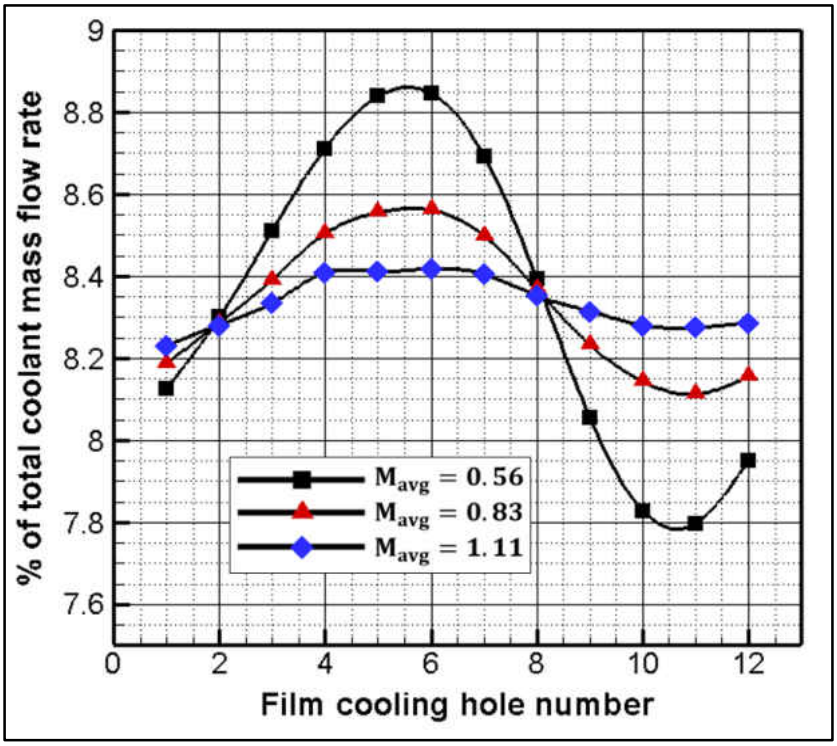

Figure 92: Predicted film cooling hole mass flow rate

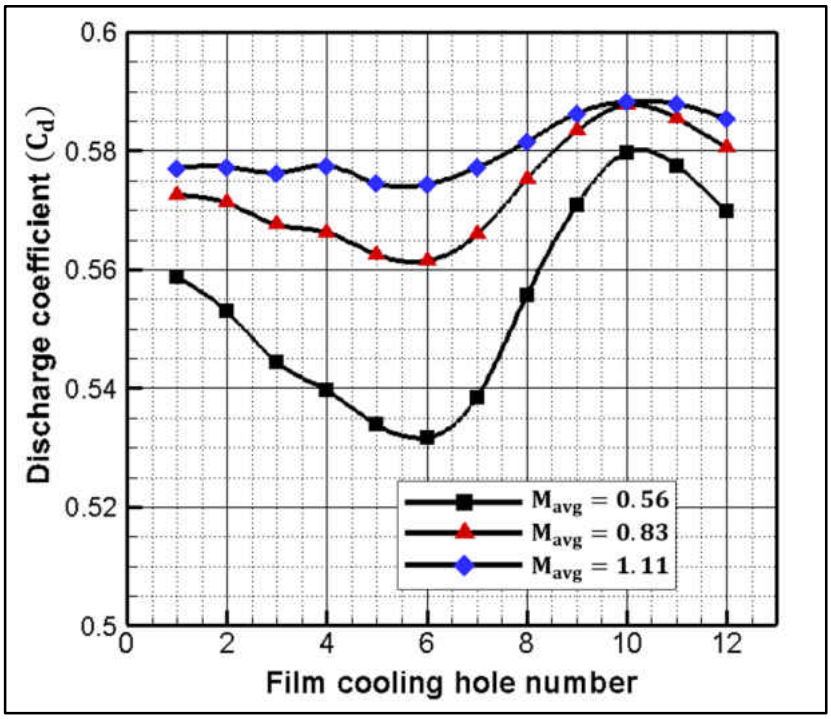

Figure 93: Predicted film cooling hole discharge coefficients

It is noted from Figure 92 that there is a significant variation in the mass flow rate between the film cooling holes at M_{avg} = 0.56. A maximum difference of ≅ 8.9% is observed between hole-1and hole-6. This variation is due to a combined effect of the local mainstream static pressure, the location of the film cooling hole relative to the endwall separation lines and the coolant momentum flux. At M_{avg} = 0.83, the maximum variation in the mass flow rate between hole-1and hole-6 is reduced to ≅ 4.6 % due to the increased coolant momentum flux. For blowing ratios above M_{avg} = 0.83, there is less than 2.4% maximum variation in the mass flow rate between the film cooling holes. Relating this information to the discharge coefficient distribution (Figure 93), it is inferred that the variation in discharge coefficient is primarily due to the variation in the individual film cooling hole mass flow rate and the mainstream static pressure which influences the theoretical mass flow rate. The dynamic compound angle of the film cooling hole is influenced by the endwall separation lines and has an implicit effect on the discharge coefficient.

At M_{avg} = 0.56, it is seen that there is a maximum difference of ≅ 4.8 % in the discharge coefficient between hole-1 and hole-6. This difference can be higher if the film cooling holes are located closer to the airfoil leading-edge or if the flow turning inside the airfoil passage is increased. After hole-6, the discharge coefficient exhibits a steady increase till hole-10. This increase is due to the lower mainstream static pressure near the airfoil suction side. Beyond hole-10, there is a drop in the discharge coefficient as it approaches the value of hole-1. There is less than 2% difference between hole-1 and hole-12 discharge coefficients, confirming the flow periodicity between hole-1 and hole-12.

At M_{avg} = 0.83, there is an increase in the discharge coefficients for all the holes relative to M_{avg} = 0.56 due to the higher coolant momentum flux. A maximum increase of ≅ 5.6 % is noted for hole-6. In addition, the variation in discharge coefficients between the film cooling holes has decreased, with a maximum difference of ≅ 2.65 % between hole-1 and hole-10. The trend in the discharge coefficient variation is similar to M_{avg} = 0.56. As the blowing ratio is increased to M_{avg} = 1.11, there is a further increase in the discharge coefficients compared to M_{avg} = 0.83. It is observed that the increase is higher for holes 8-12 than the other holes. A maximum increase of ≅ 2.75 % is noted for hole-10. The maximum variation in the discharge coefficient between the film cooling holes is less than 2%.

As mentioned in the discussion of the film cooling holes mass flow rate fraction, the coolant jet discharge appears to be a strong function of the average blowing ratio, mainstream static pressure and the location of the endwall separation lines which influences the dynamic compound angle. The varying dynamic compound angle among the film cooling jets changes the flow resistance as experienced by the jets.

In a flat plate film cooling scenario, some important parameters that influence the film cooling hole discharge coefficients include the hole length-to-diameter ratio (L/D), inclination angle (α), compound angle (β), mainstream Mach number (Ma_∞), and coolant plenum Mach number (Ma_c) as pointed out by Gritsch et al. [11]. In addition to this, the dynamic compound angle (β_d) and the local mainstream static pressure also influence the film cooling hole discharge coefficients in a cascade flow field. In the present study, the coolant plenum has negligible cross flow and so $Ma_c \cong 0$. Since the L/D of the film cooling hole is ≅ 17, the flow inside the hole is not undeveloped or does not experience an

increased effective inclination angle [12]. It can be said that the hole exit flow conditions have a strong impact on the mass flow rate through the hole for subsonic flow conditions inside the hole.

Effect of Local Blowing Ratio on Film Cooling Effectiveness

The individual film cooling hole blowing ratios are shown in Figure 94. As a general trend, the local blowing ratio increases near the airfoil pressure side due to the low mainstream velocity and decreases near the airfoil suction side. At M_{avg} = 0.56, the maximum difference (≅ 4.4 %) in the local blowing ratio is observed between hole-1 and holes-6,7. The lowest blowing ratio is observed for holes-6,7 located near the suction side. Increasing the average blowing ratio to 0.83, augments the variation in the local blowing ratio up to ≅ 7.1 % between hole-1 and holes-6,7. This results in a partial jet lift-off for jets-2,3 relative to M_{avg} = 0.56 as seen by comparing Figures 66 and 67.

As the average blowing ratio increases to 1.11, the blowing ratio variation among the film cooling holes is amplified. The highest difference (≅ 10.7 %) in the local blowing ratio is observed between hole-1 and hole-6. Both jet-2 and jet-3 show significant lift-off at M_{avg} = 1.11 as inferred from Figure 68.

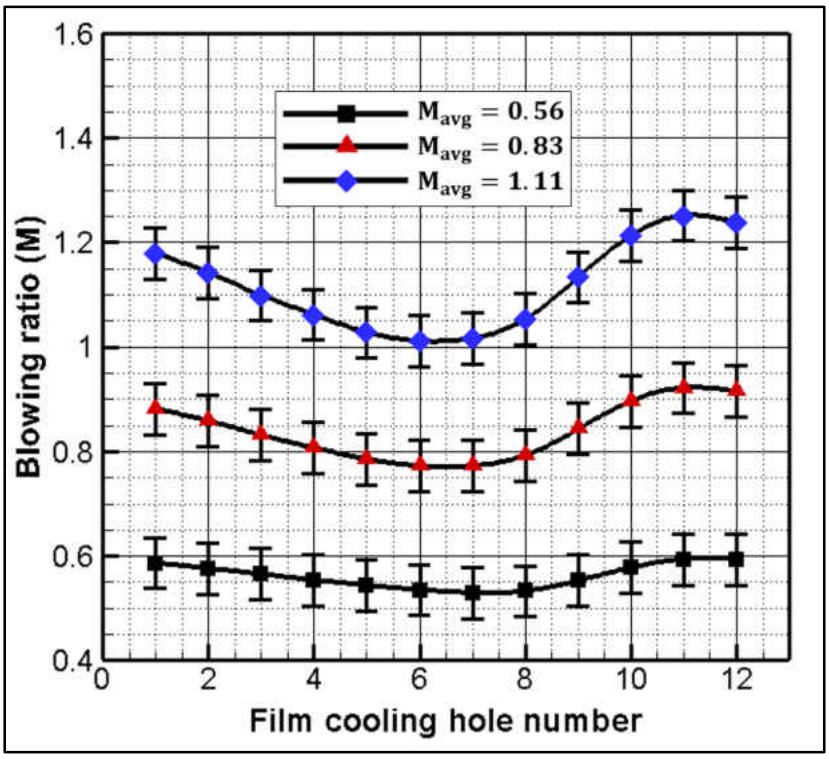

Figure 94: Local blowing ratio for film cooling holes

Pitchwise Film Cooling Effectiveness

Due to the complex secondary flows and pressure gradients in an airfoil passage, it is essential to quantify the local variation in the film cooling effectiveness along the pitchwise direction which cannot be represented in the more commonly reported pitch-averaged film cooling effectiveness in endwall film cooling studies. In the present study, this local variation is quantified using pitchwise film cooling effectiveness and a cooling uniformity coefficient (reported in the next section). Due to higher intensity fluctuations in the TSP image near the airfoil walls and in the far downstream of the airfoil passage ($x/C_{ax} > 0.8$), the pitchwise film cooling effectiveness values in this region are not reported. The pitchwise film cooling effectiveness results are shown in Figures 95-103. In addition, the

pitch-averaged film effectiveness values at each axial chord location are provided in Table 11.

Table 11: Pitch-averaged film cooling effectiveness at various axial chord locations

Pitch-averaged film cooling effectiveness ($\bar{\eta}$)			Axial chord location (x/C_{ax})
$M_{avg} = 0.56$	$M_{avg} = 0.83$	$M_{avg} = 1.11$	
0.219	0.235	0.242	0
0.196	0.227	0.236	0.1
0.184	0.204	0.237	0.2
0.165	0.196	0.227	0.3
0.15	0.181	0.211	0.4
0.127	0.158	0.197	0.5
0.102	0.13	0.173	0.6
0.09	0.113	0.158	0.7
0.08	0.097	0.14	0.8

At $x/C_{ax} = 0$ (Figure 95), it can be seen that there is significant increase in the film cooling effectiveness for $0.05 \leq z'/p \leq 0.175$ at $M_{avg} = 0.83,1.11$ compared to $M_{avg} = 0.56$. The maximum increase ($\cong 81\%$) in the film cooling effectiveness occurs at $z'/p \cong 0.05$ for $M_{avg} = 1.11$. Since the film cooling jets coalesce near the airfoil suction side (shown in Figure 66), the discrete film cooling jet peaks are not distinguishable in this region. The reduced film cooling effectiveness close to the airfoil suction side shoulder is due to the SHV that prevents the coolant from completely reaching the airfoil. Moving away from the airfoil suction side, it can be seen that there is a zone of nearly uniform film cooling effectiveness ($0.28 \leq z'/p \leq 0.55$) for all blowing ratios.

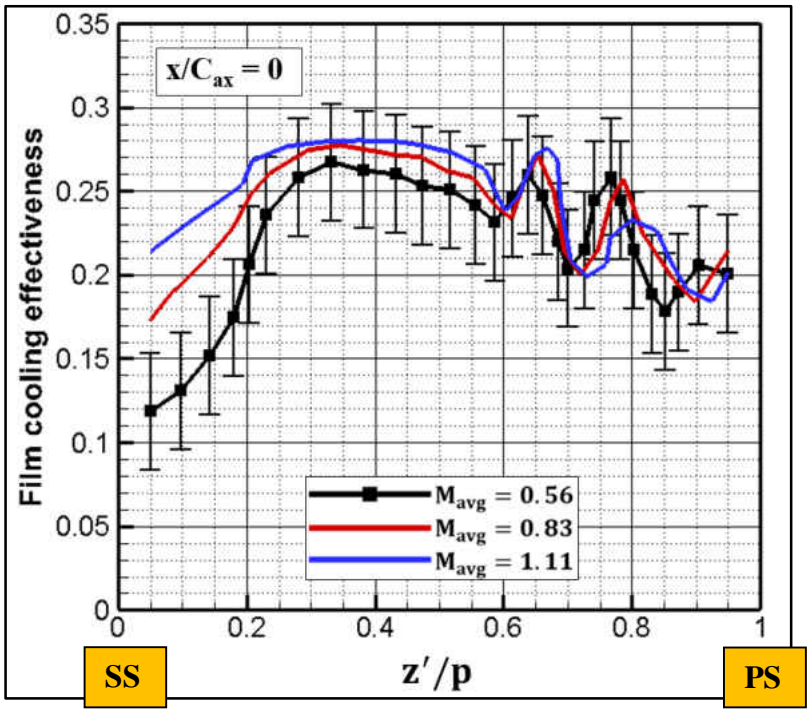

Figure 95: Pitchwise film cooling effectiveness at 0% axial chord

Beyond z′/p ≅ 0.55, discrete film jet peaks start to appear due to the absence of streamwise flow acceleration. The discrete film cooling jets near the airfoil pressure side are absent at $x/C_{ax} = 0.1$ (Figure 96) for $M_{avg} = 0.56$ but are visible for the other blowing ratios. Near the airfoil suction side, there is a considerable increase in the film cooling effectiveness between $M_{avg} = 0.56$ and $M_{avg} = 1.11$ with a maximum increase of ≅ 79% observed at z′/p ≅ 0.05.

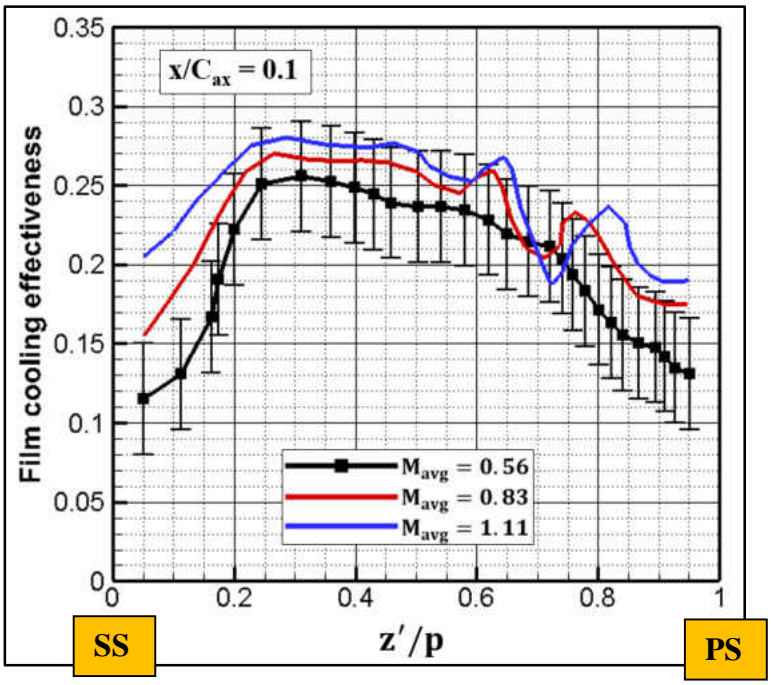

Figure 96: Pitchwise film cooling effectiveness at 10% axial chord

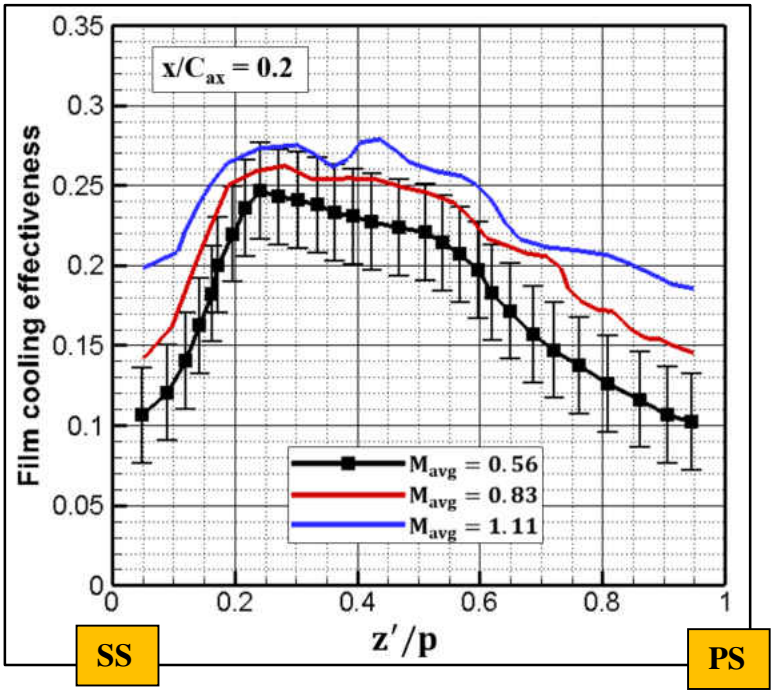

Figure 97: Pitchwise film cooling effectiveness at 20% axial chord

Due to the pitchwise pressure gradient, the coolant is moved to the airfoil suction side which is evident till x/C_{ax} = 0.5. This "coolant accumulation effect" is higher for M_{avg} = 0.56,0.83 compared to M_{avg} = 1.11 due to the low momentum flux ratio (I_{avg} = 0.35,0.77) which reduces the capability of the film cooling jets to influence the endwall secondary flow. At x/C_{ax} = 0.2 (Figure 97), the discrete film jets are no longer visible for M_{avg} = 0.56,0.83,1.11. One reason for this is that part of the film cooling jets have coalesced and part of the coolant has been transported from the endwall by the PV and SHV. It is seen that the decay rate in the film cooling effectiveness at x/C_{ax} = 0.3 (Figure 98) for M_{avg} = 0.56 is steeper past $z'/p \cong 0.43$. The discrete film cooling jets near the airfoil pressure side are not visible for any of the blowing ratios.

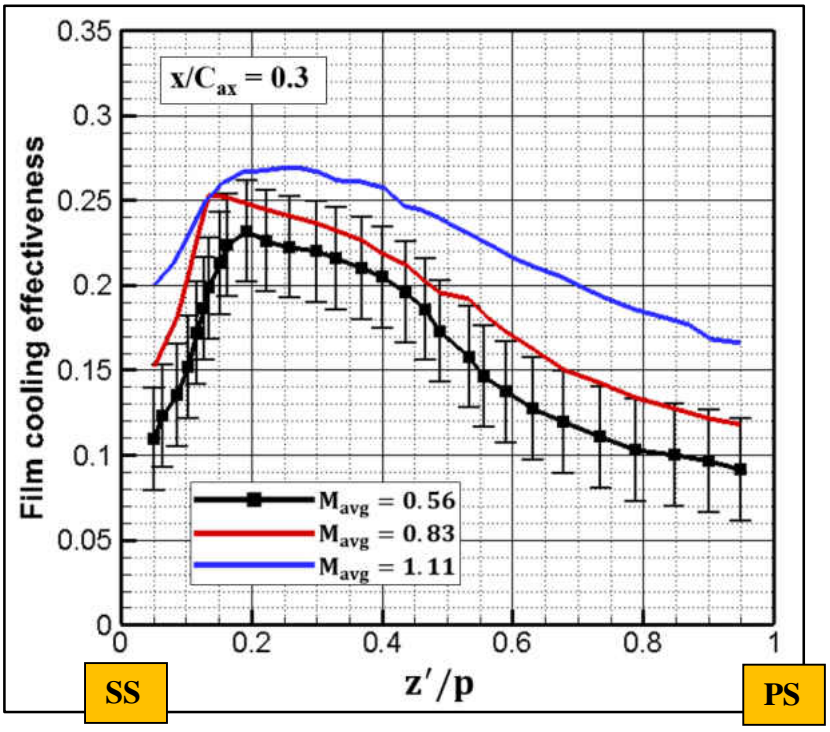

Figure 98: Pitchwise film cooling effectiveness at 30% axial chord

At x/C_{ax} = 0.4 (Figure 99), the non-uniformity in the coolant coverage increases with most of the coolant present in the region close to the airfoil suction side ($0.05 \leq z'/p \leq 0.4$) for all the blowing ratios. The decay rate in the film cooling effectiveness beyond $z'/p = 0.4$ is similar between M_{avg} = 0.56,0.83,1.11. Moving downstream to x/C_{ax} = 0.5, it is noted from Figure 100 that approximately 30% of the pitchwise distance near the airfoil pressure side has less than 11% film cooling effectiveness for M_{avg} = 0.56,0.83. At higher blowing ratios, this coolant deficit is low because of the film cooling jets' increased momemtum that alters the size and location of the vortices thereby providing cooling to most of the pitchwise distance. At $z'/p \cong 0.5$, there is ≅ 93% increase in the film cooling effectiveness between M_{avg} = 0.56 and M_{avg} = 1.11.

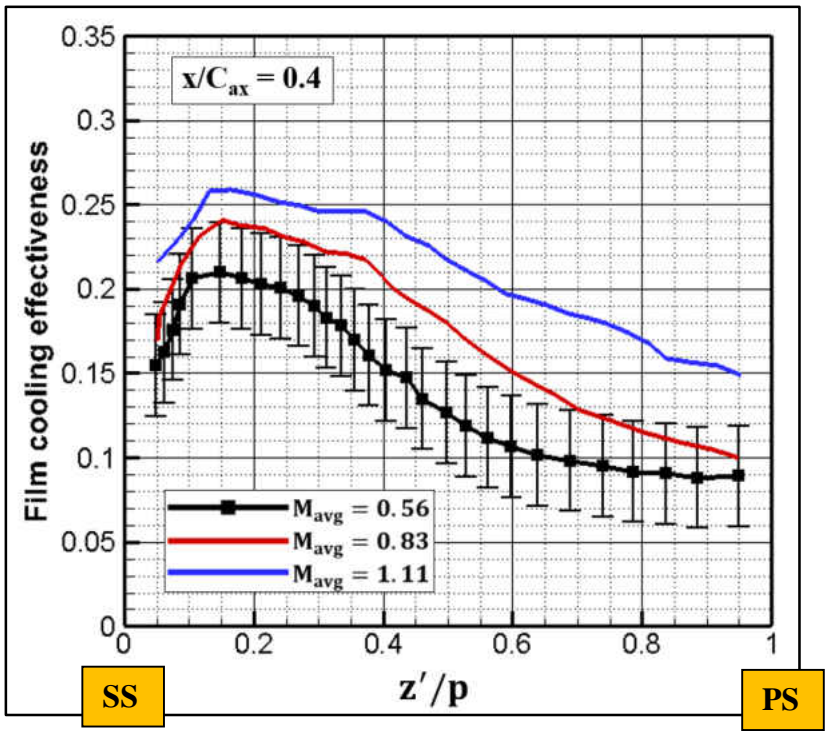

Figure 99: Pitchwise film cooling effectiveness at 40% axial chord

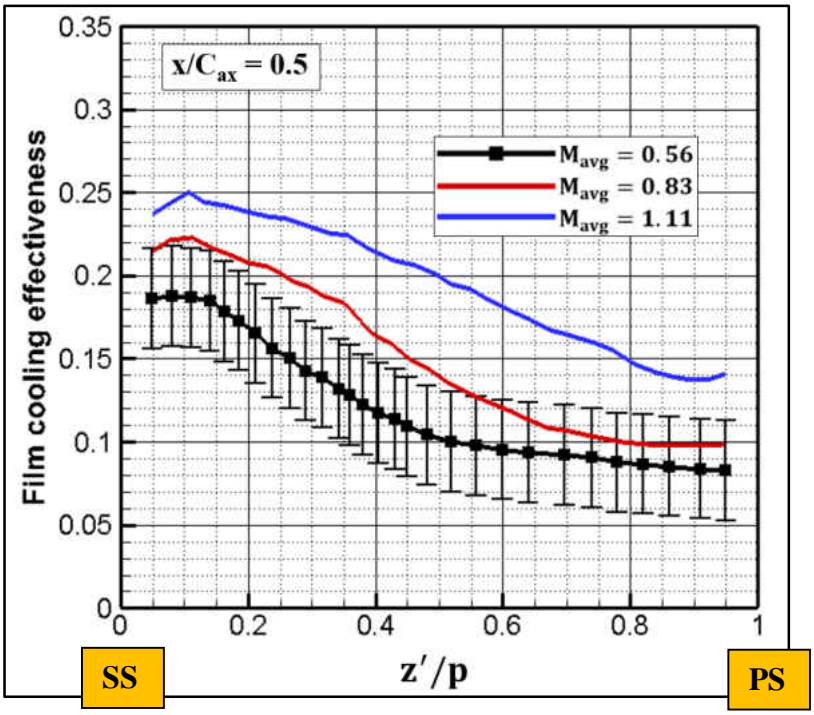

Figure 100: Pitchwise film cooling effectiveness at 50% axial chord

At x/C_{ax} = 0.6 (Figure 101), it is noted that there is 13% or less film cooling effectiveness for $0.4 \leq z'/p \leq 0.95$ in the case of M_{avg} = 0.56,0.83. A maximum increase ($\cong$ 95%) in the film cooling effectiveness is noted at $z'/p \cong 0.43$ between M_{avg} = 0.56 and M_{avg} = 1.11. At x/C_{ax} = 0.7 (Figure 102), about 50% of the region near the airfoil pressure side has 10% or less film cooling effectiveness in the case of M_{avg} = 0.56,0.83. Near the airfoil suction side, the highest film cooling effectiveness ($\cong$ 0.21) occurs at $z'/p \cong 0.05$ for M_{avg} = 1.11.

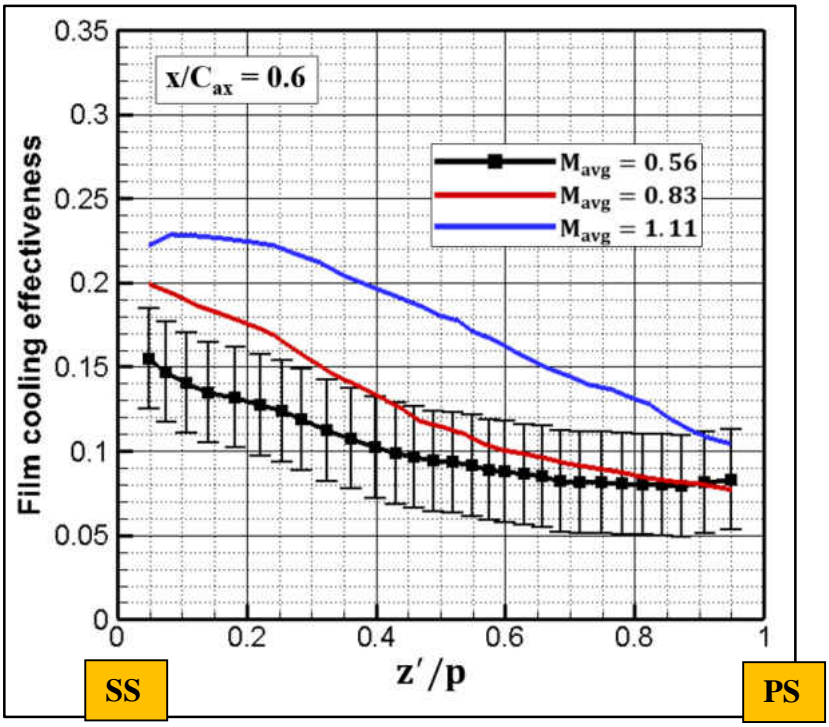

Figure 101: Pitchwise film cooling effectiveness at 60% axial chord

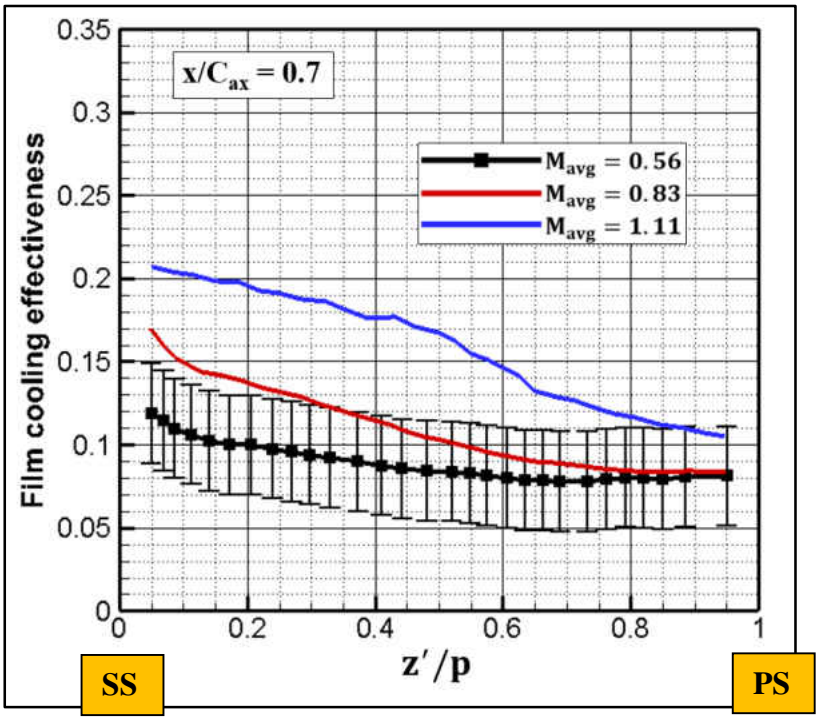

Figure 102: Pitchwise film cooling effectiveness at 70% axial chord

For the low blowing ratios (M_{avg} = 0.56,0.83), Figure 103 shows that ≅ 80% of the region near the airfoil pressure side has 10.6% or less film cooling effectiveness at x/C_{ax} = 0.8. About 40% of the pitchwise distance near the airfoil pressure side has 13% or less film cooling effectiveness for M_{avg} = 1.11.

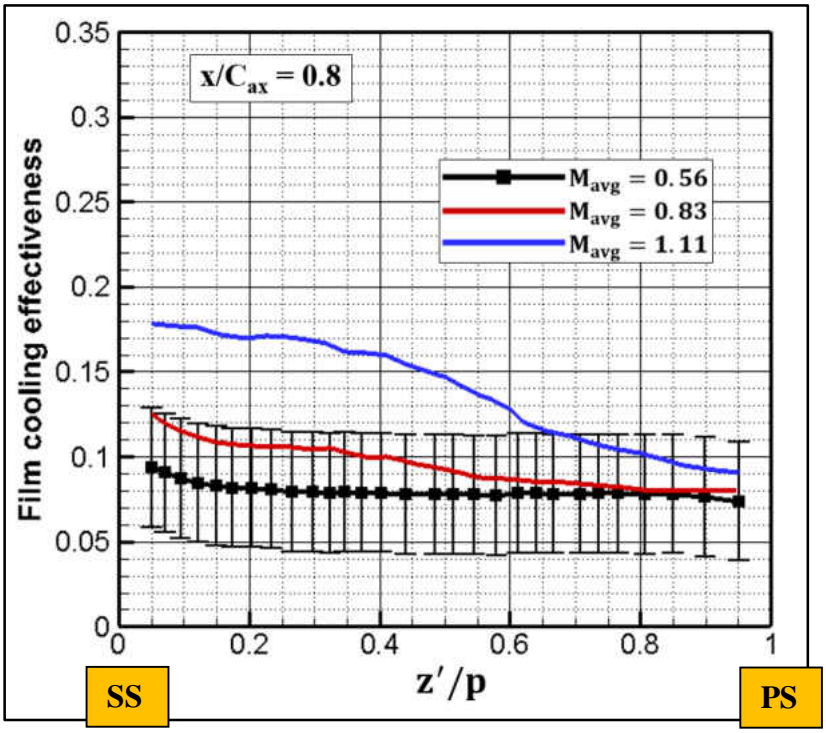

Figure 103: Pitchwise film cooling effectiveness at 80% axial chord

In order to study the difference in the film cooling effectiveness along the various streamwise locations for a fixed average blowing ratio, Figures 104-106 provide the film cooling effectiveness for x/C_{ax} = 0 to x/C_{ax} = 0.8 for a specific average blowing ratio. The streamwise location, x/C_{ax} = 0 is used as a reference to compare the film cooling effectiveness at the downstream locations.

For M_{avg} = 0.56 (Figure 104), the streamwise locations x/C_{ax} = 0,0.1,0.2 exhibit negligible difference till z′/p ≅ 0.6. The discrete film jets are visible only at x/C_{ax} = 0. Past

z′/p = 0.6, there is a significant decrease in film cooling effectiveness at x/C_{ax} = 0.2 with a maximum drop of ≅ 93% occuring at z′/p ≅ 0.9. Moving downstream of the airfoil passage, the "coolant accumulation effect" is noted to be dominant for x/C_{ax} = 0.3,0.4,0.5,0.6. The locations beyond x/C_{ax} = 0.6 have negligible variation in film cooling effectiveness across the pitchwise distance between the airfoils. There is less than 12% film cooling effectiveness at these locations.

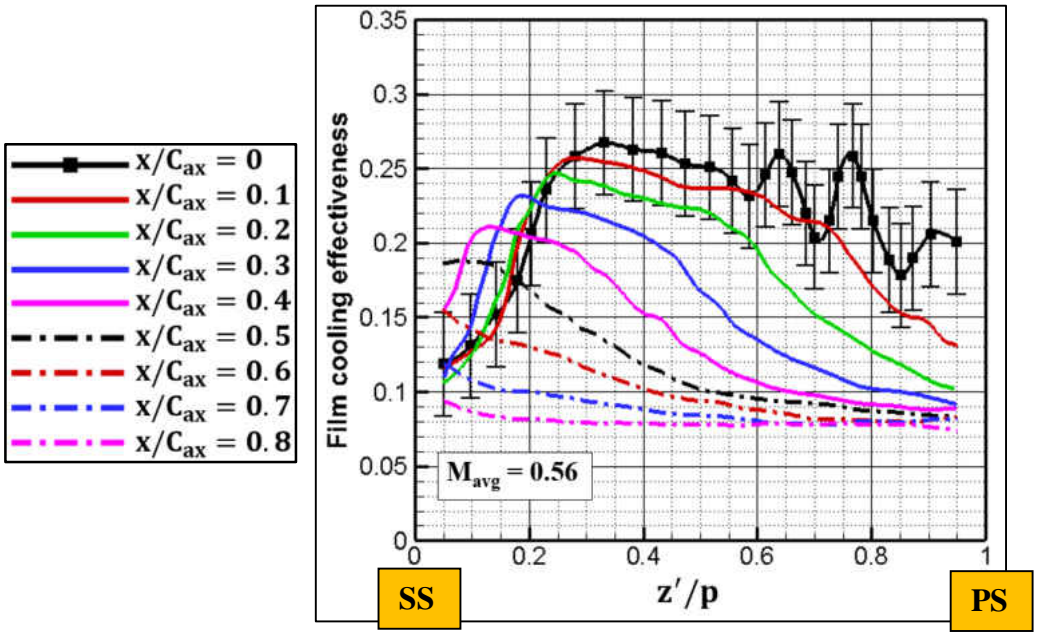

Figure 104: Pitchwise film cooling effectiveness - case 1

The trend in film cooling effectiveness for M_{avg} = 0.83 (Figure 105) at x/C_{ax} = 0 is similar to M_{avg} = 0.56. The streamwise locations x/C_{ax} = 0.1,0.2 exhibit negligible difference compared to x/C_{ax} = 0 till z′/p ≅ 0.74. Past z′/p ≅ 0.74, there is a significant drop in the film cooling effectiveness at x/C_{ax} = 0.2 with a maximum decrease of ≅ 49% at z′/p ≅ 0.79. For the downstream locations between x/C_{ax} = 0.3 and x/C_{ax} = 0.6, the coolant persists for an increased pitchwise distance before decaying to less than 9% film

cooling effectiveness at z′/p ≅ 0.95. The streamwise locations beyond x/C_{ax} = 0.6 have less than 10.3% film cooling effectiveness for at least 50% of the region near the airfoil pressure side.

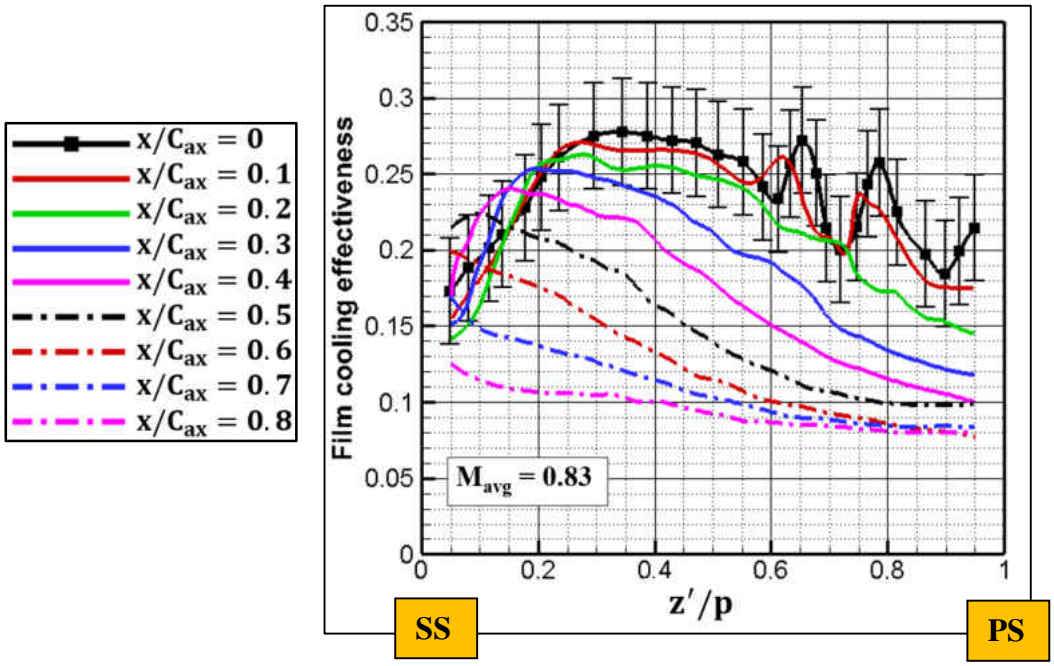

Figure 105: Pitchwise film cooling effectiveness - case 2

At M_{avg} = 1.11 (Figure 106), there is a noteable improvement in the film cooling effectiveness along the pitchwise distance with the lowest film effectiveness ≅ 14%. The decay trend is very similar for the locations between x/C_{ax} = 0.3 and x/C_{ax} = 0.8. Past x/C_{ax} = 0.6, there is less than 13% film cooling effectiveness for ≅ 30% of the region near the airfoil pressure side.

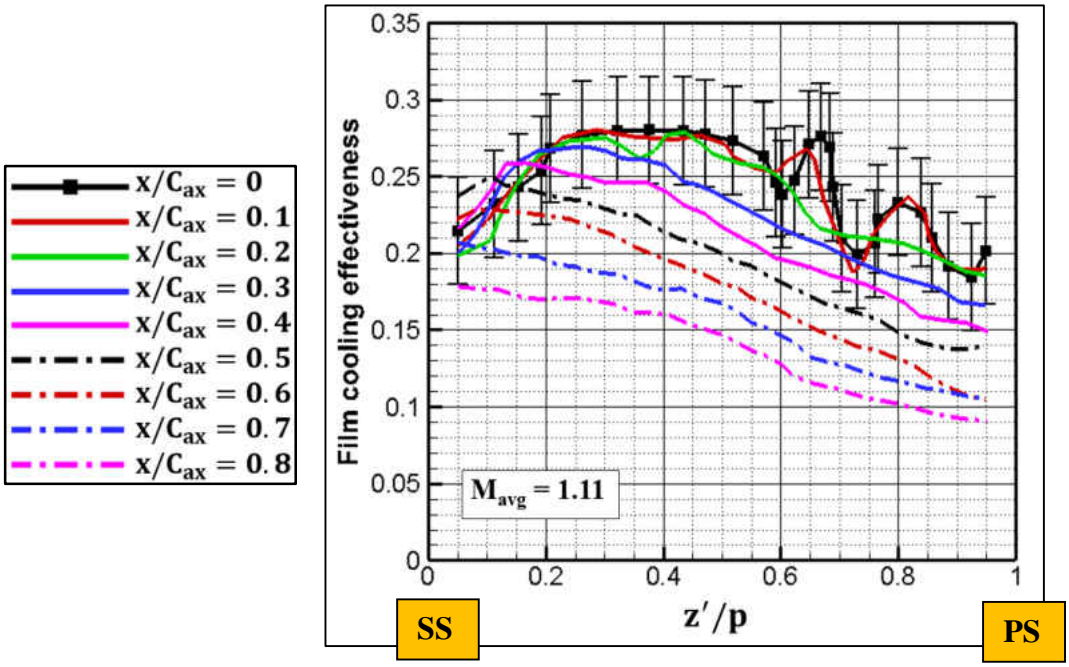

Figure 106: Pitchwise film cooling effectiveness - case 3

Cooling Uniformity Coefficient

For the first time in endwall film cooling studies, a cooling uniformity coefficient (CUC) (defined in chapter 6) is used in addition to the pitchwise film cooling effectiveness to quantify the uniformity in the film cooling. The normalizing parameter in Equation 6.17 can be different in a real engine scenario depending on the target film cooling effectiveness value at a given streamwise location. The goal behind reporting the CUC is to provide a better representation of the local hot and cold spots on the endwall. The CUC results are shown in Figures 107-109. The CUC values close to the airfoil walls are not reported due to high uncertainty in the experimental data.

Since the pitch-averaged film cooling effectiveness decreases along the streamwise direction, it is necessary to terminate the reported CUC values when the pitch-averaged film cooling effectiveness approaches a very low value so that the CUC values are realistic.

For this purpose, the CUC values are reported in this study only for the airfoil axial chord locations which have $\bar{\eta}(x) \geq 0.5 * \bar{\eta}(x = 0)$. By connecting the CUC plot with the film cooling effectiveness contour (Figures 66-68), improved film cooling hole locations to achieve close to uniform film coverage can be obtained.

For M_{avg} = 0.56 (Figure 107), it can be observed that at x/C_{ax} = 0, the CUC remains above 1 with slight variations (between 1.05 and 1.18) along the pitchwise direction between $z'/p \cong 0.28$ and $z'/p \cong 0.59$. This is the coalesced region of the film cooling jets 5-12 near the airfoil suction side (Figure 66). At $z'/p > 0.59$, the film jets exhibit discrete behavior resulting in a pronounced variation of CUC. It can also be seen from Figure 66 that part of jet 2 deflects to the suction side of the adjacent airfoil passage after interacting with the airfoil leading-edge. This decreases the film jet's efficacy in the studied airfoil passage resulting in a lower CUC which can be related to the last peak near the airfoil pressure side in Figure 107. The CUC values at x/C_{ax} = 0 are used as a reference to compare the downstream CUC values. At x/C_{ax} = 0.1, no noticeable change is seen in the CUC.

It is observed that the CUC is less than unity for ≅ 40% of the region near the airfoil pressure side for $x/C_{ax} > 0.2$. Moving downstream, x/C_{ax} = 0.3 exhibits higher non-uniformity in film cooling due to the pronounced coolant accumulation effect. There is also a significant shift in the over-cooled region towards the airfoil suction side. This behavior is due to the movement of the PV separation line which acts like a virtual wall preventing the coolant from reaching the airfoil pressure side. At x/C_{ax} = 0.4, the peak CUC value remains unchanged (≅ 1.4) from x/C_{ax} = 0.3, but the under-cooled area increases. There are two possible reasons for this: (i) coolant removed from the endwall due to the PV action and (ii) narrowing of the passage area unaffected by the endwall flow separation. The CUC

variation is augmented at x/C_{ax} = 0.5 with the maximum and minimum values being 1.47 and 0.65 approximately. There is a steep decrease in CUC from 1.46 at $z'/p \cong 0.14$ to 0.79 at $z'/p \cong 0.52$, beyond which the decay becomes gradual.

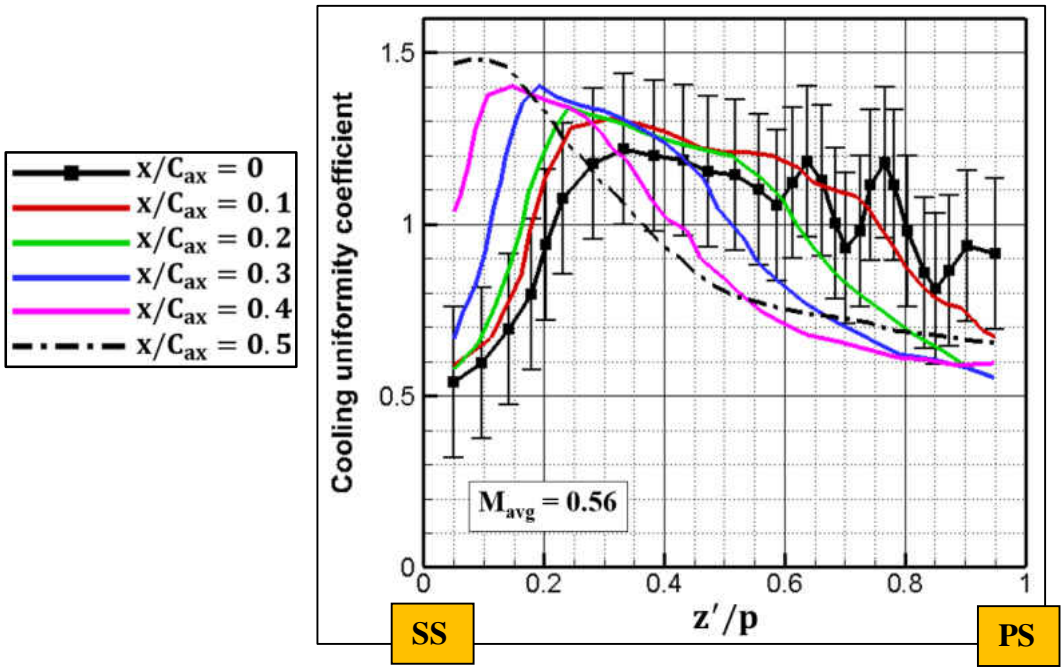

Figure 107: Cooling uniformity coefficient - case 1

Increasing the average blowing ratio to M_{avg} = 0.83 (Figure 108) results in negligible difference in the CUC between x/C_{ax} = 0,0.1,0.2. For locations downstream of x/C_{ax} = 0.2, ≅ 35% of the region near the airfoil pressure side has CUC less than 1, indicating inadequate uniformity in film cooling. There is a slight increase in the CUC at x/C_{ax} = 0.3 with a maximum of ≅ 1.29 at $z'/p \cong 0.19$. The CUC drops to ≅ 0.6 close to the airfoil pressure side. The downstream locations (x/C_{ax} = 0.5,0.6) exhibit similar trends with a drastic variation in CUC from the airfoil suction side to pressure side.

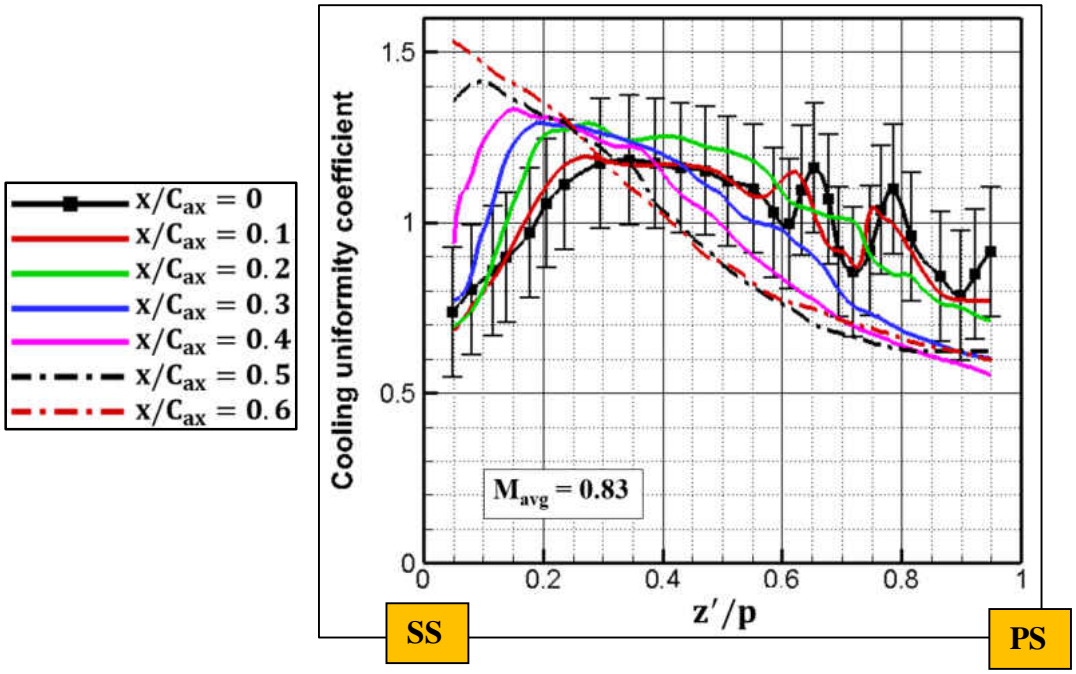

Figure 108: Cooling uniformity coefficient - case 2

When the average blowing ratio is increased to M_{avg} = 1.11 (Figure 109), it is observed that there is negligible variation in CUC between x/C_{ax} = 0,0.1,0.2,0.3 at most of the pitchwise locations. The CUC is less than 1 for ≅ 40% of the region near the airfoil pressure side for $x/C_{ax} > 0.2$. A close to stable CUC region is noted between $z'/p \cong 0.2$ and $z'/p \cong 0.57$ for x/C_{ax} = 0,0.1,0.2. The locations downstream of x/C_{ax} = 0.4 exhibit an increase in the CUC between $z'/p \cong 0.05$ and $z'/p \cong 0.16$ with a maximum value of 1.32. Past $z'/p \cong 0.16$, there is no noticeable change in CUC compared to the upstream locations.

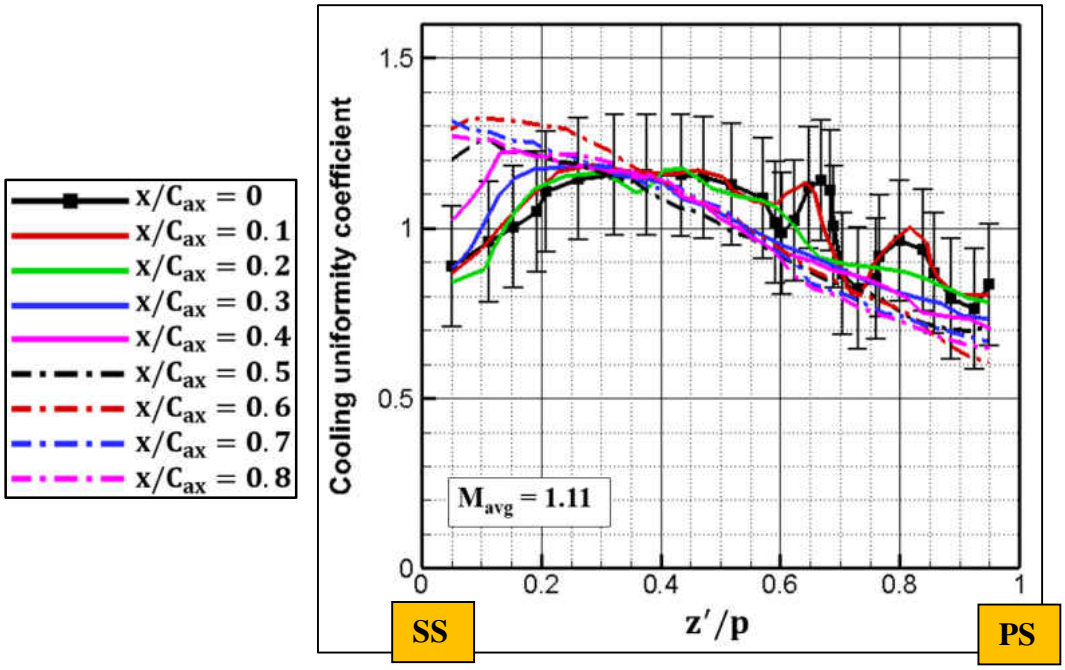

Figure 109: Cooling uniformity coefficient - case 3

Pitch-averaged Film Cooling Effectiveness

In order to quantify the average film cooling efficiency along the streamwise direction, the pitch-averaged film cooling effectiveness is reported in Figure 110. The film cooling effectiveness decay rate is nearly the same for M_{avg} = 0.56, 0.83 at all x′/D locations. Between M_{avg} = 0.56 and M_{avg} = 0.83, the film cooling effectiveness is quantitatively same at all x′/D locations. The lowest blowing ratio (M_{avg} = 0.56) is used as a reference case for comparing with the higher blowing ratio cases. Elevating the blowing ratio to M_{avg} = 1.11 results in a substantial increase in the film cooling effectiveness with the maximum (≅16.4%) occuring at x′/D ≅ 23. Although jet lift-off was seen for the film cooling jets near the airfoil pressure side for M_{avg} = 0.83,1.11, this is not explicitly observed in the pitch-averaged representation. This reinforces the essentiality of studying the local film

cooling effectiveness distribution. For M_{avg} = 1.11, the decay rate is less steep compared to M_{avg} = 0.56, 0.83 till x′/D ≅ 18, after which, the decay trend is similar to the low blowing ratio cases.

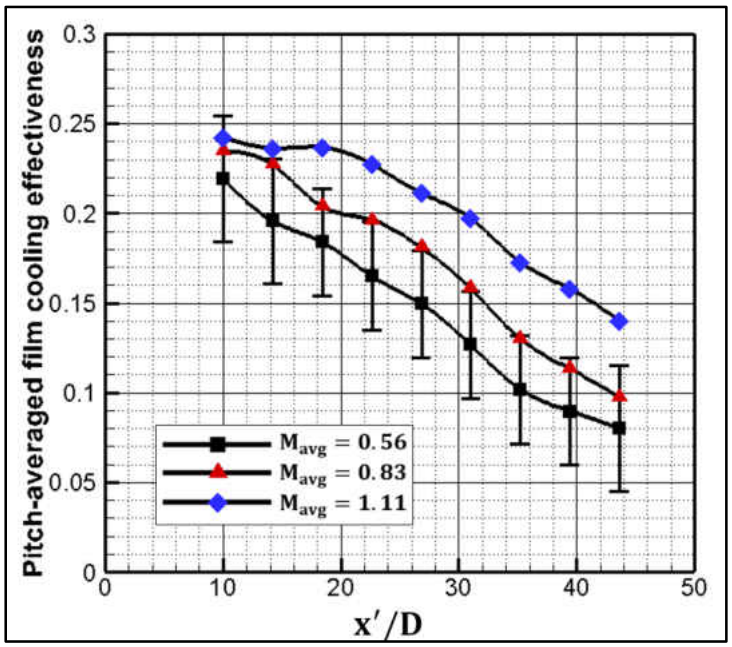

Figure 110: Pitch-averaged film cooling effectiveness

Comparison with Published Literature

Among the published literature in cascade film cooling, a wide variation is observed in the airfoil and endwall geometries, flow conditions, film cooling hole location, spacing between film cooling holes and the definition of blowing ratio. These differences make it very difficult to establish a fair comparison between the results of the present study and the published literature for the pitch-averaged film cooling effectiveness. For this reason, no literature comparison is reported in the present study.

Connection with Real Engine Endwall Film Cooling Design

The present study provides insight into the interaction between the coolant film injected upstream of the airfoil leading-edge using discrete cylindrical holes and the endwall secondary flow. The connection between the surface flow and the three-dimensional flow field is established. Unlike a real engine, the density ratio, combustor exit thermal and hydrodynamic profiles, shock waves in the airfoil passage, leakage flows and turbulence intensity levels could not be replicated in the present study due to constraints in experimental facilities.

The scientific methodology followed in the current investigation to (i) connect the surface flow to the three-dimensional flow field, (ii) quantify the film cooling non-uniformity, (iii) relate the hole-by-hole blowing ratio to the film cooling jet behavior, and (iv) use computational results to explain the coolant-mainstream interaction in regions where experimental data is not available can be adapted for analyzing a real engine endwall film cooling case.

References

[1] Hay, N., Lampard, D., and Saluja, C.L., 1985, "Effects of cooling Films on the heat transfer coefficient on a flat plate with zero mainstream pressure gradient," *Journal of Engineering for Gas Turbines and Power*, Vol. 107, pp. 104-110.

[2] Eriksen, V.L., and Goldstein, R.J., 1974, "Heat transfer and Film cooling following injection through inclined circular tubes," *Journal of Heat Transfer*, Vol. 96, pp. 239-245.

[3] Goldstein, R.J., and Taylor, J.R., 1982, "Mass transfer in the neighborhood of jets entering a crossflow," *Journal of Heat Transfer*, Vol. 104, pp. 715-721.

[4] Yuen, C. H. N., and Martinez-Botas, R. F., 2003, "Film cooling characteristics of a single round hole at various angle in a cross flow: Part II-heat transfer coefficients," *International Journal of Heat and Mass Transfer*, Vol. 46, pp. 237-249.

[5] Friedrichs, S., 1997, "Endwall film-cooling in axial flow turbines", *Ph.D. Dissertation*, Cambridge University, Cambridge, United Kingdom.

[6] Denton, J. D., 1993, "Loss mechanisms in turbomachines", *Journal of Turbomachinery*, Vol. 115, pp. 621-656.

[7] Takeishi, K., Matsuura, M., Aoki, S., 1989, "Experimental study of heat transfer and film cooling on low aspect ratio turbine nozzles", *Journal of Turbomachinery*, Vol. 112, pp. 488-496.

[8] Friedrichs, S., Hodson, H. P., and Dawes, W. N., 1999, "The design of an improved endwall film-cooling configuration", *Journal of Turbomachinery*, Vol. 121, pp. 772-780.

[9] Sinha, A. K., Bogard, D. G., and Crawford, M. E., 1991, "Film-cooling effectiveness downstream of a single row of holes with variable density ratio", *Journal of Turbomachinery,* Vol. 113, pp. 442-449.

[10] Friedrichs, S., Hodson, H.P., and Dawes, W.N., 1997, "Aerodynamic aspects of endwall film-cooling", *Journal of Turbomachinery*, Vol. 119, pp. 786-793.

[11] Gritsch, M., Schulz, A., and Wittig, S., 2001, "Effect of crossflows on the discharge coefficient of film cooling holes with varying angles of inclination and orientation", *Proceedings of the International Gas Turbine and Aeroengine Congress and Exposition*, 2001-GT-134, pp. 1-9.

[12] Lutum, E., and Johnson, B. V., 1998, “Influence of hole length-to-diameter ratio on film cooling with cylindrical holes”, *Journal of Turbomachinery*, Vol. 121, pp. 209-216.

CHAPTER 10: CONCLUSIONS

Unsteady Passing Wake Effect on a Pitchwise-curved Surface

In the first part of the research study, the effect of unsteady passing wakes on heat transfer was experimentally investigated on a pitchwise-curved surface representing an endwall without airfoils with a wall-normal wake-rod orientation. Discrete film cooling jets were injected at 35º to the test surface with no compound angle. Eliminating the airfoils provided an opportunity to study the effect of passing wakes in isolation. Coolant to mainstream mass flux ratios between 0.25 and 0.75 were tested at two wake Strouhal numbers (S = 0.15, 0.3) along with the study of passing wake effect without film injection on heat transfer. The density ratio was held approximately constant at 1. Some of the key findings include:

1. Passing wakes augment the heat transfer coefficient at both wake passing frequencies (S = 0.15, 0.3). The highest increase in the heat transfer augmentation solely due to the unsteady passing wakes was measured to be 7.6% approximately at S = 0.3.
2. A combination of film injection and unsteady passing wakes resulted in a maximum pitch-averaged and centerline heat transfer augmentation of ≅ 28% and 31.7% respectively, relative to the no wake and no film injection case.
3. The maximum increase in the heat transfer augmentation (≅ 4.5%) between z/D = 0 and z/D = 1.5 occurred at M = 0.75, S = 0.3 and at x/D ≅ 2.5. This rise in the heat transfer augmentation is conjectured to be due to the interaction between the film jets.

4. The passing wake-induced velocity perturbations are considered to be one of the primary contributors towards the increased heat transfer augmentation.

Endwall Film Cooling in a High Subsonic Annular Cascade

In the second part of the research study, the interaction between endwall secondary flow and coolant film was experimentally investigated using surface oil visualization and film cooling effectiveness measurements in a high subsonic annular cascade. Coolant was injected using discrete film holes inclined at 30° to the inner endwall. The average blowing ratio was varied between 0.56 and 1.11 with the density ratio held approximately constant at 0.89. Computations were performed to predict the individual film cooling hole discharge coefficients, local blowing ratio, temperature drop across the film cooling coupon and the streamlines of coolant and mainstream flow. Some of the pertinent findings include:

1. The saddle point movement exhibited close to a linear trend with increasing average blowing ratio. The highest shift (≅ 47% relative to $M_{avg} = 0$) was observed at $M_{avg} = 1.11$.
2. A maximum coolant temperature drop of ≅ 9.34°C was observed at $M_{avg} = 1.11$. It is extremely important to account for the coolant temperature drop in film effectiveness measurements.
3. Due to the induced incidence effect, the effective number of film cooling jets in the studied passage was reduced.
4. It is extremely important to account for the induced incidence effect while determining film cooling hole locations in cascade experiments so that the

individual film cooling hole mass flow rate and the film cooling jet trajectory are representative of a single airfoil passage.

5. The horseshoe vortex was augmented by coolant injection at locations upstream of s/C = 0.16.
6. The local mainstream static pressure and endwall separation lines have a profound effect on the film cooling hole mass flow rate and the jet trajectory.
7. The variation in the discharge coefficients between the film cooling holes decreases with increasing average blowing ratio.
8. A maximum variation of ≅ 10.7% was observed in the blowing ratio between hole-1 and hole-6 at M_{avg} = 1.11. The local blowing ratio is needed to predict individual film cooling jet behavior.
9. The variation in the local blowing ratio between the film cooling holes causes slight jet lift-off for film cooling jets-2,3 at M_{avg} = 0.83 and significant jet lift-off at M_{avg} = 1.11 as inferred from the local film cooling effectiveness distribution.
10. Film coverage increases with average blowing ratio but a large variation in the coolant distribution is observed at $x/C_{ax} > 0.2$ due to the coolant accumulation effect.
11. As the average blowing ratio increased, the distortion of the coolant streamlines by the endwall secondary flow was reduced. The coolant sustained its trajectory better at higher average blowing ratios.

CHAPTER 11: FUTURE WORK

The potential future work options for the cascade film cooling study are discussed in this chapter.

Airfoil Passage Film Cooling Measurements

As a continuation work of the endwall film cooling measurements (reported in Chapter 9), passage film cooling measurements will be performed for airfoil passage-3. The location of the film cooling holes inside the airfoil passage are very important since the pitchwise pressure gradient significantly alters the static pressure on the endwall. After reviewing the relevant published literature on airfoil passage film cooling, it was decided to orient the film cooling holes such that their exits followed the iso-Mach line for a given row of holes. This configuration results in a uniform blowing ratio and therefore higher cooling uniformity as reported by Harasgama and Burton [1] and Knost and Thole [2].

Positioning of Film Cooling Holes on Iso-Mach lines

In order to obtain the static pressure distribution on the endwall, the PSP technique (see Chapter 4) was used. The isentropic Mach number corresponding to the measured static pressure was calculated using the isentropic relation given in Equation 11.1.

$$\frac{P_o}{P} = \left[1 + \frac{\gamma - 1}{2} Ma^2\right]^{\frac{\gamma}{\gamma-1}} \tag{11.1}$$

The isentropic Mach number distribution was superimposed on the endwall along with the surface streamlines obtained from surface oil visualization. While the former

provides the local velocity for the near endwall flow, the latter gives the local mainstream flow direction which can be used to determine the orientation of the film cooling hole. An adapter was used to connect the endwall to the coolant plenum. Few essential design guidelines were followed before arriving at the film cooling hole locations. Most of the design guidelines were based on published literature and manufacturing limitations. The design guidelines are given below.

1. The film cooling hole should have minimal angle relative to the local mainstream flow to avoid increased aerodynamic losses.
2. In order to avoid wall effects, the film cooling hole should be located away from the coolant plenum walls.
3. The inclination angle of the film cooling hole should be 35° or less to avoid jet lift-off at low momentum flux ratios.
4. The film cooling hole pitch should be representative of typical engine endwall film cooling configuration.
5. There should be adequate access to machine the film cooling holes on the endwall.
6. Since there is significant coolant deficit near the airfoil pressure side (as observed from film cooling upstream of the leading-edge), the passage film cooling holes should be located near the airfoil pressure side.
7. The film cooling holes should be positioned away from the airfoil throat region to avoid large mainstream density variations.

Considering the aforementioned guidelines, the hole locations were selected. The isentropic Mach number distribution superimposed on the endwall along with the film cooling holes is shown in Figure 111. The calculated values of the mainstream isentropic Mach number at the exit of each film cooling hole and the specifications of the passage film cooling hole geometry are given in Table 12.

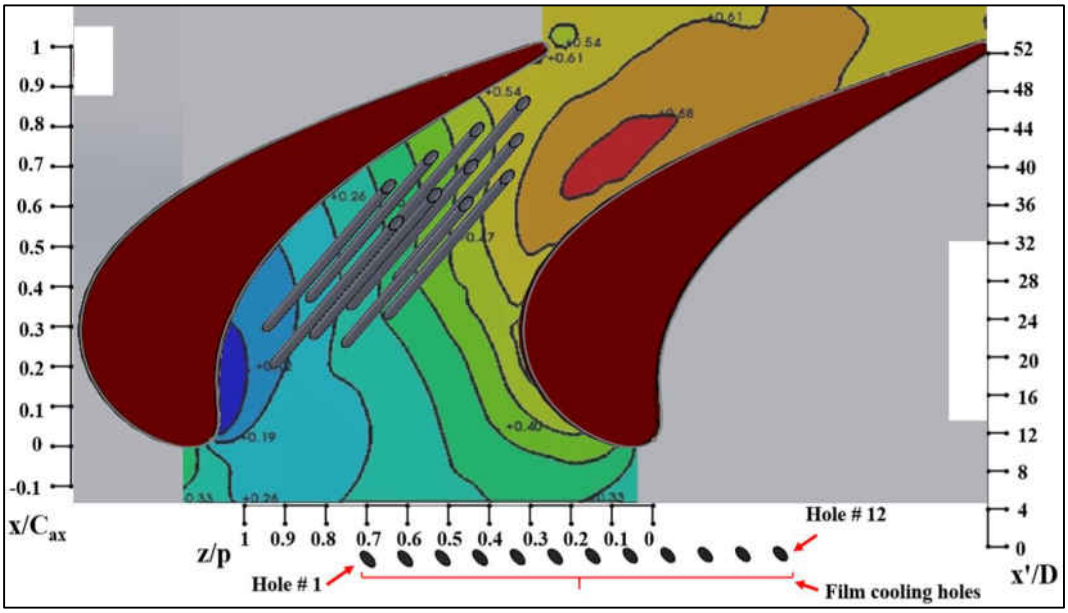

Figure 111: Isentropic Mach number contour superimposed on passage film cooling holes

Table 12: Specifications of airfoil passage film cooling holes

Row no.	Hole no.	$Ma_{is,e}$	L/D	p/D	α (deg)	β (deg)
1	1	0.33	21.7	4	35	35
	2	0.33	21.8	4	35	35
2	1	0.4	22.6	4	35	35
	2	0.4	22.6	4	35	35
3	1	0.47	22.3	4	35	35
	2	0.47	22.3	4	35	35
	3	0.47	22.3	4	35	35
4	1	0.54	22.3	4	35	35
	2	0.54	22.3	4	35	35
	3	0.54	22.3	4	35	35

Experimental Setup

The cascade tunnel will be operated in an open-loop configuration for passage film cooling measurements. The setup for the coolant flow is identical to the cascade film cooling measurements (see Chapter 5). The blowing ratios for the experiments will be selected based on the range of the thermal mass flow meter and the maximum available mass flow rate from the compressed air supply.

Machining of Passage Film Cooling Holes

After the film cooling hole locations were ascertained, a CAD model of the endwall with the passage film cooling holes was prepared. With a small diameter (2 mm) and a large L/D (> 20), it was a challenge to arrive at a suitable drilling procedure for the film cooling holes. The machining of the film cooling holes was performed by House of Plastics Unlimited (Orlando, Florida). Due to the large L/D (> 20) of the film cooling holes, the drilling tool was most likely to get over-heated during the machining process since the removed material gets accumulated on the drilling tool.

After several hours of discussion with House of Plastics Unlimited, it was decided to perform the entire drilling process inside a box of coolant fluid (typically soap water) covering the airfoil passage-3. The coolant fluid was expected to keep the temperature of the drilling tool low. The machined inner endwall with the passage film cooling holes is shown in Figure 112. Based on the measurements of the machined film cooling holes, the tolerance on the film cooling hole spacing was found to be ±0.1 mm and the film cooling hole diameter had negligible difference from the nominal value.

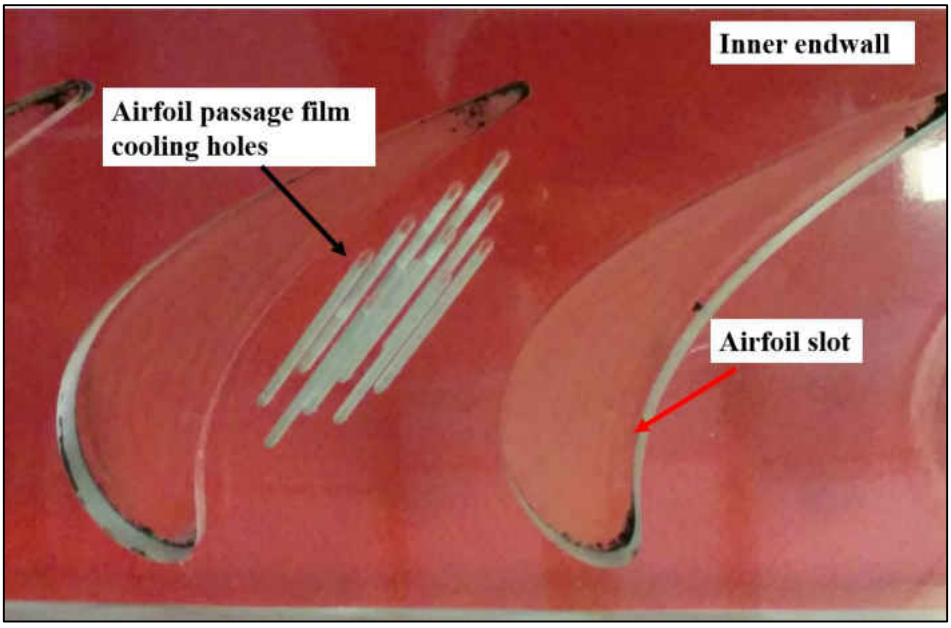

Figure 112: Machined passage film cooling holes on inner endwall

Endwall Heat Transfer Measurements

Due to the significant influence of the endwall secondary flows on the surface flow pattern, the heat transfer coefficients on the endwall exhibit large variations from the pressure side to the suction side of the airfoil inside the airfoil passage [3]. In addition to this, film injection can also alter the heat transfer coefficient distribution on the endwall depending on the momentum flux ratio. Investigating the endwall heat transfer under high subsonic flow conditions with a maximum isentropic throat Mach number of ≅ 0.68 can provide close to engine-realistic heat transfer distribution. This is the motivation behind the second part of the future work.

The density ratio will be maintained approximately constant at 1 for all the experiments. The test matrix for the proposed experiments is given in Table 13. The coolant flow setup will be similar to that described in Chapter 5 of this dissertation without the in-

line heaters to elevate the temperature of the coolant. The foil heater technique used in the unsteady passing wake study will be adapted (with some modifications to the heater layout) to provide a constant heat flux boundary condition on the endwall. The heaters are made of stainless steel (type 321) with thickness ≅ 51μm, electrical resistivity and thermal conductivity at 25˚C being 75×10^{-8} Ohm-m and 14.12 W/mK respectively. For obtaining the local temperatures on the endwall, the TSP technique will be used.

Table 13: Proposed test matrix for endwall heat transfer measurements

Cooling method	Measurement	M_{avg}	I_{avg}	DR	p/D	L/D
Discrete film (Cylindrical hole)	Heat transfer	0	0	1	3.55	17
		0.56	0.31			
		0.83	0.69			
		1.11	1.23			
		1.38	1.9			

Heat Flux Calculation

The heat flux calculation was performed based on two values of typical heat transfer coefficients observed in an airfoil passage (obtained from preliminary CFD simulations) and considering the constraints in the available experimental facility. The heat flux calculations are shown in Table 14. Based on the resistance needed from the heater foil that spans the airfoil passage, the cross section and length of the heater foil was selected for a fixed current input. Due to the complex profile of the airfoil passage, a serpentine layout of the heater foil was necessary. The drawing of the foil heater to fit the airfoil passage-3 is shown in Figure 113.

Table 14: Heat flux calculation for endwall foil heater

h (W/m^2K)	Current (Amps)	T_w-T_r (°C/K)	Area (m^2)	q" (W/m^2)	thickness (m)	width (m)	resistance (Ohm)	Length (m)
500	6.8	35	0.00939	17500	51×10^{-6}	0.004	3.554	0.967
700	8.1	35	0.00939	24500	51×10^{-6}	0.004	3.506	0.969

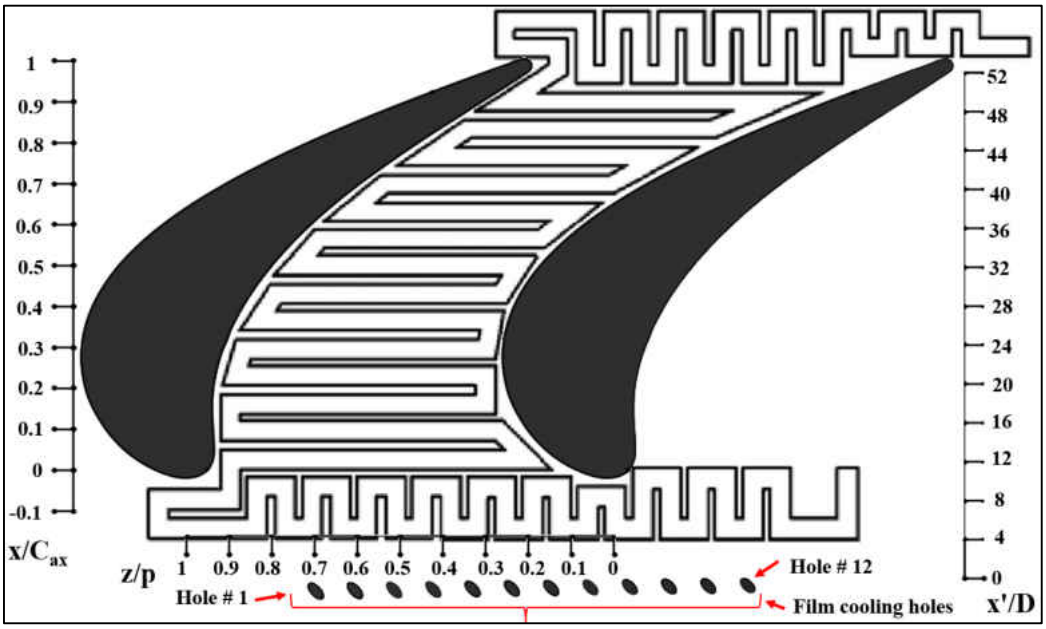

Figure 113: Heater layout for airfoil passage-3

Heater Foil Cutting

After exploring several options to cut the foil heater to obtain a serpentine layout (shown in Figure 113), abrasive water jet machining was selected due to its low cost and reasonable accuracy (± 0.25 mm). As a preparatory process for the heater foil cutting, two fixture plates (drawing shown in Figure 114) were machined out of aluminum to enclose multiple heater foils that will accommodate the serpentine heater layout with some tolerance on the circumference for the fasteners. Each heater foil was attached to a double-sided Kapton tape (shown in Figure 115) so that the cut foil can later be affixed to the

endwall. In order to avoid shifting of the heater foils during the cutting process, the two fixture plates were bolted around the circumference with appropriate spacing between the bolts. The fixture plates prior to the cutting process are shown in Figure 116.

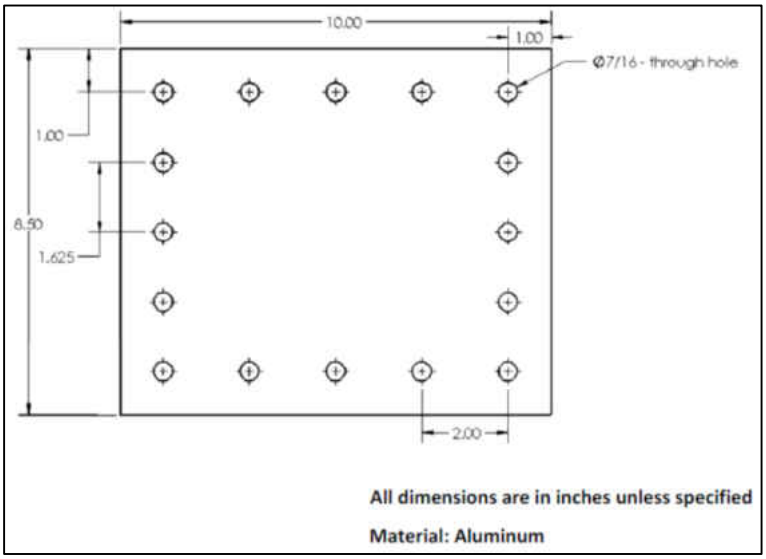

Figure 114: Drawing of fixture plate for heater foil cutting

The heater foil cutting (abrasive water jet machining) was performed by Doudney Sheet Metal Inc., (Orlando, Florida). Figure 117 shows the heater foil after the water jet machining process. Due to the expansion of the water jet after it exits the nozzle, the last few foils (along the direction of the water jet) exhibited large deviations from the drawing dimensions. These foils will not be used for the heat transfer experiments.

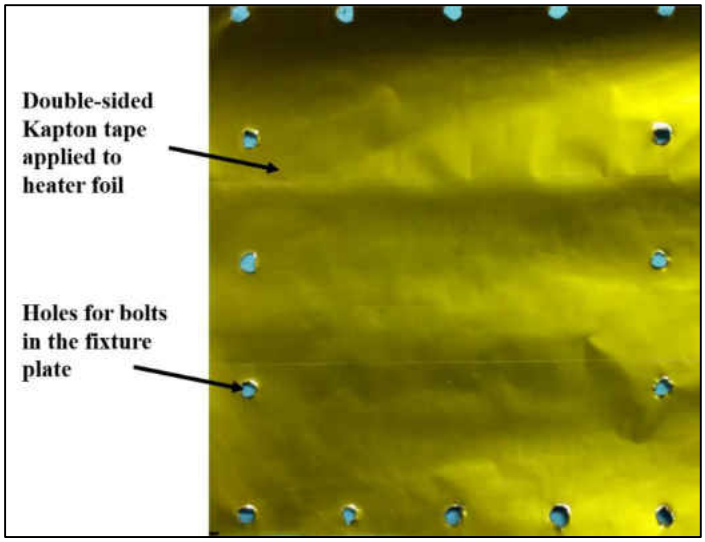

Figure 115: Heater foil with double-sided Kapton tape

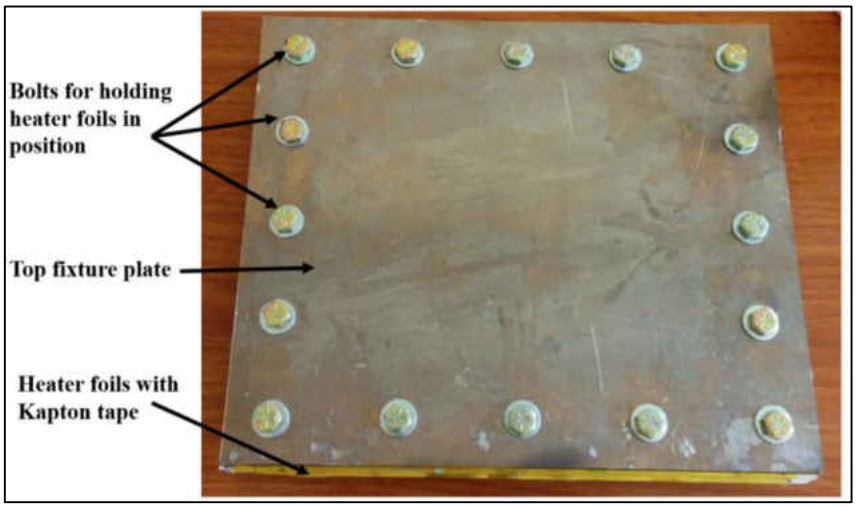

Figure 116: Fixture plates with heater foils before cutting

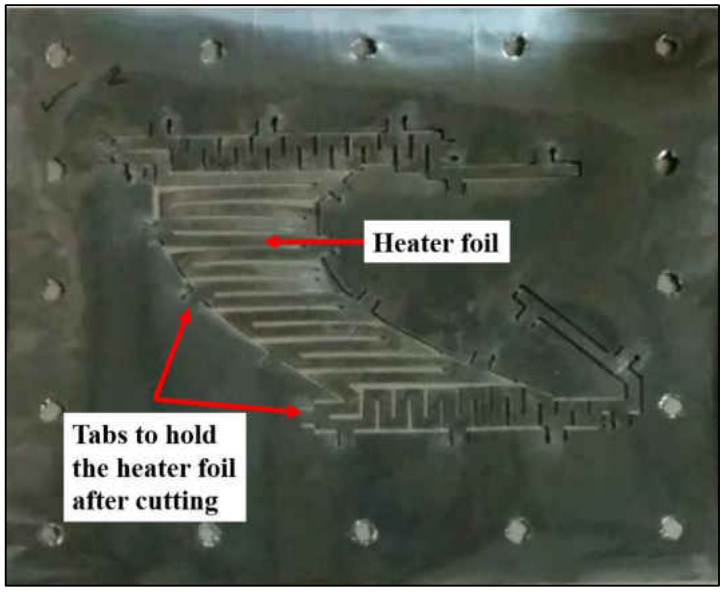

Figure 117: Heater foil after cutting

Experimental Setup

The cascade tunnel will be operated in an open-loop configuration for heat transfer measurements. While operating in open loop, the mainstream temperature reaches steady state at 35˚C approximately. The serpentine layout of the foil will be adhered to the endwall using Kapton tape to hold the heater in place. The Kapton tape is made from Kapton polyimide film with silicon adhesive. The thickness ranges between 0.025 mm to 0.127 mm and they are compatible over a wide temperature range (-269°C to 400°C) with a thermal conductivity of ≅ 0.5 W/mK. The lowest thickness Kapton tape will be used with the foils. The usage of Kapton tape provides good electrical isolation (resistance ≅ 1×10^{12} ohms) from the plexiglass substrate. The ends of the heater foil will be connected to copper bus bars to which a variable alternating current voltage is applied. By supplying an

appropriate potential difference across the copper bus bars, the required power input to the heater or the heat flux is obtained.

Foil Heater Technique

In order to measure the endwall surface temperature, the heaters are painted with TSP (see chapter 4 for the TSP technique). Three to four thermocouples are sandwiched between the Kapton tape and the heater in order to measure the temperature of the foil. The foil temperature needs to be closely monitored because the plexiglass substrate (endwall) can change optical properties if the temperature exceeds 80°C. The foil temperatures are also used to validate the TSP temperatures. The tunnel is allowed to reach steady state by monitoring the mainstream and heater foil temperature before the TSP images are taken. The foil heater experimental setup is shown in Figure 118. The heat transfer coefficient is defined in Equation 11.1.

$$h = \frac{q_w''}{(T_w - T_r)} \tag{11.1}$$

Where, T_w is the endwall surface temperature with heat flux input and T_r is the recovery temperature. The recovery temperature is measured on the endwall surface with the mainstream flow turned on and the voltage to the foil heater turned off. With introduction of film cooling, the heat transfer coefficient is calculated using the same definition given in Equation 11.1.

The heat transfer augmentation in the presence of film cooling is defined in Equation 11.2.

$$h_{aug} = \frac{h_f}{h_o} \tag{11.2}$$

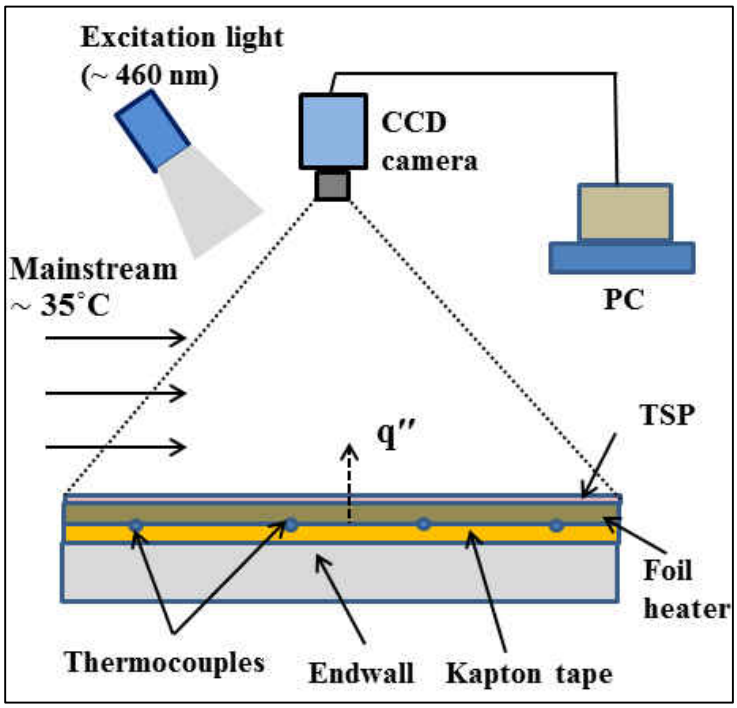

Figure 118: Foil heater measurement technique

References

[1] Harasgama, S. P., and Burton, C. D., 1992, "Film cooling research on the endwall of a turbine nozzle guide vane in a short duration annular cascade: part I-experimental technique and results", *Journal of Turbomachinery*, Vol. 114, pp. 734-740.

[2] Knost, D.G. and Thole, K.A., 2005, "Adiabatic effectiveness measurements of endwall film-cooling for a first stage vane", *Journal of Turbomachinery*, Vol. 127, pp. 297-305.

[3] Graziani, R.A., Blair, M.F., Taylor, J.R. and Mayle, R.E., 1980, "An Experimental Study of Endwall and Airfoil Surface Heat Transfer in a Large Scale Turbine Blade Cascade", ASME Journal of Engineering for Power, Vol. 102, pp. 257-267.

APPENDIX A: PUBLICATIONS

Journal Publications

[1] Mahadevan, S., Kutlu, B., Golsen., M, Verma, S. B., Kapat, J. S., 2015, "Experimental study of unsteady wake effect on a film-cooled pitchwise-curved surface", *International Journal of Heat and Mass Transfer*, Vol. 83, pp. 118-135.

[2] Mahadevan, S., Ricklick, M., Kapat, J. S., 2013, "Internal cooling using porous turbulators", *AIAA Journal of Thermophysics and Heat Transfer*, Vol. 27, No. 3, pp. 526-533.

Under Preparation for the International Journal of Heat and Fluid Flow:

Mahadevan, S., Verma, S. B., Kapat, J. S., 2015, "Experimental and numerical study of secondary flow and coolant film interaction in a high subsonic annular cascade".

Conference Presentations

[1] Mahadevan, S., Kutlu, B., Golsen., M, Kapat, J. S., 2012, "Heat Transfer and Film Effectiveness Study on a Pitchwise Curved Surface with Unsteady Wake Interaction", AIAA 2012-4101.

[2] Mahadevan, S., Golsen., M, Nguyen, C. Q., Ricklick, M., Kapat, J. S., 2011, "Secondary Flow and Coolant Film Interaction in a High Subsonic Cascade", IGTC 2011-0152.

[3] Mahadevan, S., Ricklick, M., Kapat, J. S., 2011, "Endwall Heat Transfer and Pressure Drop Measurements in a Rectangular Channel with Porous Turbulators", AIAA 2011-6097.

APPENDIX B: COPYRIGHT PERMISSION LETTERS

Aeroprobe Corporation

From,
Srikrishna Mahadevan,
University of Central Florida,
12781, Ara Dr. Orlando, FL 32816, USA

October 6, 2015

To,
Senior Account Manager
Aeroprobe Corporation,
200 Technology Drive
Christiansburg, VA 24073 USA

Dear Sir/Mam,

I am completing a doctoral dissertation at the University of Central Florida entitled "Experimental and Numerical Study of Endwall Film Cooling". I would like your permission to reprint in my dissertation, excerpts from the following:

"Multi-hole Probe Manual", 2015, Aeroprobe Corporation, Blacksburg, VA, USA.

The excerpt(s) to be reproduced are:

Page 4, Probe kit
Page 11, Pressure port arrangement for L-shaped probe
Page 20, Drawing of L-shaped probe

The requested permission extends to any future revisions and editions of my dissertation, including non-exclusive world rights in all languages. These rights will in no way restrict republication of the material in any other form by you or by others authorized by you. Your signing of this letter will also confirm that you own or your company owns the copyright to the above-described material.

If these arrangements meet with your approval, please sign this letter where indicated below and email a scanned copy at the earliest possible to: srikrishna@knights.ucf.edu

Thank you for your attention in this matter.

Sincerely,

Srikrishna Mahadevan
Doctoral Candidate,
Center for Advanced Turbomachinery and Energy Research,
Department of Mechanical and Aerospace Engineering,
University of Central Florida, Orlando, FL 32816
Email: srikrishna@knights.ucf.edu
Phone: 407-437-8091

PERMISSION GRANTED FOR THE USE REQUESTED ABOVE:

By: _____ (Signature)

Josh Bishop (Print name)

Date: 10/5/15